HIGH ENERGY PULSE PROPAGATION AND PARAMETRIC CONVERSION IN NORMAL-DISPERSION OPTICAL FIBERS

A Dissertation

Presented to the Faculty of the Graduate School

of Cornell University

in Partial Fulfillment of the Requirements for the Degree of

Doctor of Philosophy

by

Simon Lefrançois

August 2012

HIGH ENERGY PULSE PROPAGATION AND PARAMETRIC

CONVERSION IN NORMAL-DISPERSION OPTICAL FIBERS

Simon Lefrançois, Ph.D.

Cornell University 2012

The development of ultrafast lasers has enabled a wide range of applications such as time-resolved spectroscopy, micro-machining and non-linear microscopy. For the past 20 years, solid-state lasers have been the workhorses of ultrafast science. However, they remain bulky and sensitive tools requiring careful alignment. Thus, rare-earth doped fiber lasers have generated significant interest. They can be monolithically integrated and use simple power scalable diode pumping. Thanks to recent advances in the understanding of non-linear pulse evolution in optical fiber, as well as the development of large-core fiber technologies, fiber lasers have achieved performance matching conventional solid-state lasers.

This thesis explores the non-linear propagation and parametric conversion of high energy short pulses in normal dispersion optical fibers. A laser source for coherent anti-Stokes Raman scattering microscopy is demonstrated based on frequency conversion of picosecond pulses through four-wave mixing in photonic crystal fiber. The effects of vibrational dephasing on the coherence and compressibility of Raman Stokes pulses generated in chirped-pulse fiber amplifiers are investigated. Finally, all-normal-dispersion fiber lasers are scaled to high pulse energies using large-core fibers. The performance of multimode step-index fiber, chirally-coupled core fiber and photonic crystal fiber is compared. Using fibers with robust mode-filtering, fibers lasers delivering up to a megawatt of peak power are demonstrated.

BIOGRAPHICAL SKETCH

Simon Lefrançois was born in Quebec City, Canada in 1985. Before he started school, his family moved to nearby Drummondville where he spent the rest of his childhood. After briefly considering a career as a medical doctor, he instead opted to pursue raw curiosity in the natural sciences. He moved back to Quebec City to study physics at Université Laval, where he received his bachelor's degree in 2007.

Having completed two summer internships in nanoscience, he initially considered graduate studies in condensed matter and nanoscale physics. He thus enrolled in the Applied Physics PhD program at Cornell University. After exploring his options during the first year, he decided to try a fresh direction and joined the ultrafast optics group of Pr. Frank W. Wise in the summer of 2008. He spent the next four years studying the propagation of ultrashort pulses in optical fibers and designing fiber laser systems for various applications.

After obtaining his PhD, he will be moving on to a post-doctoral position at the University of Sydney. There, he plans to study non-linear and ultrafast optics in nanophotonics devices and work on high bandwidth optical communications and signal processing.

ACKNOWLEDGEMENTS

TABLE OF CONTENTS

LIST OF TABLES

LIST OF FIGURES

CHAPTER 1

INTRODUCTION

Ultrashort pulse lasers have opened up new scientific and technical frontiers in time-resolved material and chemical studies, non-linear microscopy, precision machining, and metrology. Mode-locked Ti:sapphire oscillators [1] have long been the workhorses of ultrafast science due to their broadband gain, large tunability and advantageous laser material qualities. However, they are limited by the power available from high beam quality solid-state pump lasers. Diode-pumped solid-state lasers, both in crystal [2] and thin-disk format [3], offer competitive performance but still require careful alignment, complex thermal management and specialized maintenance.

Rare-earth doped fiber lasers confine the cavity light into bendable waveguides, opening the way to compact, monolithic laser sources. Besides reducing or eliminating complex alignment, waveguiding of the signal and pump also offers very high gain per pass and excellent thermo-optical properties. They can be pumped by power scalable diode lasers to deliver large average powers.

However, the tight confinement of light into fiber waveguides results in the accumulation of large non-linear phaseshifts. Understanding the role of nonlinearity in ultrashort pulse evolution is thus critical. At anomalous dispersion, the pulse peak power is constrained by modulation instability and soliton formation. At normal dispersion, new classes of chirped-pulse evolution such as similaritons and dissipative solitons emerge. They can support large non-linear phaseshifts and spectral broadening while avoiding wavebreaking. This has enabled fiber lasers to compete directly with solid-state laser performance. Non-linear interaction such as stimulated Raman scattering (SRS) and four-wave mixing (FWM) also display

qualitatively different behavior at normal dispersion. SRS is generally recognized as limit in normal dispersion chirped-pulse amplifiers, while FWM is attractive as a frequency shifting and signal processing mechanism.

This thesis focuses on the scaling to high energies of ultrashort pulse propagation and parametric conversion in normal dispersion optical fibers. Four-wave mixing in photonic crystal fiber (PCF) is used for tunable conversion of picosecond pulses. To overcome spontaneous noise and pulse walk-off, seeding the process is critical. This enables a two-color picosecond fiber laser for coherent anti-Stokes Raman scattering (CARS) microscopy matching solid-state laser performance in a robust and integrable package. Moving on to fiber amplifiers, the coherence properties of Stokes pulses generated by SRS in chirped-pulse amplifiers are then studied. Stokes pulses can be recompressed to high peak powers when the Raman dephasing time is not too short compared to the input pulse duration. Finally, the scaling of all-normal dispersion (ANDi) fiber lasers using large mode-area (LMA) fibers is investigated. By comparing step-index multimode fiber, chirally-coupled core (CCC) fiber and PCF, it is found that mode-locked oscillators are perturbed by small amounts of higher-order mode content, leading to a reduced maximum single pulse energy. This can be solved using robust and integrated mode filtering mechanism. Fiber lasers delivering up to a megawatt of peak power are then demonstrated.

1.1   Organization of the thesis

The thesis is organized as follows.

Chapter 1 introduces key concepts and models that will be used throughout the thesis. Modeling ultrashort pulses in the presence of higher-order non-linear ef-

fects will be done using the generalized non-linear Schrödinger equation (GNLSE). Four-wave mixing in optical fibers will be explained. A brief introduction to CARS microscopy is given. Important pulse evolution mechanism in fiber lasers will be discussed, including solitons, similaritons and dissipative solitons. Finally, important pulse shaping elements for mode-locked lasers will be introduced, specifically saturable absorbers and spectral filters.

Chapter 2 demonstrates a two-color picosecond fiber laser for CARS microscopy. The FWM process used for frequency conversion is modeled to provide design guidelines. A high energy divided-pulse fiber amplifier is described. Results from frequency shifting experiments in PCF are presented. CARS imaging of animal tissues and cells is demonstrated.

Chapter 3 explores the coherence of SRS Stokes pulse in chirped-pulse amplifiers. Vibrational dephasing times ranging from 32 fs to 32 ps are studied. The compressibility and pulse quality are assessed, as well as the statistics of this spontaneously seeded process.

Chapter 4 gives an overview of the mode-locking performance of ANDi lasers based on LMA fibers. Results from step-index, CCC and PCF fiber are compared and a link is established between higher-order mode content and the maximum stable single-pulsing energy.

Chapter 5 presents a high energy dissipative soliton fiber laser based on CCC fiber. The intracavity pulse evolution is modeled and beam quality and higher order mode suppression are assessed. Up to 40 nJ pulses dechirping below 200 fs are obtained, while pulse durations down to 100 fs are possible by optimizing the cavity design.

Chapter 6 demonstrates the scaling of amplifier similariton lasers to high peak powers using CCC fiber. As before, the pulse evolution is modeled, the beam quality assessed and mode-locked performance is presented. Up to 60 nJ pulses are delivered with dechirped durations below 90 fs.

Chapter 7 presents the scaling of dissipative soliton fiber lasers to megawatt peak powers. By using large core double-clad PCF, pulse energies of more than 150 nJ with dechirped durations of 115 fs are possible, in agreement with simulations.

Chapter 8 discusses future directions. Concepts for a fiber-OPO based on FWM in PCF and femtosecond frequency conversion through FWM will be presented. Then, the scaling of amplifier similariton fibers lasers through gain engineering will be discussed, as well as modeling the non-linear compression of dissipative soliton and amplifier similariton pulses.

1.2   Non-linear pulse propagation in optical fibers

An ultrashort optical pulse propagating through a medium can excite a wide range of non-linear responses due to its high peak power. This can fundamentally be described by including the non-linear response in Maxwell's equations. However, for pulse durations much longer than an optical cycle, Maxwell's equations can be reduced to a simpler first order differential equation called the generalized non-linear Schrödinger equation. This section outlines the derivation of the GNLSE and describes results relevant to pulse propagation and shaping in passive and active optical fibers.

1.2.1 Generalized non-linear Schrödinger equation

The derivation of the GNLSE is covered in standard textbooks, for instance in chapter 2.3 of Ref. [4]. Here I will summarize the key concepts and results of the derivation. For simplicity, we assume that the electric field $E(z, t)$ propagating along z is linearly polarized and has a fixed distribution in x and y, which is the case for a single-mode fiber in the absence of birefringence. The starting point is Maxwell's wave equation, in which the non-linear polarizability of the medium P_{NL} is added to the linear polarizability P_L. The speed of light and permeability in vacuum are c and μ_0 respectively.

$$\nabla^2 E - \frac{1}{c^2}\frac{\partial^2 E}{\partial t^2} = \mu_0 \frac{\partial^2 P_L}{\partial t^2} + \mu_0 \frac{\partial^2 P_{NL}}{\partial t^2} \tag{1.1}$$

The key approximations are as follows. First, the electric field is separated into a complex envelope $A(z, t)$, a fast carrier with carrier frequency $\omega_0 = 2\pi f_0$ and longitudinal wavenumber β_0, and a transverse spatial mode profile $F(x, y)$:

$$E(z, t) = F(x, y)A(z, t)e^{i(\beta_0 t - \omega_0 t)}. \tag{1.2}$$

Under the slowly-varying envelope approximation (SVEA), $A(z, t)$ is assumed to vary slowly compared to a carrier cycle in time and to a longitudinal spatial period, as indicated in Eq. 1.3. This allows the temporal carrier to be divided out and the second-order spatial derivative to be neglected.

$$\frac{\Delta\omega}{\omega_0} \ll 1 \qquad\qquad \frac{\partial^2 A}{\partial z^2} \ll 2\beta_0 \frac{\partial A}{\partial z} \tag{1.3}$$

Equation 1.1 is then solved in the frequency domain by separation of variable to yield transverse and longitudinal equations. The dominant term from P_{NL} in glass is the third-order susceptibility $\chi^{(3)}$. We assume that ω_0 is far from any resonance

so that $\chi^{(3)}$ is effectively constant and treat it as a first-order perturbation. This yields an intensity dependant shift $\Delta\beta$ of the propagation constant. The transverse equation 1.4 is an eigenvalue equation yielding the fiber modes $F(x, y)$ and the propagation constant $\beta(\omega)$ from the dielectric constant $\epsilon(\omega)$. The solution method is similar to that of standard dielectric waveguides [4, 5]. The resulting propagation constant is then substituted into the longitudinal propagation equation 1.5.

$$\frac{\partial^2 F}{\partial x^2} + \frac{\partial^2 F}{\partial y^2} + \left(\epsilon(\omega)\frac{\omega^2}{c^2} - \beta^2\right)F = 0 \qquad (1.4)$$

$$2i\beta_0\frac{\partial A}{\partial z} + (\beta^2 - \beta_0^2)A = 0 \qquad (1.5)$$

The net propagation constant β is then separated into the non-linear term $\Delta\beta$ and a linear term $\beta(\omega)$ which includes waveguide and material contributions to chromatic dispersion. The linear part is then expanded into a Taylor series of dispersion order β_n:

$$\beta(\omega) = \sum_{n=0}^{\infty} \frac{\beta_n}{n!}(\omega - \omega_0)^n. \qquad (1.6)$$

Taking $\beta^2 - \beta_0^2 \approx 2\beta_0(\beta - \beta_0)$, transforming Eq. 1.5 back into the time domain and adopting a reference frame matching the group-velocity of the carrier yields a partial differential equation that is first-order in the propagation direction z. The non-linear index change $\Delta\beta$ is related to the intensity dependant refractive index n_2. This gives rise to self-phase modulation (SPM), often the dominant non-linear phenomenon in optical fibers. The effective area of the waveguided beam A_{eff} can be computed from the transverse mode $F(x, y)$ [4].

$$\Delta\beta = \gamma|A|^2 \qquad\qquad \gamma = \frac{n_2\omega_0}{cA_{eff}} \qquad (1.7)$$

So far, we have assumed that the non-linear response P_{NL} is instantaneous by taking $\chi^{(3)}$ to be constant. This generally applies to the non-resonant electronic

contribution, but the molecular vibration response time is typically on the order of 100 fs for glasses. To treat pulses shorter than this, or equivalently with bandwidths greater than a few terahertz, the frequency dependance of P_{NL} must be included using the delayed response $R(t - t')$ [4]. At this approximation order, it is more accurate to also take into account the first time derivative of P_{NL} in Eq. 1.1. This adds a shock-forming term and yields the GNLSE:

$$\frac{\partial A}{\partial z} = \sum_{n=2}^{\infty} i^{n+1} \frac{\beta_n}{n!} \frac{\partial^n A}{\partial t^n} + i\gamma \left(1 + \frac{i}{\omega_0} \frac{\partial}{\partial t}\right) \left(A(z,t) \int_{-\infty}^{t} R(t - t')|A(z,t')|^2 dt'\right). \quad (1.8)$$

1.2.2   Stimulated Raman scattering

The exact expression for the delayed response $R(t - t')$ in Eq. 1.8 can be separated into an instantaneous and delayed part. The delayed molecular response gives rise to stimulated Raman scattering. The relative contribution of each is given by f_R, with $f_R = 0.18$ in fused silica:

$$R(t - t') = (1 - f_R)\delta(t - t') + f_R h_R(t - t'). \quad (1.9)$$

The GNLSE then becomes:

$$\frac{\partial A}{\partial z} = \sum_{n=2}^{\infty} i^{n+1} \frac{\beta_n}{n!} \frac{\partial^n A}{\partial t^n}$$
$$+ i\gamma \left(1 + \frac{i}{\omega_0} \frac{\partial}{\partial t}\right) \left((1 - f_R)A|A|^2 + f_R A \int_{-\infty}^{t} h_R(t - t')|A(t')|^2 dt'\right). \quad (1.10)$$

A simple model for the delayed response $h_R(t - t')$ uses a single damped harmonic oscillator, represented by a Lorentzian vibrational line with a phonon period τ_1 and inverse linewidth τ_2 [6]. For silica, the values are $\tau_1 = 12.2$ fs and $\tau_2 = 32$ fs.

$$h_R(t - t') = \frac{\tau_1^2 + \tau_2^2}{\tau_1 \tau_2^2} e^{-t/\tau_2} \sin(t/\tau_1) \quad (1.11)$$

7

A more complete model of the delayed response includes multiple homogeneous Lorentzian components and gaussian inhomogeneous broadening terms, a so-called intermediate broadening model. The parameter values for fused silica are given in table 1 of Ref. [7].

$$h_R(t - t') = \sum_{i=1}^{13} \frac{A'_i}{\omega_i} e^{-\gamma_i t} e^{-\Gamma_i^2 t^2/4} \sin(\omega_i t) \tag{1.12}$$

We compare the two responses in Figure 1.1. The real part of the response spectrum describes the delayed part of the nonlinear refraction, and the imaginary part is the Raman gain spectrum. The single Lorentzian model account for the Stokes shift as well as the Raman gain bandwidth. The multiple line, intermediate broadening model reproduces the fine structure of the Raman response. For the cases described in this thesis, the fine structure was found to produce little significant difference in the simulation results. However, once the response function has been generated, there is no computational time difference between the single and multi-line models, so that the intermediate broadening model is used.
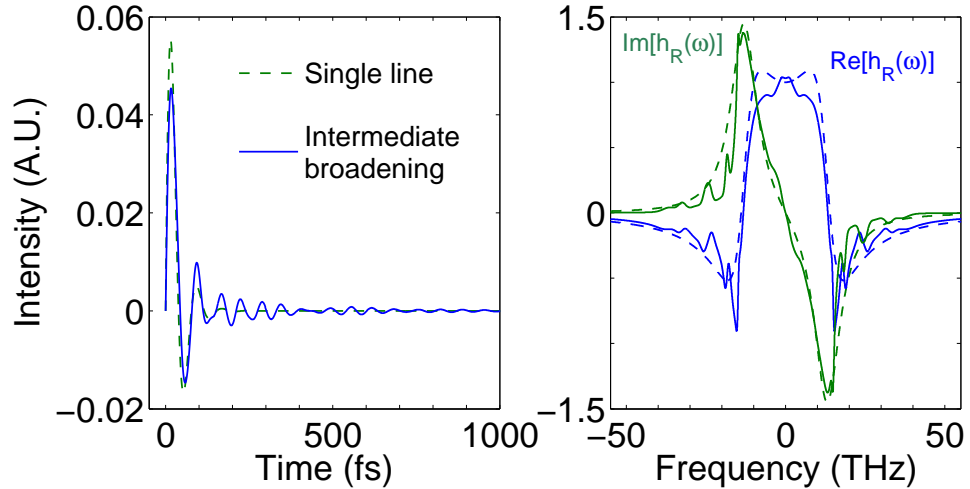
Figure 1.1: Delayed response of fused silica: single (dashed) and multiple (solid) line models. The spectrum shows the even real part and odd imaginary part.

1.2.3 Spontaneous Raman scattering and shot noise

Up to now, the deterministic response of the medium has been included in the GNLSE. To account for certain phenomena, it is necessary to include spontaneous excitations and noise. This is the case for the statistics of sensitive non-linear phenomena such as supercontinuum generation [8], Raman generation [9], optical parametric generation [10] and to study the noise properties of lasers and amplifiers [11, 12]. In optical fibers, the main random excitations are random molecular vibration giving rise to spontaneous Raman scattering and input shot noise.

Spontaneous Raman scattering occurs due to thermal and quantum fluctuations of the molecular vibrational modes. This can me modeled by adding an amplified spontaneous emission (ASE) term $A \cdot \Gamma_R(z, t)$ to the GNLSE [13]. This term is modeled by populating the density of states corresponding to the Raman gain spectrum $\text{Im}[h_R(\Omega)]$ following a Planck distribution of phonons $n_{th}(\Omega)$. Ω is the angular frequency shift from the carrier frequency. This yields the following frequency domain correlation spectrum, with $U(\Omega)$ the Heavyside step function and $\hbar$ is the Planck constant $h/2\pi$:

$$\langle \Gamma_R(\Omega, z)\Gamma_R^*(\Omega', z') \rangle = \frac{2f_R \hbar \omega_0}{\gamma} |\text{Im}[h_R(\Omega)]| \left[n_{th}(|\Omega|) + U(-\Omega) \right] \delta(\Omega - \Omega')\delta(z - z'),$$

$$n_{th}(\Omega) = \left[\exp\left(\hbar\Omega/k_B T \right) - 1 \right]^{-1}. \tag{1.13}$$

This corresponds to a field that is uncorrelated between different frequency bins or propagation steps, but whose average magnitude follows a thermalized Raman gain spectrum. The resulting field in Figure 1.2 clearly shows the higher occupation of the Stokes field vs the Anti-Stokes.

The shot noise describes the photon number fluctuations of the input pulse. This is due to quantum ground state fluctuations of the electric field and cor-
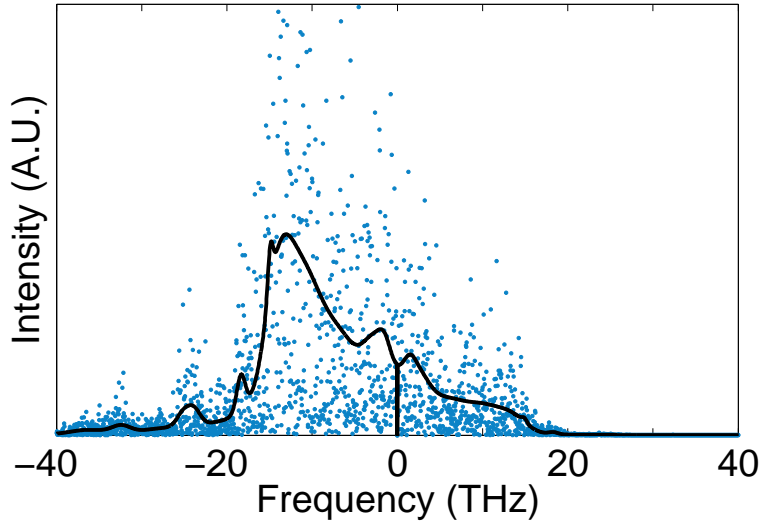
Figure 1.2: Randomly generated Raman ASE field $|\Gamma_R(\Omega)|^2$ (dots) and correlation spectrum (solid line).

responds to a power density of one photon with random phase at each frequency f [11]. The resulting complex fluctuation $\delta A(t)$ have the following correlation spectrum with $\delta(f)$ the Dirac delta function:

$$\langle \delta A^*(f)\delta A(f')\rangle = \frac{hf}{2}\delta(f - f').\tag{1.14}$$

1.2.4 Numerical model

Putting all deterministic and noise terms together, we get the full stochastic GNLSE:

$$\frac{\partial A}{\partial z} = \sum_{n=2}^{\infty} i^{n+1}\frac{\beta_n}{n!}\frac{\partial^n A}{\partial t^n} + i\gamma\left(1 + \frac{i}{\omega_0}\frac{\partial}{\partial t}\right)\left((1 - f_R)A|A|^2\right.$$

$$\left. + f_R A \int_{-\infty}^{t} h_R(t - t')|A(t')|^2 dt' + iA\Gamma_R(t, z)\right).\tag{1.15}$$

The input pulse $A(t, 0)$ is specified and the shot noise $\delta A(t)$ is added. The GNLSE is then integrated to propagate the pulse in steps dz. This is most effi-

ciently done using the split-step Fourier (SSF) method, as described in chapter 2.4 of Ref. [4]. This involves separating the linear dispersive operator $\widehat{D}$ and the non-linear operator $\widehat{N}$. The linear part is computed in the Fourier domain, while the non-linear part is integrated in the time domain using a 4th-order Runge-Kutta integrator.

The accuracy of the split-step method is limited by the commutator $[\widehat{D}, \widehat{N}]$. The symmetric SSF method described in Ref. [4] is accurate up to dz^2. To model phenomena involving very broad bandwidths and higher-order non-linearities, higher accuracy may be needed. The Runge-Kutta interaction picture (RK4IP) method can achieve an accuracy of dz^4, the limit of the Runge-Kutta integrator [14]. The SSF and RK4IP method are described in more details in Appendix A.1. In this thesis, the SSF is used for simulating fiber lasers, while the RK4IP is used to model four-wave mixing and SRS.

Care must be taken in handling the noise terms described by Eqs. 1.13 and 1.14. Rigorously, differential equations with random terms such as Eq. 1.15 must be treated using the methods of stochastic calculus. In order to integrate the equation following the rules of ordinary calculus, a random Ito correction must be added to the deterministic drift term [15]. However, in quantum optics the relative importance of the Ito correction scales inversely with photon number [16]. For the pulses considered in this thesis, this correction can be neglected [9]. The only remaining challenge is to properly discretize the stochastic terms by averaging the noise distribution over the numerical bins. The amplitudes of the numerical noise distributions are thus resolution dependant. Appendix A.2 describes the numerical distributions used to model shot noise and spontaneous Raman scattering.

The model is implemented in FORTRAN as an extension of the program in [17].

1.3 Four-wave mixing in optical fibers

Four-wave mixing is a fundamental non-linear process resulting from frequency mixing by the third-order non-linear response $\chi^{(3)}$ ([4] chapter 10). In this process, three waves mix to generate a fourth wave at a new frequency. As with any parametric mixing process, energy conservation and phase matching must be respected as in Eqs. 1.16-1.17. The photon energy is $\hbar\omega$ and the photon momentum is $\hbar k$ where the wavevector $k = 2\pi n(\omega)/\lambda$, with $n(\omega)$ the effective refractive index.

$$\omega_1 + \omega_2 = \omega_3 + \omega_4 \tag{1.16}$$

$$\Delta k = k_1 + k_2 - k_3 - k_4 = 0 \tag{1.17}$$

Here we will mainly be interested in degenerate FWM where $\omega_1 = \omega_2$. Two pump photons mix to generate a signal and idler pair. The process is illustrated in Figure 1.3.
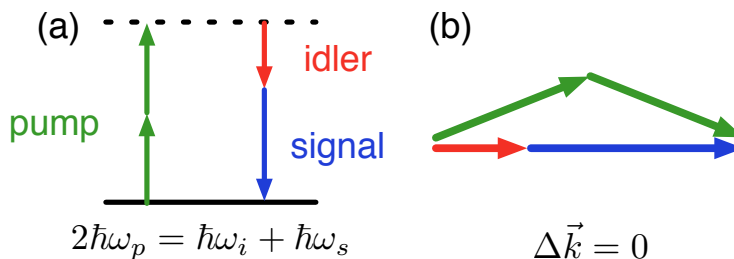
Figure 1.3: Degenerate four-wave mixing constraints: (a) energy conservation and (b) phase-matching.

In the continuous wave (CW) approximation, FWM can be modeled using coupled amplitude equations representing each field [4], or with a single broadband GNLSE [18]. An ansatz $\exp(gz - i\omega t)$ is used with an exponential gain dependance and a frequency shift ω from the pump frequency ω_0. We get a phase-matched

gain spectrum which depends on the non-linear phaseshift γP_0 and the net phase-mismatch κ [8]:

$$g = \sqrt{(\gamma P_0)^2 - (\kappa/2)^2}, \tag{1.18}$$

$$\kappa = 2\gamma P_0 + 2\sum_{n=1}^{\infty} \frac{\beta_{2n}}{(2n)!}(\omega - \omega_0)^{2n}. \tag{1.19}$$

A typical example of the FWM gain spectrum is plotted in Figure 1.4. Two distinct regimes are visible. At anomalous dispersion, g is maximized when the GVD $\beta_2 < 0$ and the SPM γP_0 cancel. The FWM sidebands are broad and close to the pump. This is the mechanism behind the well-know modulation instability at anomalous dispersion. At normal dispersion, the GVD and SPM add up. Higher-order dispersion terms are thus necessary to obtain phase-matching. This results in narrow sidebands far away from the pump frequency.
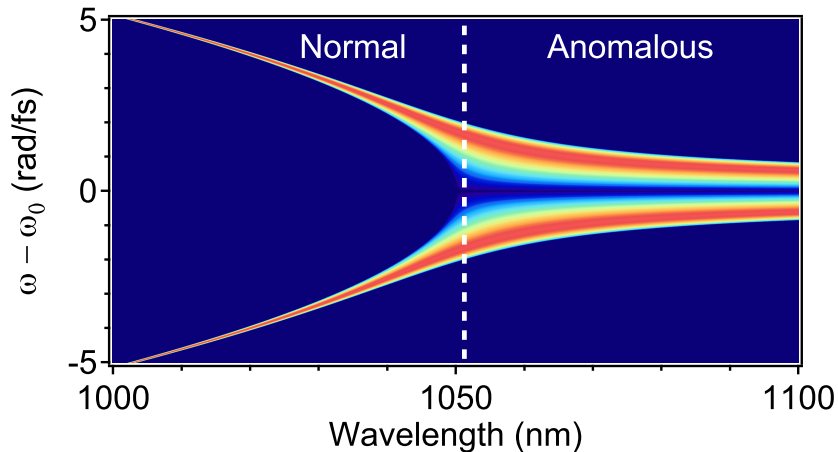
Figure 1.4: Typical gain spectrum for degenerate four-wave mixing. Dotted line indicates the zero-dispersion wavelength. Color scale is logarithmic.

Several mechanisms can be used to satisfy the phase-matching condition in optical fibers [4]. This includes self-phase modulation, the index difference in birefringent optical fibers and intermodal dispersion in multimode fibers. One of the most powerful mechanisms is engineering the waveguide dispersion in photonic

crystal fibers. This allows exquisite control over waveguide dispersion and enable tuning of the FWM phase-matching [18].

For ultrashort pulses, the effects of dispersion must be included in the coupled amplitude equations. This results in a system of coupled NLSE with additional phase-matched terms representing FWM. Alternatively, a single GNLSE with enough higher-order dispersion and non-linear terms can implicitly model the the FWM process. This is the approach used in this thesis.

1.4   Coherent anti-Stokes Raman scattering microscopy

Coherent anti-Stokes Raman scattering microscopy allows label-free biological imaging by exciting intrinsic Raman molecular vibrations [19]. When used in a laser-scanning microscope configuration, this non-linear imaging technique allows high resolution imaging with 3-dimensional sectioning capability. The contrast is based on the variety of vibrational modes present in organic molecules. A typical CARS image is shown in Figure 1.5.
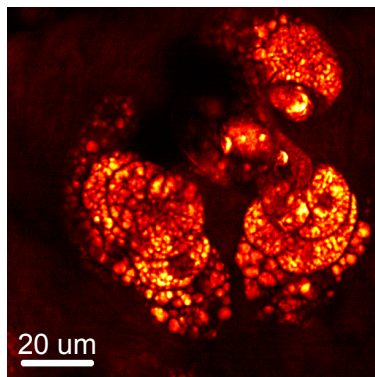
Figure 1.5: CARS microscopy image of the lipid distribution in a sebaceous gland 36 μm deep in a mouse ear. In collaboration with Dan Fu from Harvard University.

Spontaneous Raman scattering is based on the scattering between a pump photon of frequency ω_p and a vibrational mode of frequency ω_{vib}. This creates either a red-shifted Stokes photon or a blue-shifted anti-Stokes photon at frequencies ω_s and ω_{as} respectively. At room temperature, the low density of spontaneously excited vibration modes leads to a low Raman signal and long integration time.

In CARS, a second photon is introduced at the targeted Stokes frequency. The beat between the pump and Stokes coherently drives the vibrational mode. A second pump photon scatters with the driven vibration to produce an anti-Stokes signal with high efficiency. This is illustrated in Figure 1.6.
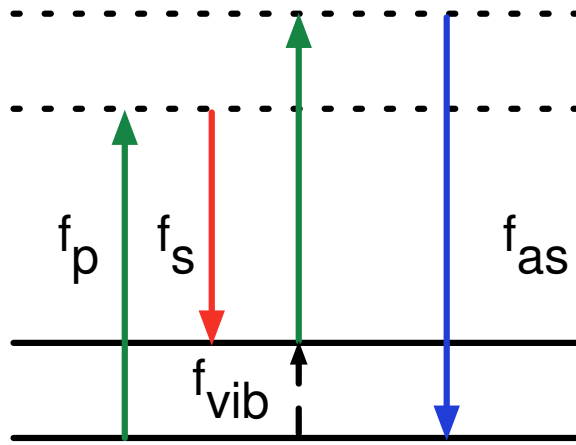
Figure 1.6: Energy level diagram of the CARS process.

CARS corresponds to a resonant three-photon process mediated by the nonlinear susceptibility $P^{(3)}(\omega_{as}) \propto \chi^{(3)} E_p^2 E_s^*$. The resulting anti-Stokes signal is:

$$I_{as} \propto |\chi^{(3)}|^2 I_p^2 I_s \left(\frac{\sin\left(\Delta k L/2\right)}{\Delta k L/2} \right)^2. \tag{1.20}$$

The CARS signal is thus proportional to the square of the concentration of resonators. It is also necessary to minimize the phase-matching Δk. However,

the phase-matching condition is relaxed in the tight focusing geometry used in laser-scanning microscopy [20], so that collinear beams can be used.

The $\chi^{(3)}$ susceptibility for CARS is a combination of a resonant vibrational contribution and a non-resonant electronic contribution due to four-wave mixing. Given a detuning $\Delta = \omega_p - \omega_s - \omega_{vib}$ and a Raman line width Γ, the susceptibility is:

$$\chi^{(3)} = \chi_{NR}^{(3)} + \frac{\chi_R^{(3)}}{\Delta - i\Gamma}. \tag{1.21}$$

This results in a CARS line shape against a flat non-resonant background, The resonant peak is red-shifted and a negative contrast feature appears on the blue side, as shown in Figure 1.7. Several extensions have been developed to suppress the non-resonant background, notably stimulated Raman scattering (SRS) microscopy, which also features a linear dependance on concentration [21].
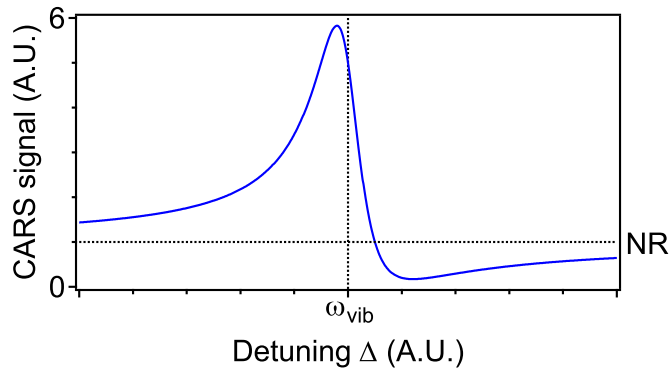
Figure 1.7: Typical CARS line shape. NR marks the non-resonant background.

CARS requires short pulses with high peak power due to the non-linear nature of the response. However, if the pulses are too short, their bandwidth will exceed that of the chosen Raman line, resulting in lower signal versus background and low spectral resolution. Given that most vibrational linewidths in biological samples are on the order of 10-20 cm^{-1}, picosecond pulses are optimal. For biological

imaging, the vibrational frequency of interest are the fingerprint region from 600-1600 cm^{-1} and the CH/water vibrations from 2800-3600 cm^{-1}. Table 1.1 gives the optimal parameters for a CARS microscopy source [19].

Pump wavelength	780-980 nm
Stokes wavelength	1000-1300 nm
Pulse duration	2-7 ps
Spectral bandwidth	3-5 cm^{-1}
Pulse energy	0.1-1 nJ
Repetition rate	50-100 MHz

Table 1.1: Optimal parameters for a CARS microscopy laser source.

1.5 Pulse evolution in fiber lasers and amplifiers

This section discusses a wide range of pulse shaping phenomena occurring in fiber lasers, amplifiers and parametric devices. The interaction between self-phase modulation, dispersion and other pulse shaping elements gives rise to several classes of non-linear waves including solitons, self-similar pulses and dissipative solitons.

1.5.1 Solitons of the non-linear Schrödinger equation

Solitary waves are solutions to wave equations that preserve their shape despite dispersive effects such as diffraction or chromatic dispersion. Beyond their interesting mathematical and physical properties, their fixed shape and stability properties can be useful for applications such as communications, remote sensing and pulse shaping. Solitons are a special class of non-linear solitary waves that follow discrete conservation and interaction rules.

The basic non-linear Schrödinger equation (NLSE) supports soliton solutions

that can be readily observed in optical fibers. First, consider the NLSE with SPM and group velocity dispersion (GVD) β_2 as the dominant effects:

$$\frac{\partial A}{\partial z} = -i\frac{\beta_2}{2}\frac{\partial^2 A}{\partial t^2} + i\gamma A|A|^2. \tag{1.22}$$

Given the right pulse pulse shape $A(z,t)$, we can expect the phase modulation due to SPM and GVD to balance and form a stable pulse shape. A full solution of the NLSE is possible using the inverse scattering method, as described in chapter 5.2 of [4]. In the case of anomalous dispersion $\beta_2 < 0$ we can verify by substitution that Eq. 1.22 has the solution:

$$A(t,z) = \sqrt{P_0}\text{sech}(t/T_0)e^{i\frac{\beta_2}{2T_0^2}z}. \tag{1.23}$$

Eq. 1.23 has a fixed temporal profile for all z and is the fundamental soliton of the NLSE. It the lowest-order member of a family of NLSE solution with periodically recurring pulse shapes [4]. They are defined by a soliton number N:

$$N^2 = \frac{\gamma P_0 T_0^2}{|\beta_2|}. \tag{1.24}$$

By substituting Eq. 1.23 into Eq. 1.22, we can verify that the fundamental soliton corresponds to $N = 1$. This yields the soliton area theorem, which links together the pulse duration and energy of the soliton.

The NLSE describes passive pulse propagation, for instance in an optical fiber communication link. However, it can extended to fiber lasers by using an average cavity model yielding a master equation of the cubic Ginzburg-Landau (CGLE) type [22]. For negative average cavity dispersion, the soliton solution Eq. 1.23 remains unchanged as long as average cavity parameters are used.

Soliton mode-locking of fiber lasers imposes strict restrictions on pulse energy due to the area theorem. For typical single-mode fibers, this typically limits the

pulse energy to 10s of picojoule for sub-picosecond pulses [23]. The pulse energy can be increased using the dispersion-managed soliton or stretched-pulse cavity design [24]. By alternating segments of normal and anomalous dispersion, the pulse breathes inside the cavity and the average peak power is reduced, enabling higher stable pulse energies. Bringing the net cavity dispersion close to zero also yield shorter dechirped pulses. Stretched-pulse modelocking can be described by a chirped gaussian solution to the master equation [25]. Stretched-pulse lasers based on Yb-doped fibers can reach pulse duration below 100 fs with energies approaching 1 nJ [26].

1.5.2   Similariton pulse evolution in fiber lasers

The pulse energy limitation of soliton and stretched-pulse lasers stems from the limited amount of non-linear phase Φ_{NL} these pulses can tolerate. In the presence of dispersion, non-linear phase will generally start distorting pulse for $\Phi_{NL} > 1$ [27]. To scale fiber lasers to higher energies, pulse evolutions capable of tolerating larger non-linear phase are necessary.

One of the main limits to non-linear phase accumulation is wave-breaking. This occurs when two colors of the same pulse overtake each other and overlap in time, corresponding to a non-monotonic frequency sweep [28]. This leads to intra-pulse interference in the time domain and non-linear mixing leading to spectral sidebands. However, certain pulse shapes can accumulate non-linear phase while maintaining a monotonic chirp. A simple example of these wave-breaking free pulses is the parabolic solution to the normal dispersion NLSE, valid in the high non-linearity regime [29]. Such parabolic pulses generate a linear frequency sweep $\delta\omega(t) = -\partial\phi/\partial t$ through SPM, avoiding wave-breaking and enabling simple com-

pensation with negative GVD compressors. They are an example of self-similar waves with evolving parameters but fixed normalized shapes. When implemented in a net-normal dispersion Yb-doped fiber laser, the passive parabolic pulse can reach 10 nJ output pulse energy and dechirp to 100 fs [30].

The NLSE with normal dispersion and gain also has self-similar parabolic solutions [31]. Consider the following equation with g the gain coefficient per unit length:

$$\frac{\partial A}{\partial z} = -i\frac{\beta_2}{2}\frac{\partial^2 A}{\partial t^2} + i\gamma A|A|^2 + \frac{g}{2}A. \tag{1.25}$$

The general solution of Eq. 1.5.2 requires numerical simulations. However, in the limit $z \to \infty$, there is an asymptotic parabolic solution of the form:

$$A(z,t) = A_0(z)\sqrt{1-(t/T_0(z))^2}e^{i\phi(z,t)}, \qquad |t| \le T_0(z). \tag{1.26}$$

This parabolic similariton continuously grows in duration, amplitude and bandwidth due to the combined action of GVD, gain and SPM:

$$A_0(z) = 0.5(gE_{in})^{1/3}(\gamma\beta_2/2)^{-1/6}e^{gz/3}, \tag{1.27}$$

$$T_0(z) = 3g^{-2/3}(\gamma\beta_2 E_{in}/2)^{1/3}e^{gz/3}, \tag{1.28}$$

$$\phi(z,t) = \phi_0 + 3\gamma(2g)^{-1}A_0^2(z) - g(6\beta_2)^{-1}t^2, \tag{1.29}$$

$$\delta\omega(t) = -\partial\phi/\partial t = g(3\beta_2)^{-1}t. \tag{1.30}$$

The instantaneous frequency $\delta\omega(t)$ is linear as expected from the SPM of a parabolic intensity profile. The pulse should thus dechirp close to its transform-limited duration. The chirp $-\partial^2\phi/\partial t^2 = g(3\beta_2)^{-1}$ is constant, a consequence of self-similarity.

The output pulse is determined solely by E_{in}, not the other initial pulse parameters or shape. Numerical simulations show that arbitrary input pulse will asymptotically evolve toward the similariton solution, as in Figure 1.8. The amount of propagation required depends on how far the input pulse is from the asymptotic solution.
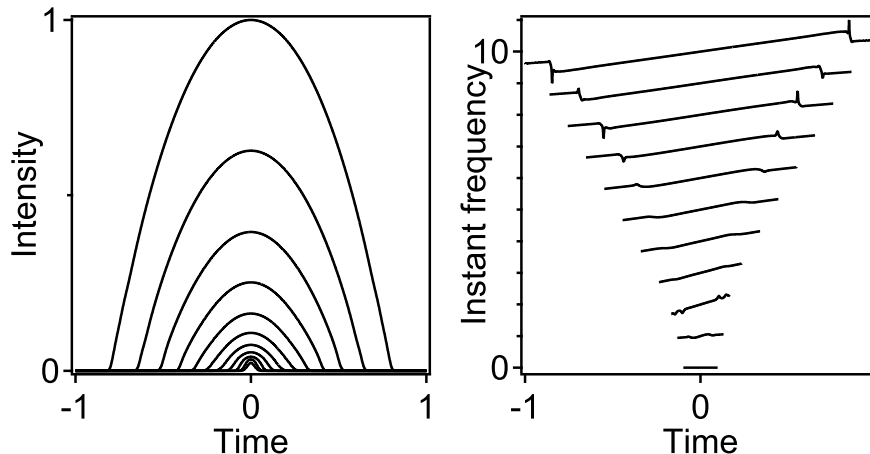
Figure 1.8: Evolution of an input gaussian pulse into a parabolic similariton in a gain fiber.

The active similariton of Eq. 1.26 is well studied in fiber amplifiers, where it can lead to hundreds of nanojoules and sub-100 fs duration with LMA fibers [32]. However, implementing such pulse evolution in a fiber laser cavity requires a mechanism to ensure self-consistency despite the monotonically evolving similariton propagation. Recently, it was shown that similaritons can be formed in the gain segment of fiber lasers through self-consistent seeding conditions such as a dual soliton-similariton design [33], or by introducing a very narrow spectral filter [34, 35]. The seed pulse for each roundtrip is then a near-transform-limited gaussian pulse close to the asymptotic evolution. The pulse reshapes into a parabolic form as it propagates through the gain fiber and undergoes large spectral broadening. With single-mode Yb-doped fiber, spectral breathing ratios of more than 20 are possi-

ble at pulse energies of several nanojoules and dechirped durations approaching 50 fs [34].

1.5.3   Dissipative solitons in normal dispersion fiber lasers

Until recently, it was considered general knowledge that fibers lasers required some amount of anomalous dispersion to ensure self-consistency, either through soliton formation or dispersion compensation. With only normal dispersion, the pulses would undergo continuous dispersive broadening and never converge to a stable cavity state.

However, it was recently shown that negative dispersion is not the only mechanism that can ensure self-consistent temporal evolution of pulses in a fiber laser. By adding a spectral filter inside an all-normal dispersion fiber laser, stable mode-locking can be obtained [36]. This is because for highly chirped pulses, the frequency components are spread across time. Thus, a spectral filter which cuts the spectral edges of the pulse will also cut its temporal edges. This results in a fiber laser with large spectral and temporal breathing. The spectral filter can be an explicit discrete filter [36] or an implicit filtering effect such as gain bandwidth [37] or the the frequency dependance of non-linear polarization evolution [38].

The pulse shaping of ANDi lasers is very flexible and can produce a wide range of pulses [39]. The output pulses are highly chirped with effective dispersions typically larger than the intra-cavity dispersion. Non-linear phases up to $\Phi_{NL} \sim 10\pi$ can be tolerated. This enables high pulse energies ranging from several nanojoules to above 20 nJ in single-mode fiber [40]. Pulse durations below 100 fs can be reached by minimizing the net cavity dispersion [41, 42]. At

very large cavity dispersion, pulses with greater than 100 ps chirped duration and sub-picosecond dechirped duration are produced, simplifying chirped-pulse fiber amplifier systems [43].

The pulse shaping in ANDi lasers is well described by a dissipative soliton model [44]. Whereas the NLSE soliton balances phase modulations from GVD and SPM, dissipative solitons balance phase and amplitude modulations. By including dissipative effects in the NLSE such as net gain, spectral filtering and saturable absorption, we get a normalized cubic-quintic Ginzburg-Landau equation (CQGLE):

$$\frac{\partial U}{\partial z} = gU + \left(\frac{1}{\Omega} - i\frac{D}{2}\right)\frac{\partial^2 U}{\partial t^2} + (\alpha + i\gamma)|U|^2 U + \delta|U|^4 U. \qquad (1.31)$$

Equation 1.31 describes the average cavity dynamics. The average dispersion is D and the non-linear SPM coefficient is γ. Dissipative effects include the net gain and loss per unit length g, the spectral filter bandwidth Ω and the cubic and quintic saturable absorber terms α and δ. The CQGLE admits a generalized chirped sech-like solution:

$$U(z,t) = \sqrt{\frac{A}{\cosh(t/\tau) + B}} \exp\left(-i\beta/2\ln\left(\cosh(t/\tau) + B\right) + i\theta z\right). \qquad (1.32)$$

The parameters A, β, τ and θ are set by the cavity parameters [44]. By tuning the free parameter B, a broad class of pulse and spectral shapes can be produced as shown in Figure 1.9. This reproduces well the range of pulses observed in ANDi fiber lasers.
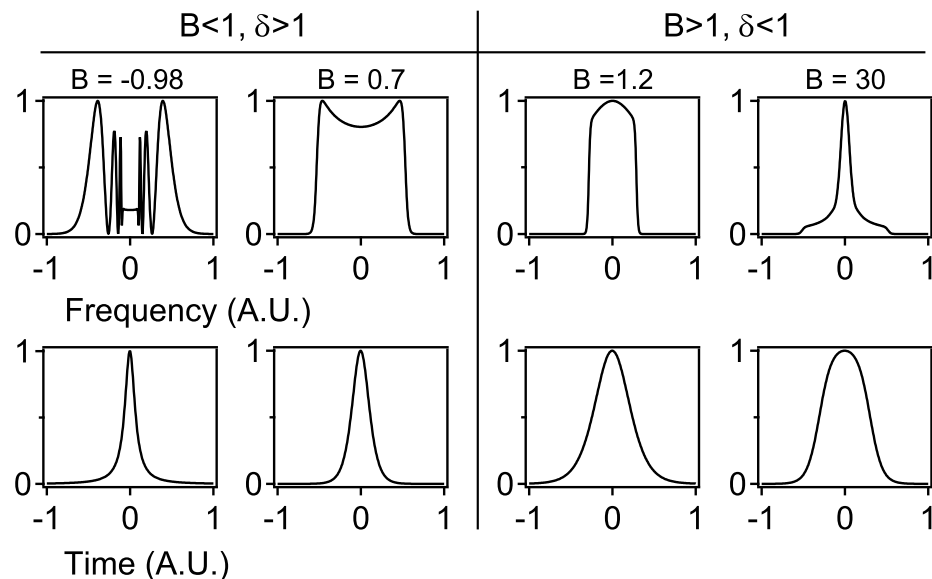
Figure 1.9: Dissipative soliton spectra (top) and pulses (bottom) for different values of B in Eq. 1.32. Parameters are $\Omega = 1$, $D = 5$, $\gamma = 0.1$ and $|\delta| = 10$. β is phenomenologically set to 10.

1.6 Components for amplitude control in fiber lasers

This section describes key pulse shaping components for fiber lasers. Saturable absorbers and spectral filters used in this thesis are discussed.

1.6.1 Saturable absorbers

The generation of ultrashort pulses from a laser cavity requires a fixed phase relationship between the different modes supported by the cavity. This is referred to as mode-locking. Although mode-locking is straightforward to describe in the frequency domain, in practice it is difficult to control the spectral phase of each mode.

Instead, an element is introduced in the laser cavity to promote pulse formation.

A saturable absorber provides high loss at low input intensity and high transmission at high intensity. Short pulses experience lower loss than cw operation and background noise, thus mode-locking is enforced in the time-domain. The simple model used in this thesis for the transmission $T(t)$ of a saturable absorber depends on the instantaneous power $P(t)$, the modulation depth l_0 and the saturation power P_{sat} [30]:

$$T(t) = 1 - \frac{l_0}{1 + P(t)/P_{sat}}.$$
(1.33)

An example saturable absorber curve and its effects on an input gaussian pulse are shown in Figure 1.10. The saturable absorber has two effect. First, it suppresses background fluctuations, helping suppress noise spurs. Second, pulses are shortened, stabilizing pulse formation. These effects are optimal if the pulse peak power lies on the high slope part of the saturable absorber curve.
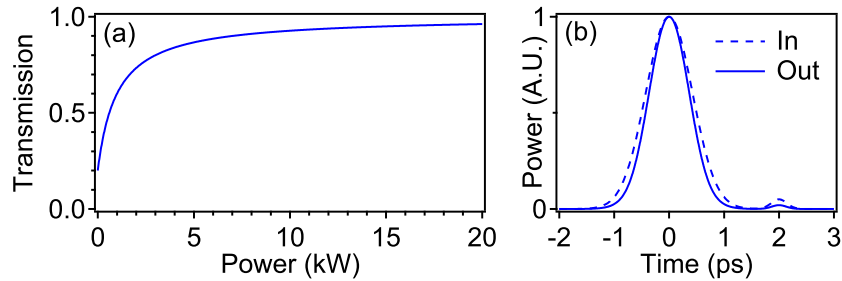
Figure 1.10: (a) Saturable absorber curve from Eq. 1.33 with l_0=0.8 and P_{sat}=1 kW. (b) Normalized 1 kW peak power pulse before and after the saturable absorber.

Saturable absorbers include molecular dyes, semiconductor saturable absorber mirrors (SESAM), carbon nanotubes and graphene. Artificial saturable absorbers can be created by converting a non-linear phase modulation into an intensity dependent transmission, such as in a non-linear optical loop mirror (NOLM) or in non-linear polarization evolution (NPE).

Non-linear polarization evolution

In this thesis, NPE will be the main saturable absorber used. NPE occurs when elliptically polarized light travels through a non-linear medium of length L. Cross-phase modulation between the two polarization components results in an intensity-dependent polarization rotation. Working in a circular polarization basis, the rotation angle is $\Delta\theta$ [45]:

$$\Delta\theta = \frac{\gamma L}{3}(|E_+|^2 - |E_-|^2). \tag{1.34}$$

If a polarizer is placed after the non-linear medium, an intensity-dependent transmission is obtained, thus converting NPE into artificial saturable absorption. The response time is that of the electronic non-linearity, which can be considered instantaneous even for pulses are short as tens of femtoseconds.

To control the NPE transmission curve, polarization controllers are introduced. The configuration used in this thesis used two quarter-wave plates and one half-wave plate as illustrated in Figure 1.11. The first quarter-wave plates converts the polarization to elliptical, while the two other wave plates align the polarization out of the non-linear medium with the output polarizer.
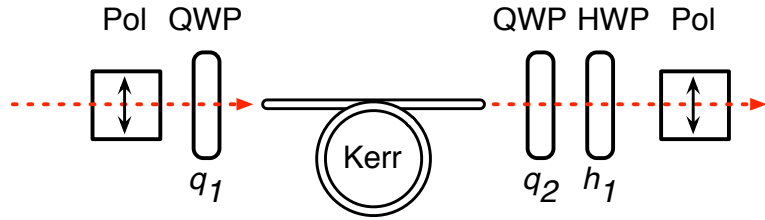
Figure 1.11: NPE configuration for fiber lasers. Pol: polarizer, HWP/QWP: half/quarter-wave plates with angles q_1, q_2 and h_1.

A wide range of saturable absorber curves can be obtained by adjusting the angles of the three waveplates. The transmission of the NPE configuration in

Figure 1.11 can be calculated using Jones matrix algebra [45]:

$$T = \frac{1}{2}\big[1 - \sin 2q_1 \sin 2q_2 + \cos 2q_1 \cos 2q_2 \cos\left(2(q_1 + q_2 - 2h_1 + \Delta\theta)\right)\big]. \quad (1.35)$$

1.6.2 Spectral filters

Spectral filters can be used for pulse shaping and stabilization of fibers lasers. In particular, they are critical elements in dissipative soliton and amplifier similariton fiber lasers. This section describes the birefringent and grating filters which will be used in this thesis.

Birefringent filter

A birefringent filter is obtained by placing a birefringent element of thickness d in front of a polarizer [46]. The ordinary and extraordinary waves with refractive indices n_o and n_e will experience a phase delay $\Delta\phi$:

$$\Delta\phi = \frac{2\pi}{\lambda}(n_e - n_o)d. \quad (1.36)$$

For a fixed retardation $\Delta\phi$, the polarization rotation will depend on the optical frequency. The polarizer converts this to a frequency-dependent transmission. At normal incidence and a linear polarization 45° from both axes, the resulting filter has a cosine squared profile as shown in Figure 1.12(a):

$$T = \cos^2\left(\Delta\phi/2\right). \quad (1.37)$$

Filter bandwidths from a few nanometers to more than 20 nm can be obtained in the near-infrared using several millimeter thick quartz plates ($n_e = 1.54333$,

27

$n_o = 1.53457$ around 1030 nm [47]). The filter bandwidth increases for thinner plates and can be calculated from Eq. 1.37 as shown in Figure 1.12(b).
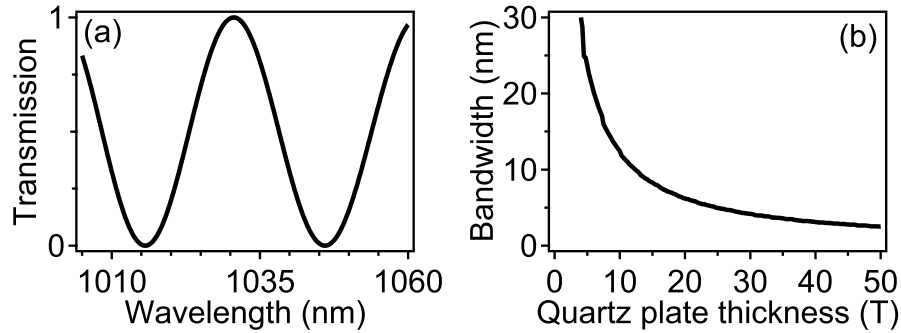
Figure 1.12: (a) Birefringent filter profile for a 4 mm thick quartz plate. (b) Full-width half maximum (FWHM) bandwidth of quartz plate birefringent filters around 1030 nm (1 T ≈ 0.5 mm). All filters at normal incidence and polarization 45° from the optical axis.

Grating filter

A diffraction grating spreads the colors of a beam at different angles. By placing an aperture after the grating, the angular dispersion can be converted into spectral filtering. A optical fiber and a focusing lens can be used as the aperture. The numerical aperture (NA) of the fiber samples the dispersed beam and creates a single-peaked gaussian filter. For typical groove densities and single-mode fibers, this can be used to create high-quality filters with bandwidths of a few nanometers [34].

The grating filter profile can be modeled using the ABCDEF gaussian beam matrix formalism [48]. The full derivation of the filter profile is beyond the scope of this thesis, so here I will present relevant experimental results. Rigorously, the filter bandwidth depends on the grating-fiber distance, incidence angles and

grating groove density. However, for distance less than 20 cm, the grating groove density is the dominant parameter.

A typical grating filter profile applied to an ASE spectrum are shown in Figure 1.13. The fiber has a 33 um core diameter with a NA of 0.06. Coupling is done with a 19 mm focal length lens 10 cm from the grating. The center wavelength can be tuned by rotating the grating, and filter bandwidths between 2 nm and 5 nm can be obtained with 600 ln/mm and 300 ln/mm gratings respectively.
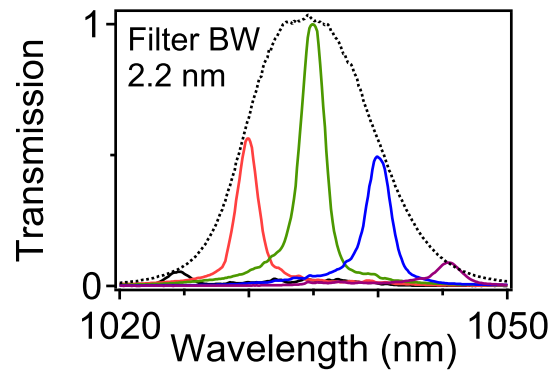
Figure 1.13: Grating-fiber filter acting on the ASE of Yb (dotted line) using a 600 lines/mm grating and $d = 33$ um core NA $= 0.06$ fiber.

Bibliography

[1] J. D. Kafka, M. L. Watts, and J. Pieterse, IEEE J. Quantum Electron. **28**, 2151 (1992).

[2] G. R. Holtom, Opt. Lett. **31**, 2719 (2006).

[3] S. V. Marchese, C. R. E. Baer, A. G. Engqvist, S. Hashimoto, D. J. H. C. Maas, M. Golling, T. Südmeyer, U. Keller, and T. Suedmeyer, Opt. Express **16**, 6397 (2008).

[4] G. P. Agrawal, *Nonlinear Fiber Optics*, 3rd ed. (Academic Press, New York, 2001).

[5] D. Marcuse, *Theory of Dielectric Waveguides* (Academic Press, New York, 1974).

[6] K. J. Blow and D. Wood, IEEE J. Quantum Electron. **25**, 2665 (1989).

[7] D. Hollenbeck and C. D. Cantrell, J. Opt. Soc. Am. B **19**, 2886 (2002).

[8] J. M. Dudley, G. Genty, and S. Coen, Rev. Mod. Phys. **78**, 1135 (2006).

[9] I. I. I. Headley C. and G. P. Agrawal, IEEE J. Quantum Electron. **31**, 2058 (1995).

[10] S. Lefrancois, D. Fu, G. R. Holtom, L. Kong, W. J. Wadsworth, P. Schneider, R. Herda, A. Zach, X. S. Xie, and F. W. Wise, Opt. Lett. **37**, 1652 (2012).

[11] R. Paschotta, Appl. Phys. B-Lasers O. **79**, 153 (2004).

[12] R. Paschotta, Appl. Phys. B-Lasers O. **79**, 163 (2004).

[13] F. X. Kärtner, D. J. Dougherty, H. A. Haus, and E. P. Ippen, J. Opt. Soc. Am. B **11**, 1267 (1994).

[14] J. Hult, J. Lightwave Technol. **25**, 3770 (2007).

[15] M. J. Werner and P. D. Drummond, J. Comput. Phys. **132**, 312 (1997).

[16] S. J. Carter, Phys. Rev. A **51**, 3274 (1995).

[17] F. O. Ilday, Ph.D. thesis, Cornell University, 2004.

[18] W. H. Reeves, D. V. Skryabin, F. Biancalana, J. C. Knight, P. S. Russell, F. G. Omenetto, A. Efimov, and A. J. Taylor, Nature **424**, 511 (2003).

[19] C. L. Evans and X. S. Xie, Annu. Rev. Anal. Chem. **1**, 883 (2008).

[20] A. Zumbusch, G. R. Holtom, and X. S. Xie, Phys. Rev. Lett. **82**, 4142 (1999).

[21] C. W. Freudiger, W. Min, B. G. Saar, S. Lu, G. R. Holtom, C. He, J. C. Tsai, J. X. Kang, and X. S. Xie, Science **322**, 1857 (2008).

[22] H. A. Haus, J. G. Fujimoto, and E. P. Ippen, J. Opt. Soc. Am. B **8**, 2068 (1991).

[23] K. Tamura, H. A. Haus, and E. P. Ippen, Electron. Lett. **28**, 2226 (1992).

[24] K. Tamura, E. P. Ippen, H. A. Haus, and L. E. Nelson, Opt. Lett. **18**, 1080 (1993).

[25] H. A. Haus, K. Tamura, L. E. Nelson, and E. P. Ippen, IEEE J. Quantum Electron. **31**, 591 (1995).

[26] H. Lim, F. O. Ilday, and F. W. Wise, Opt. Lett. **28**, 660 (2003).

[27] F. W. Wise, A. Chong, and W. H. Renninger, Laser Photonics Rev. **2**, 58 (2008).

[28] D. Anderson, M. Desaix, M. Lisak, and M. L. Quiroga-Teixeiro, J. Opt. Soc. Am. B **9**, 1358 (1992).

[29] D. Anderson, M. Desaix, M. Karlsson, M. Lisak, and M. L. Quiroga-Teixeiro, J. Opt. Soc. Am. B **10**, 1185 (1993).

[30] F. O. Ilday, J. R. Buckley, W. G. Clark, and F. W. Wise, Phys. Rev. Lett. **92**, 213902 (2004).

[31] M. E. Fermann, V. I. Kruglov, B. C. Thomsen, J. M. Dudley, and J. D. Harvey, Phys. Rev. Lett. **84**, 6010 (2000).

[32] Y. Deng, C.-Y. Chien, B. G. Fidric, and J. D. Kafka, Opt. Lett. **34**, 3469 (2009).

[33] B. Oktem, C. Ulgudur, and F. O. Ilday, Nat. Photon. **4**, 307 (2010).

[34] W. H. Renninger, A. Chong, and F. W. Wise, Phys. Rev. A **82**, 21805 (2010).

[35] C. Aguergaray, D. Méchin, V. Kruglov, and J. D. Harvey, Opt. Express **18**, 8680 (2010).

[36] A. Chong, J. Buckley, W. Renninger, and F. Wise, Opt. Express **14**, 10095 (2006).

[37] L. M. Zhao, D. Y. Tang, and J. Wu, Opt. Lett. **31**, 1788 (2006).

[38] W. S. Man, H. Y. Tam, M. S. Demokan, P. K. A. Wai, and D. Y. Tang, J. Opt. Soc. Am. B **17**, 28 (2000).

[39] A. Chong, W. H. Renninger, and F. W. Wise, J. Opt. Soc. Am. B **25**, 140 (2008).

[40] A. Chong, W. H. Renninger, and F. W. Wise, Opt. Lett. **32**, 2408 (2007).

[41] A. Chong, W. H. Renninger, and F. W. Wise, Opt. Lett. **33**, 2638 (2008).

[42] N. B. Chichkov, C. Hapke, J. Neumann, D. Kracht, D. Wandt, and U. Morgner, Opt. Express **20**, 3844 (2012).

[43] W. H. Renninger, A. Chong, and F. W. Wise, Opt. Lett. **33**, 3025 (2008).

[44] W. H. Renninger, A. Chong, and F. W. Wise, Phys. Rev. A **77**, 023814 (2008).

[45] K. R. Tamura, Ph.D. thesis, Massachusetts Institute of Technology, 1994.

[46] J. W. Evans, J. Opt. Soc. Am. **39**, 229 (1949).

[47] G. Ghosh, Opt. Commun. **163**, 95 (1999).

[48] A. A. Tovar and L. W. Casperson, J. Opt. Soc. Am. A **14**, 882 (1997).

CHAPTER 2

A TWO-COLOR PICOSECOND FIBER LASER FOR COHERENT ANTI-STOKES RAMAN SCATTERING MICROSCOPY[1]

Here we present a fiber-based picosecond source for CARS microscopy. Frequency conversion is achieved by four-wave mixing in normal-dispersion photonic crystal fiber (PCF). Seeding the process mitigates GVM and suppresses noise. Pulses from a 1 μm fiber amplifier are converted to around 800 nm with up to 160 mW of average power and durations around 2 ps. Frequency shifts in the range 2650 cm^{-1} to 3200 cm^{-1} have been achieved. We use this system to image mouse brain and skin tissues, as well as single cells. To our knowledge, this is the first fiber instrument to offer performance comparable to solid-state systems.

2.1   Introduction

Coherent anti-Stokes Raman scattering (CARS) microscopy allows label-free biological imaging by exciting intrinsic molecular vibrations [4]. Several extensions have been developed, notably stimulated Raman scattering (SRS) microscopy, which enables background-free quantitative imaging [5]. However, CARS requires two synchronized picosecond pulse trains with bandwidths smaller than the relevant Raman linewidth and a frequency spacing tunable to the Raman shift of interest. This is generally accomplished using a solid-state Nd-doped laser that is frequency-doubled to synchronously pump an optical parametric oscillator (OPO) [6]. Such bulk laser cavities are complex and require careful alignment and maintenance, limiting the use of CARS microscopy outside specialized laboratories.

---

[1]Much of the work presented in this chapter was published in Optics Letters and the Proceedings of SPIE [1, 2, 3].

A turn-key source based on optical fiber technology would make CARS more accessible to users in general biology and clinical settings. An early attempt used the continuum from a PCF to perform multiplex CARS spectroscopy [7]. Later, a two-color femtosecond fiber laser for CARS microscopy was built using soliton self-frequency shifting [8]. A femtosecond fiber laser and fiber-OPO system can be used for multimodal CARS/two-photon fluorescence [9]. To maximize spectral resolution and contrast, picosecond sources are desirable. A frequency-doubled fiber laser/amplifier can pump a bulk OPO [10]. A fiber-based time-lens system can be electronically synchronized with a picosecond Ti:Sapphire laser [11]. However, these two systems require one bulk oscillator. A two-color Er-doped fiber system was realized using highly nonlinear fiber and periodically-poled lithium niobate (PPLN) [12]. Another method combines a spectrally sliced supercontinuum and frequency doubling in PPLN [13]. Electronically synchronized actively modelocked fiber lasers provide rapid spectral tuning [14]. However, limited pulse energy in the two former and longer pulse duration in the latter yield peak powers lower than from conventional solid-state systems.

A major challenge is to find a fiber-based frequency-conversion scheme scalable to high powers. Several mechanisms have been proposed, including dispersive wave generation and four-wave mixing (FWM).

Dispersive wave generation occurs when the spectrum of a higher order soliton expands into frequencies where the dispersion turns normal due to higher-order terms. A resonance condition can occur due to dispersion-mediated phase-matching, causing energy to be channeled into a separate non-solitonic wave [15]. The dispersive wave lags behind the soliton with a fixed angle in the time-propagation plane, analogous to the Cherenkov radiation emitted by charged par-

ticles. Dispersive waves are often observed during supercontinuum generation in PCF and contribute to the normal-dispersion side of the continuum [16]. Dispersive wave generation was proposed as an efficient and tunable method to convert infrared femtosecond pulses to the visible [17]. Whether this conversion scheme can be scaled to the pulse durations and energies required for CARS microscopy remains an open question.

Four-wave mixing in photonic crystal fiber has been used to convert 50-200 picosecond pulses to large frequency shifts [18, 19]. However, unseeded FWM leads to large deviations from the transform limit and significant fluctuations in the converted pulses [20], both of which are detrimental to CARS imaging. Additionally, the broadband white noise the FWM signal grows from results in bandwidths of several nanometers for the generated pulses. Transform-limited pulses with spectra that just fill the CARS vibrational linewidth ($\sim$10 cm^{-1}) would be optimal. Moreover, for the desired few-picosecond pulses, interaction lengths are only tens of centimeters due to group-velocity mismatch (GVM), which limits FWM conversion. As a result of these issues, CARS microscopy of biological samples with a fiber-FWM source had not been demonstrated when this project was initiated.

Here we present a two-color picosecond fiber laser for CARS microscopy. Fiber-based frequency conversion mechanisms are modeled. A high-energy picosecond fiber amplifier system is described and frequency shifted using FWM in PCF. CARS microscopy of biological samples using this new fiber laser is presented. Finally, the noise properties of the laser are discussed.

2.2 Dispersive waves for frequency conversion

Here we will study the scaling of dispersive wave generation to the few nanojoule picosecond pulse regime required for CARS microscopy. For the dispersive wave to form, its phase must match that of the soliton in its frame of reference, yielding the phase-matching condition [16] in Eq. 2.1. The pump soliton frequency is ω_p, the dispersive wave frequency is ω_d and the non-linear phase is γP_0.

$$\Delta k = \sum_{n=2}^{\infty} \frac{\beta_n}{n!}(\omega_d - \omega_p)^n - \gamma P_0 = 0 \tag{2.1}$$

Using the phase-matching condition, the dispersive wave conversion frequency can be calculated. Figure 2.1 presents the phase-matching diagram for several commercial non-linear PCFs (NKT Photonics, Denmark). For simplicity, the non-linear phaseshift is set to zero since the typical correction is on the order of 10% [17].
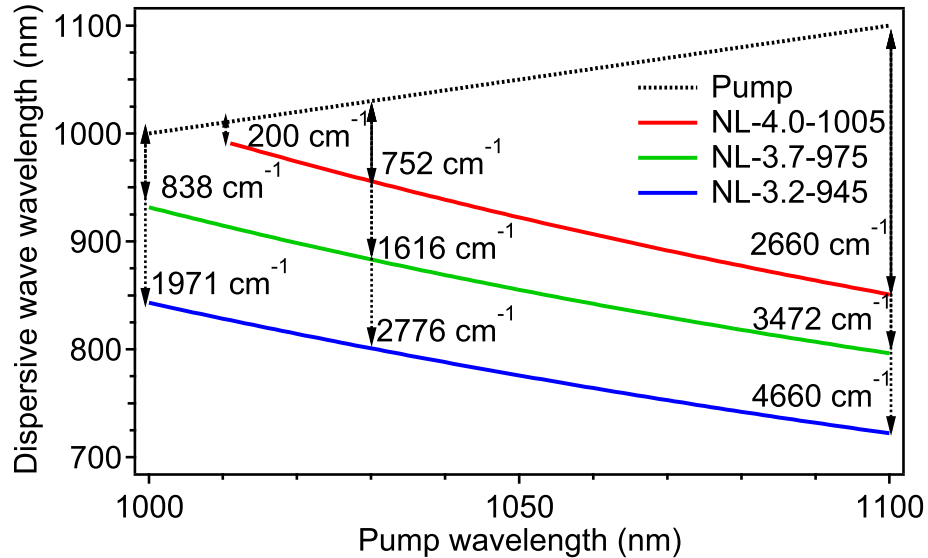
Figure 2.1: Dispersive wave phasematching diagram for commercial PCFs in the linear regime

The diagram indicates that frequency shifts relevant for CARS can be generated by pumping these fibers around 1 μm. In particular, the NL-3.2-945 PCF can generate a shift of about 2800 cm^{-1} when pumped by an Yb-doped fiber laser around 1030 nm.

The performance of the dispersive wave conversion can be assessed by modeling the pulse propagation with the GNLSE Eq. 1.15. We first model the femtosecond regime using sech^2 input pulses at 1025 nm with 0.17 nJ energy and 100 fs duration, corresponding to a soliton number N=3. The NL-3.2-945 PCF has a non-linear parameter $\gamma = 23$ (W km)$^{-1}$ and the dispersion coefficients used are $\beta_2 = -12.3$ fs^2/mm, $\beta_3 = 83.9$ fs^3/mm, $\beta_4 = -94.2$ fs^4/mm and $\beta_5 = 420$ fs^5/mm. The results are presented in Figure 2.2, where the propagation distance is normalized to the soliton period $z_0 = \pi/2 \cdot L_D$.
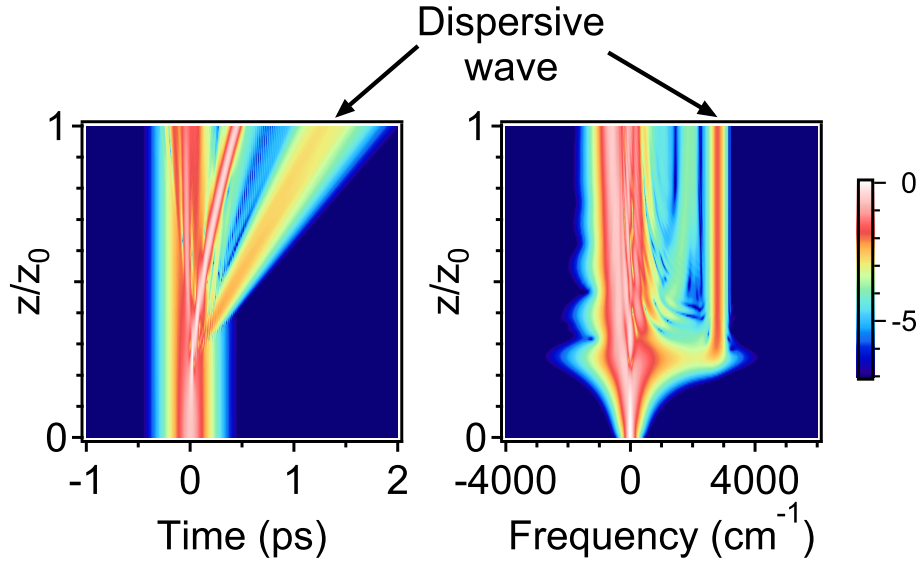
Figure 2.2: Dispersive wave generation from a 100 fs N=3 soliton in NL-3.2-945 PCF.

A dispersive wave indeed forms around 2800 cm^{-1} with about 2% conversion efficiency. It can be recognized in time as it lags behind the main pulse and

broadens due to the normal dispersion. In contrast, the main soliton undergoes fission due to Raman scattering and the resulting fundamental solitons maintain their duration.

The dispersive wave process is scaled to higher energies in Figure 2.3. For a N=6 soliton, the dispersive wave has shifted to 3400 cm^{-1} and the conversion efficiency is now 12%. However, complex spectral features begin to form, indicating the onset of supercontinuum generation. Indeed, for N=8 and above, the dispersive wave blends into the supercontinuum and becomes more structured with a lower conversion efficiency. It seems that femtosecond frequency conversion through this mechanism is limited to a few tenths of a nanojoule, similar to energies in [17].
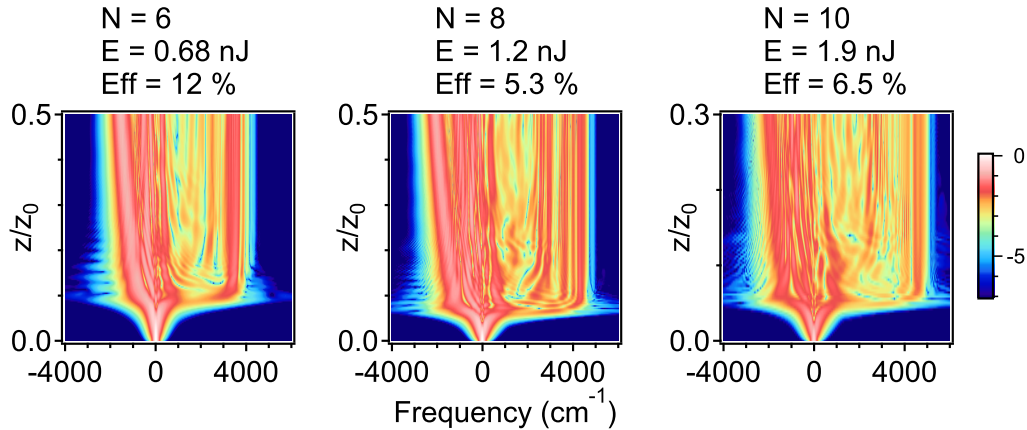
Figure 2.3: Femtosecond dispersive waves for increasing input energies.

If dispersive wave generation is to be used in a CARS microscopy source, its performance for picosecond pulses must be assessed. Since the soliton spectrum must broaden up to the dispersive resonance, large soliton N are required for the initially narrowband picosecond pulses. Figure 2.4 shows simulation results for a 1 ps input pulses. For a N=15 soliton, a dispersive wave is visible, but conversion efficiency is low at about 0.1%. Scaling up to N=25 and N=35, a continuum begins to form and the conversion efficiency is about 1-3%. For higher input energy, a

continuum forms and the dispersive wave is highly distorted. The dispersive wave energy does not exceed a few hundredth of a nanojoule.
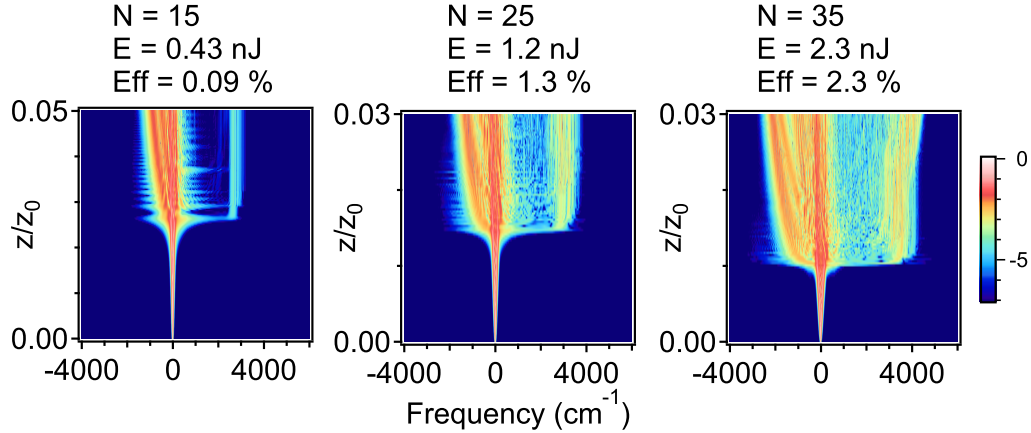
Figure 2.4: Picosecond dispersive waves for increasing input energies.

The regime over which dispersive wave generation in PCF produces clean blueshifted pulses with high efficiency thus seems constrained by supercontinuum generation. No more than a few tenths of a nanojoule can be obtained for femtosecond pulses, and for picosecond pulses only a few hundredths of a nanojoule are expected. Another frequency conversion mechanism is necessary to build a fiber-based CARS microscopy source.

2.3 Normal dispersion FWM theory and modeling

We now turn our attention to four-wave mixing. The normal dispersion regime is promising for frequency conversion as it is not affected by soliton compression and fission, which can lead to complex spectra and instabilities if not properly managed

As discussed in Chapter 1.3, the FWM phase-matched gain in optical fibers is dependent on the dispersion profile of the fiber. At normal dispersion, phase-

matching yields widely-spaced and narrow sidebands, as required for CARS. Their position can be controlled by tailoring the dispersion of a PCF, mainly its zero-dispersion wavelength (ZDW). For this experiment, a custom PCF was provided by our collaborators (fiber 050803B, Bath University, United Kingdom). The fiber is endlessly single-mode with a one missing hole design. It was chosen so the spontaneous FWM sidebands obtained around 1030 nm were observed at wavelengths suitable for CARS microscopy. Figure 2.5 shows a cross-section of the fiber as well a modeled dispersion curve matching the observed FWM wavelengths. From the micrograph, the PCF is estimated to have a pitch $\Lambda = 3.0$ μm and air hole diameter $d/\Lambda = 0.42$.
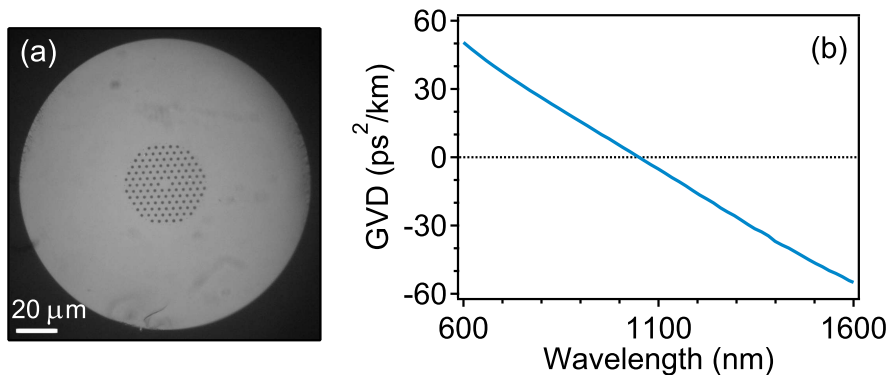
Figure 2.5: (a) Optical micrograph of the Bath 050803B PCF. (b) Modeled PCF dispersion curve (Courtesy of William J. Wadsworth at Bath University).

The FWM gain spectrum can be calculated using the dispersion coefficients of the PCF. The dispersion coefficients β_n around a pump wavelength of 1036 nm calculated from the dispersion curve in Figure 2.5 are given in Table 2.1.

Figure 2.6 shows the phase-matching diagram for Bath 050803B calculated using Eq. 1.18. The non-linear parameter is $\gamma = 9.6$ (W km)$^{-1}$ and the CW power of $P_0 = 3.6$ kW matches the pulse peak power in the experiments below. This shows that a pump laser tunable from 1030 nm to 1040 nm can be shifted

β_2 (fs^2/mm)	1.48
β_3 (fs^5/mm)	59.5
β_4 (fs^5/mm)	-69.5
β_5 (fs^5/mm)	136
β_6 (fs^5/mm)	-180

Table 2.1: Dispersion coefficients modeled at 1036 nm for Bath 050803B PCF.

by FWM in the PCF to wavelengths between 770 nm and 820 nm with narrow bandwidths.
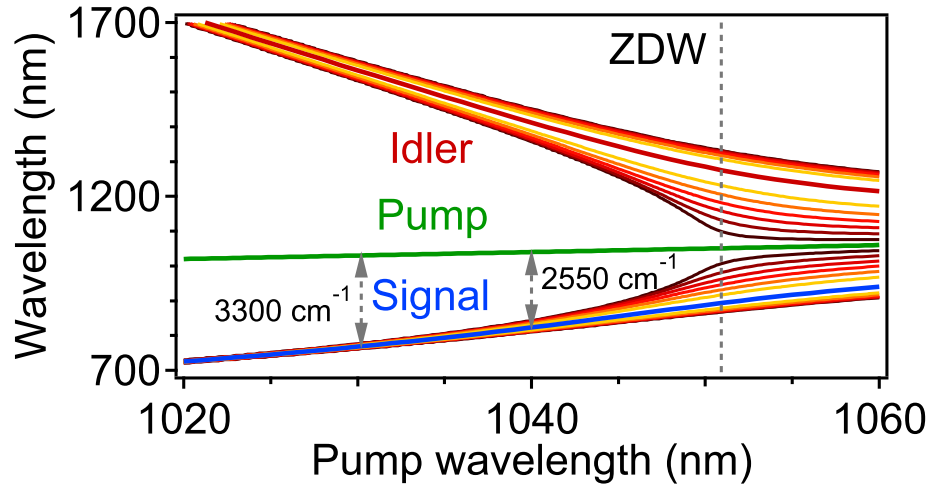
Figure 2.6: Phase-matched four-wave mixing gain for PCF Bath 050803B.

To understand the FWM process in the pulsed regime, we perform numerical simulations of the GNLSE Eq. 1.15. To account for the possibility of spontaneous FWM, the shot noise and Raman ASE are included. The input pulse is a gaussian centered at 1036 nm with 3.6 kW peak power and 7.5 ps FWHM duration. The spontaneous FWM case where only the pulsed pump is input is shown in Figure 2.7. After 56 cm, the the signal field near 800 nm reaches 3.1 nJ of pulse energy, typically required for a CARS source. Broad (>10 nm), randomly-fluctuating signal and idler bands grow spontaneously from the shot noise. The signal energy saturates below 6 nJ as supercontinuum generation takes over past the GVM length of ~50 cm. At this point, the pulses have walked off due to GVM, and non-phase-

matched processes such as SPM and Raman scattering dominate. The GVM thus places a clear limit on the FWM process.
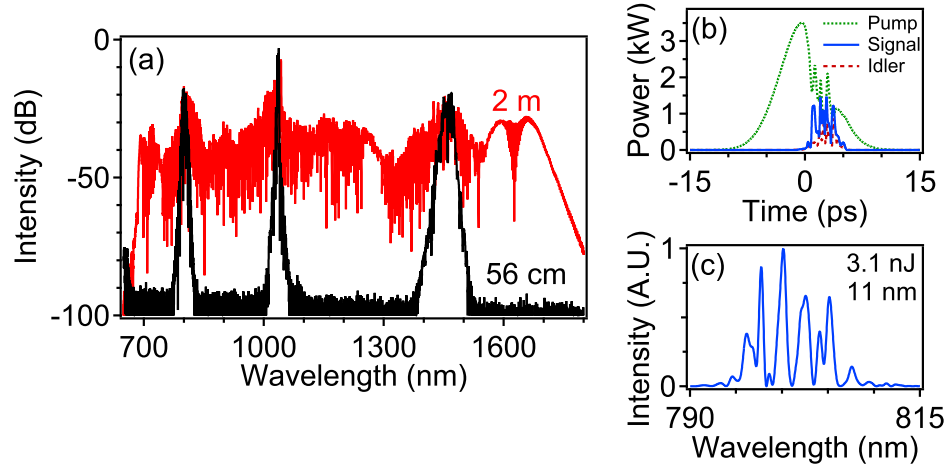
Figure 2.7: Simulated spontaneous FWM in PCF. (a) Full spectrum without idler seeding after propagating through 56 cm and 2 m. (b) Pulses and (c) signal spectrum after 56 cm propagation.

We propose that seeding the FWM process allows the fields to build up before GVM separates them. Seeding a parametric process is known to reduce fluctuations and narrow the output spectrum [20, 21], but to our knowledge there is no prior report of its use to counter GVM. 5 mW of CW light is injected at the idler frequency of 1470 nm to seed the FWM. The resulting pulses after 30 cm of propagation are shown in Figure 2.8(a). Clean signal and idler pulses are generated before GVM stops phase-matched FWM. The narrowband signal pulse carries more than 3 nJ of energy, corresponding to more than 10% of conversion efficiency. Further conversion is limited by coherent energy exchange between fields, which also generates broadband structured pulses.

Seeding the FWM is thus necessary to generate stable narrowband pulses for CARS. The next section presents a corresponding experimental design.
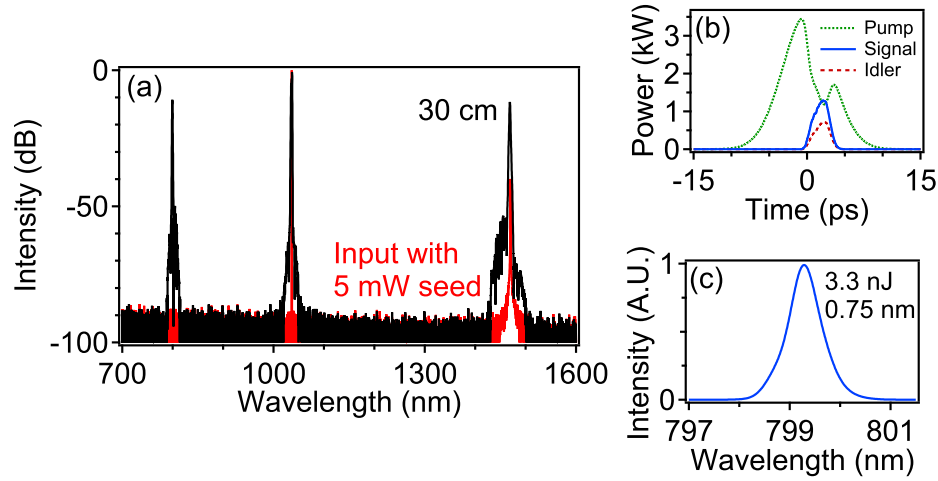
Figure 2.8: Simulated seeded FWM in PCF. (a) Full spectrum at input (red) and after propagating 30 cm (black). (b) Pulses and (c) signal spectrum after 30 cm.

2.4 High energy picosecond fiber laser

The simulations above indicate that picosecond pulses with kilowatt peak powers are necessary for efficient FWM. Amplifying few-picosecond pulses in fiber presents a special challenge. On one hand, dispersion lengths are on the order of 10s to 100s of meters, precluding the use of chirped-pulse amplification. On the other end, the kilowatt peak powers required here correspond to non-linear lengths on the order of 10 cm. It is necessary to mitigate non-linearity to avoid SPM spectral broadening that would lower the FWM gain and degrade CARS performance. Direct amplification thus requires specialty large-core fibers.

For the reasons outlined above, CARS microscopy currently uses high-power solid-state lasers based on diode-pumped Nd:YVO$_4$ technology [6]. Recently, our group demonstrated an all-fiber picosecond source based on direct amplification in few-mode LMA fiber [10]. This system can deliver up to 10 kW of peak power, but SPM broadening becomes significant after only 2 kW peak powers. To maximize

43

the FWM performance, further mitigation of non-linearity is required.

Divided-pulse amplification (DPA) was proposed to amplify picosecond pulses to high energies [22]. This method uses the large retardation in birefringent crystals to divide input pulses along the fast and slow polarization axes. By using a series of n crystals with length $L_0/2^{n-1}$ and alternating the optical axes by 45°, the input pulse is divided into 2^n copies with correspondingly lower peak power. These copies are amplified and then recombined using a matching divider built in reverse order. The DPA system used in this experiment is shown in Figure 2.9(a) and was developed in collaboration with Lingjie Kong. Figure 2.9(b) demonstrates the DPA concept in this system.
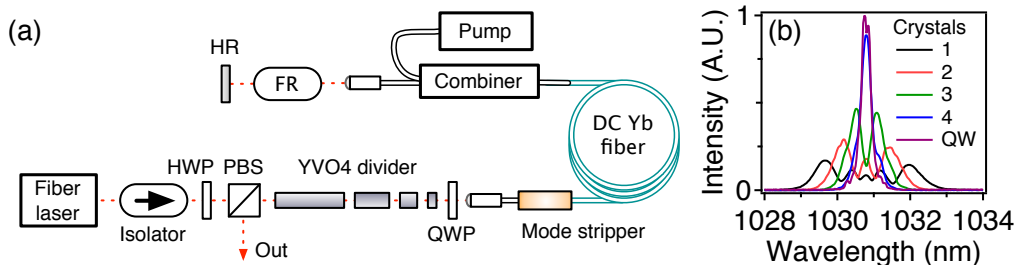
Figure 2.9: High energy picosecond fiber laser based on DPA. (a) Setup: HWP/QWP: half/quarter-wave plate, PBS: polarizing beamsplitter, FR: Faraday rotator and HR: dielectric mirror. (b) Evolution of output spectra as dividing elements are added at an output pulse energy of ∼23 nJ.

The seed oscillator is a SESAM-modelocked Yb-doped fiber laser tunable from 1030 nm to 1040 nm and delivering up to 15 mW average power at 53.5 MHz repetition rate. The laser was provided by TOPTICA Photonics (Munich, Germany) as a modified version of their PicoFYb product. An high-power isolator protects the oscillator from the DPA return signal. The divider is composed of four undoped YVO$_4$ crystals, yielding a delay of ∼1 ps/mm. The lengths are 57.6 mm, 28.8 mm, 14.4 mm and 7.2 mm. A quarter-wave plate converts the polarizations to circular to reduce the effective non-linearity in the fiber [23]. The amplifier

is composed of 2 m of double-clad Yb-doped fiber with a 10 μm core diameter, NA of 0.08 and cladding diameter of 125 μm. The input side has about 20 cm of matching passive fiber and the output side has about 55 cm. A cladding mode stripper couples out the unabsorbed pump using index-matching gel applied to the bare gain/passive fiber splice. A fiber-coupled multimode diode pump is spliced into a fused pump/signal combiner. The pump delivers more than 20 W of power at 976 nm in a fiber with 100 μm core diameter and NA of 0.22. The amplifier is set up in a double-pass configuration with a Faraday rotator to rotate the polarizations by 90°. This cancels the linear birefringence in the fibers and reverses the divider effects to recombine the pulses in an automatically matched configuration. A polarizing beamsplitter then ejects the amplified and recombined signal.

The output pulses from the DPA system are characterized in Figure 2.10. The spectral bandwidth is constant at 0.3 nm for output pulse energies of more than 70 nJ. The autocorrelation is sech^2-like with a duration of about 7.2 ps. Beyond 50 nJ, a wide pedestal starts to develop and the central pulse broadens. This may be due to cross-phase modulation between the edges of neighboring pulses inducing non-linear birefringence and distorting pulse recombination. Longer divider crystals could alleviate the issue. Overall, more than 5 kW of peak power can be delivered before pulse distortion occurs.
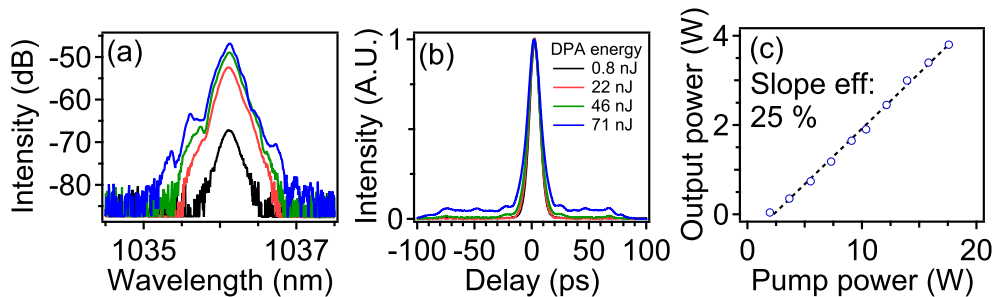
Figure 2.10: Output of picosecond DPA system: (a) pulse spectra, (b) autocorrelation and (c) output power trend.

2.5 Four-wave mixing frequency conversion experiments

The complete experimental setup is shown in Figure 2.11. The DPA output around 1030 nm is combined with a fiber-coupled single frequency diode laser tunable from 1400 nm to 1490 nm and providing up to 30 mW (TOPTICA DLpro). The polarization-matched beams are coupled into the Bath 050803B PCF. Typical coupling efficiencies for the pump and idler seed are respectively 70-80% and 15-20%. A dichroic filter separates the output signal from the residual pump and idler. A bandpass filter block the anti-Stokes light generated by non-resonant mixing of the signal and pump in the PCF [24]. A fraction of the 1 μm pulses is picked-off before the PCF, sent to a delay line and combined with the polarization-matched signal at the microscope.
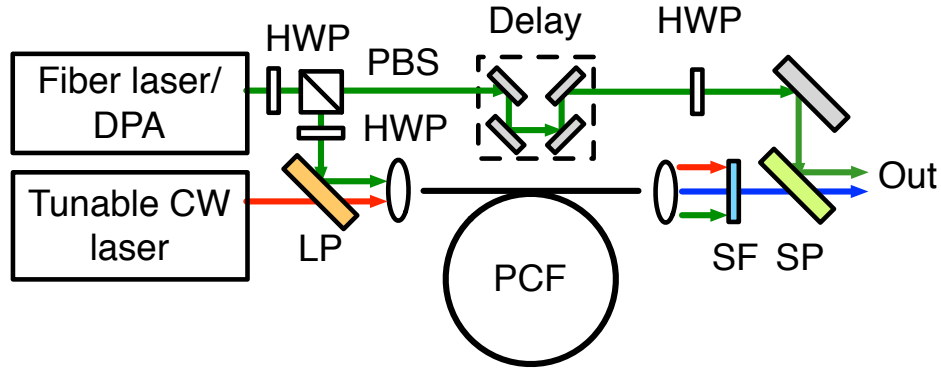
Figure 2.11: Experimental setup. HWP: half-wave plate, PBS: polarizing beam-splitter, LP: long-pass dichroic mirror, SF: filters, SP: short-pass dichroic mirror.

Experimental results with 30 cm of PCF are shown in Figure 2.12. 30 nJ of pump pulse energy at 1038 nm is coupled into the PCF. The idler is seeded with 5.1 mW at 1471 nm. The generated signal pulses have 3.1 nJ of energy and a duration of 1.8 ps, while 5.8 nJ pump pulses are picked-off to be recombined with the signal. A small satellite pulse is visible 20 ps from the main signal pulse. This pulse contains less than 1% of the energy and should not affect CARS performance. The

frequency difference of 2850 cm^{-1} corresponds to the CH$_2$ stretch. The bandwidth of the signal and pump are respectively 16 cm^{-1} and 3 cm^{-1}, suitable for CARS. The overall performance is similar to solid-state systems [6]. The peak power was tested by launching 2.2 nJ of signal pulses in 1.9 m of fiber with 4.4 μm core diameter and NA of 0.13. The resulting SPM broadening matches well with simulations using parameters within the uncertainty in fiber specifications, confirming more than 1.5 kW of peak power is generated around 800 nm.
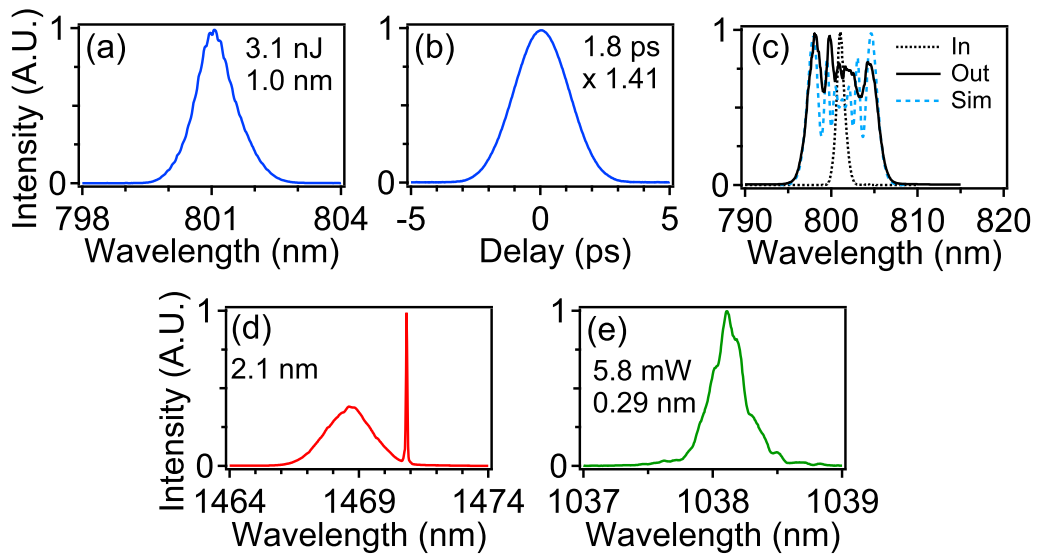
Figure 2.12: Experimental FWM results after 30 cm of PCF with a 1038 nm pump: signal (a) spectrum and (b) autocorrelation and (c) peak power test in single-mode fiber. (d) idler and seed and (e) picked-off pump spectrum.

With the tuning range of the diode, we achieved similar performance for frequency shifts of 2650 cm^{-1} and 2950 cm^{-1}. Coarse tuning can be accomplished by changing the pump wavelength, while fine tuning over 1 to 2 nanometers can be done by tuning the seed. No re-alignment is required. By use of a similar fiber amplifier centered at 1031 nm and an amplified diode laser, a signal wavelength of 774 nm can be generated with similar performance, corresponding to a Raman shift of 3200 cm^{-1}. The input pump pulse energy is 39 nJ and the seed has 13 mW

of power at 1546 nm. The results are shown in Figure 2.13.
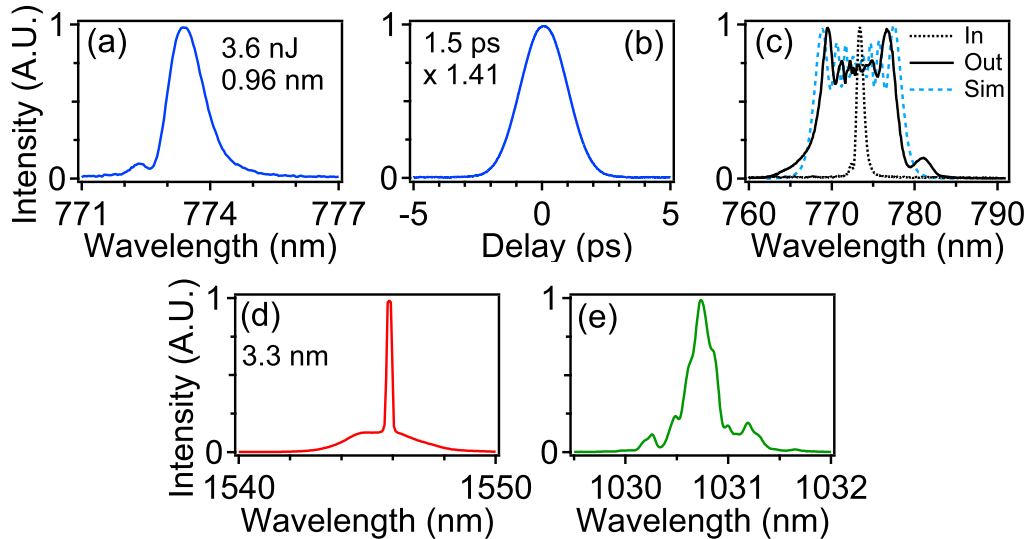
Figure 2.13: Experimental FWM results after 30 cm of PCF with a 1031 nm pump: signal (a) spectrum, (b) autocorrelation and (c) peak power test in single-mode fiber. (d) Idler and seed and (e) pump spectrum.

Higher powers or longer fibers yield higher signal energies at the expense of structured spectra. Depending on the exact system parameters, PCF lengths between 25 cm to 40 cm can be used. For longer fibers or very high energies, the conversion efficiency tends to saturate, indicating that energy may be flowing back from the signal to the pump. Complex and broad signal spectra are generated, probably due to a cascaded non-linear process. This is illustrated in Figure 2.14.

2.6   CARS microscopy of animal tissues and cells

The two-color FWM fiber laser was transported to a microscopy laboratory for CARS imaging. Note that 35 cm of PCF were used to roughly reproduce the pulse energies and bandwidths presented above, due to variations in the exact setup conditions. The FWM signal and picked-off pump are coupled into a laser-scanning
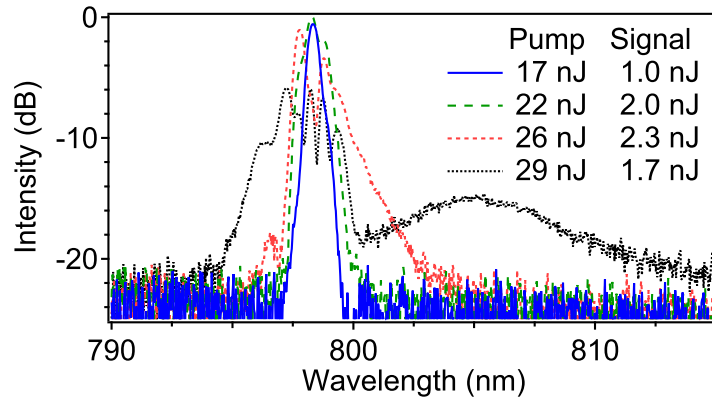
Figure 2.14: Experimental signal after 50 cm of PCF for increasing pump energy. Input pump is provided by a filtered soliton fiber laser and DPA system with pulse duration of 8.6 ps.

microscope (customized Zeiss LSM 510) and focused using a 40X water-immersion objective with a numerical aperture of 1.1. The total power delivered to the samples is about 60 mW, close to the damage threshold. We detect the forward-generated CARS signal with a non-descanned photomultiplier tube behind bandpass filters that isolate the CARS signal. All images are 512x512 pixels and are acquired at 4 s/frame with no averaging. Faster imaging at sub-Hz frame rates are possible at the expense of additional noise. The imaging experiments are done in collaboration with Gary Holtom and Dan Fu at Harvard University.

CARS images of the lipid CH_2 vibration at 2850 cm^{-1} from a nude mouse ear are presented in Figure 2.15. Surface images show the structure of the stratum corneum. Deeper images show sebaceous glands around hair shafts. Sub-cellular lipid droplets are clearly visible as small bright spots, while large darker spots highlight the cell nuclei. Imaging at 2950 cm^{-1} was also performed but did not reveal qualitatively different contrast.

Figure 2.16 shows images at 2850 cm^{-1} from a mouse brain. Myelin sheath wrapped around axons are visible in the transverse and longitudinal directions.
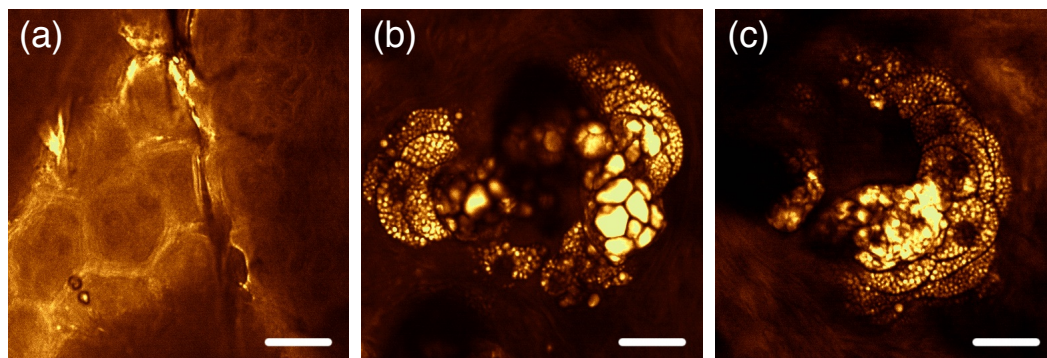
Figure 2.15: Forward-CARS images of a mouse ear at 2850 cm^{-1}: (a) stratum corneum and (b)-(c) sebaceous glands 33 μm and 40 μm deep respectively. Scale bars are 20 μm.
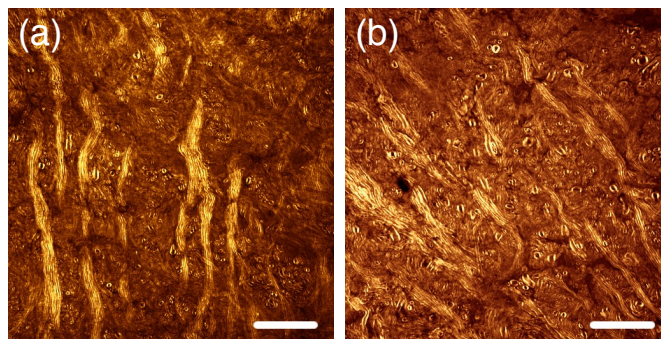
Figure 2.16: Forward-CARS images at 2850 cm^{-1} of mouse brain sections. Scale bars are 50 μm.

Finally, Figure 2.17 shows cultured rat fibroblast cells at 2850 cm^{-1} and 2950 cm^{-1}. As with sebaceous glands, sub-cellular lipid droplets and nuclei are visible. When imaging at 2950 cm^{-1}, the lipid signal drops as expected, and dark contrast features appear. This is the well-know negative contrast on the blue side of a CARS line, caused by interference between the resonant CARS signal and the non-resonant background [4].

To compare imaging performance with existing solid-state sources, image quality is quantified. The typical lipid droplet signal relative to noise is 40 for cell images and 80-120 for sebaceous glands. At a shift of 2950 cm^{-1}, this dropped to 25 for cells and 40 for sebaceous glands as expected. Overall, this confirms that
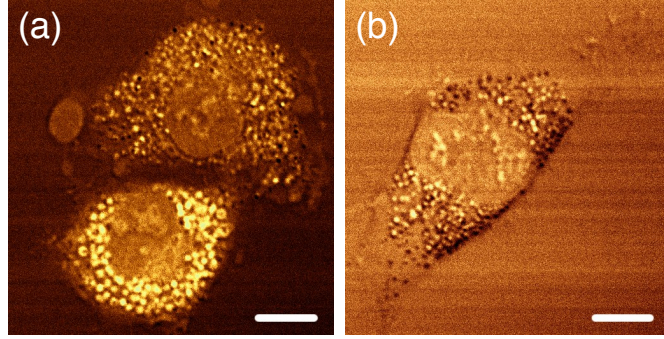
Figure 2.17: Forward-CARS images of rat fibroblasts at (a) 2850 cm^{-1} and (b) 2950 cm^{-1}.

the two-color fiber laser presented here can deliver performance and image quality matching solid-state sources in similar conditions.

2.7   Amplitude noise

Characterization of the noise of a CARS laser source is important to understand the determinants of image quality. Slow signal oscillations are visible on Figure 2.17(b) as darker horizontal line. This may be due to slow amplitude fluctuations in input laser power made visible by the lower signal level in isolated cell imaging and by using 2950 cm^{-1} contrast. This may be due to mechanical fluctuations in the free-space fiber couplings, especially at the high power PCF input which is subject to thermal effects. This could be improved using fused-fiber couplers and specialty PCF splicing, as well as mounting remaining free-space coupled fiber into stable and thermally conductive ferrules.

For faster kHz and MHz level noise, the FWM signal is sensitive to noise in the input fields. Indeed, fluctuations are transferred from the pump and idler seed

onto the signal following Eq. 2.2.

$$I_s \propto I_p^2 I_i \qquad \frac{\Delta I_s}{I_s} = 2\frac{\Delta I_p}{I_p} + \frac{\Delta I_i}{I_i} \qquad (2.2)$$

This is well illustrated by comparing the FWM signal noise for different CW seeds. Figure 2.18 compares the radio-frequency (RF) noise around the fundamental repetition rate for a CW Er-doper fiber laser, a semiconductor diode laser amplified with an Er-doped fiber amplifier (EDFA) and a single-frequency diode laser. The fiber laser seed has a bandwidth of about 0.12 nm and a cavity length of a few meters, yielding multi-frequency operation. This results in a coherence time of about 10-20 ps in the fluctuations of the CW field, which should transfer to the FWM signal. Indeed, a white noise background is visible only 50 dB from the fundamental harmonic. In contrast, the semi-conductor lasers and single-frequency diodes have much larger mode spacing and narrower bandwidths (below the resolution of the spectrum analyzer used), and the signal noise floor is 70 dB down or better. Low noise sidebands are visible around and below 70 dB for the single-frequency seeded system. These are found to be coupled in from the pump fiber oscillator.
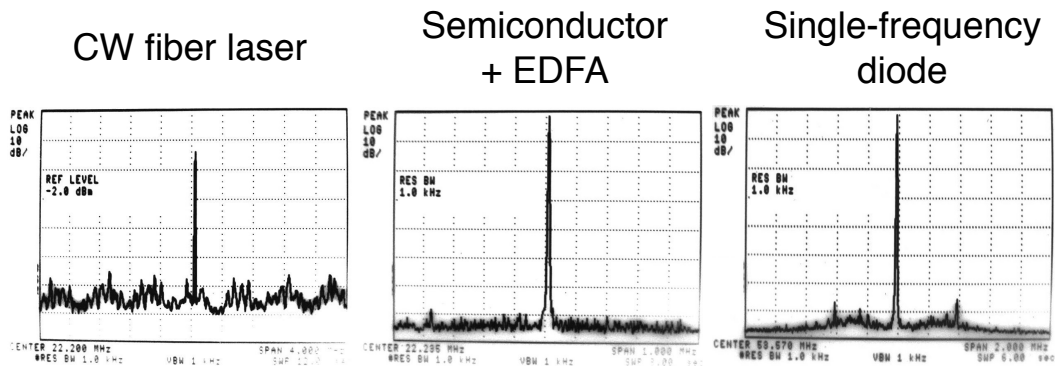
Figure 2.18: RF noise for the FWM signal seeded by different seed lasers. Scale is 10 dB/div and resolution bandwidth is 1 kHz.

Certain advanced imaging modalities are particularly sensitive to fast ampli-

tude noise. This is the case for stimulated Raman scattering (SRS) imaging [5]. SRS imaging uses lock-in detection to extract the Raman gain or loss instead of the generated anti-Stokes. The SRS signal is free of the non-resonant background, enhancing chemical contrast and allowing for straight Raman spectrum extraction. It is also linearly dependent on molecular concentration, facilitating quantitative imaging. However, typical SRS signals are a difference on the order of -40 dB on the main signal. Thus, to obtain a signal-to-noise ratio (SNR) of about 100, the optical intensity noise around the lock-in modulation frequency should be no higher than about -60 dB (private communication with Christian Freudiger and Gary Holtom at Harvard University). CARS is much less sensitive as it measures an absolute photon count.

We attempted to perform stimulated Raman scattering (SRS) imaging with the FWM fiber source. Preliminary experiments with dodecane showed excessive fluctuations in the SRS signal, precluding imaging. To better understand the source of noise, the relative intensity noise (RIN) of the different laser stages was measured [25]. This is done in collaboration with Christian Freudiger at Harvard University. The signal from a fast photodetector is low-pass filtered to eliminate the pulse train frequencies. A bias-T then separates the DC carrier from the 0-20 MHz radio-frequency signal which is detected with an electrical spectrum analyzer. The raw data is normalized to the DC carriers ranging from 0.55 V to 0.8 V coupled into 50 Ω and to the spectrum analyzer resolution bandwidth of 3.2 kHz. The results are compared with the standard solid-state laser and OPO system in Figure 2.19.

The fiber oscillator has a noise level similar to the solid-state OPO signal, both close to the shot noise limit. The DPA adds about 10 dB of noise, as expected given
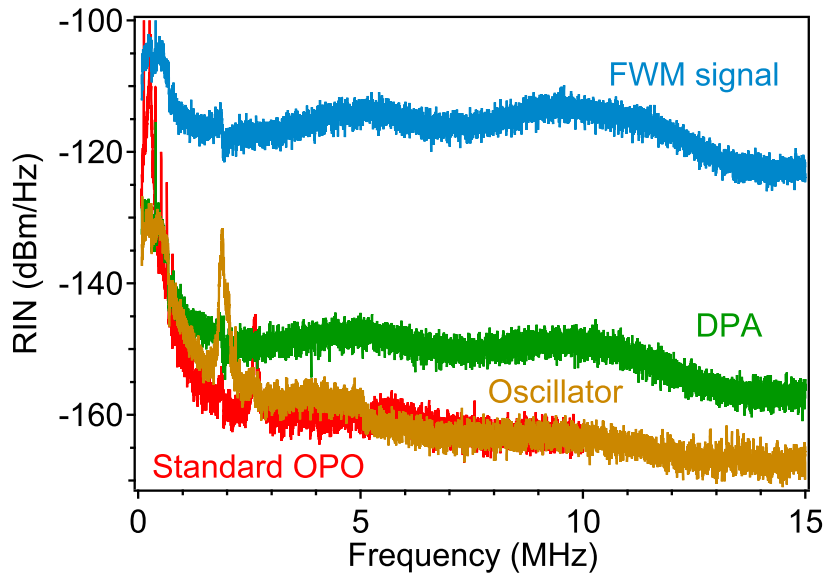
Figure 2.19: Relative intensity noise of the FWM fiber source compared to standard OPO system.

the high gain and strong ASE in fiber amplifiers. The largest noise contribution is the FWM, adding 35 dB. This is expected as the relative noise on the pump and idler seed are compounded on the FWM signal according to Eq. 2.2. Note that the RIN of the diode laser seed could not be measured above the detector noise floor given its lower power output. The FWM signal has a RIN around -110 dB at the lock-in frequency of 10 MHz. This corresponds to an optical intensity noise of about -55 dB, noisier than required for SRS.

We can conclude that fiber sources will have to be designed for low-noise performance for SRS microscopy. Optimization of the detection scheme will also be desirable, for instance by modulating the FWM signal and detecting the quieter fiber laser pulse train. A quieter frequency conversion scheme could significantly reduce noise. Chapter 8.1 will present preliminary work on a fiber-OPO based on FWM in PCF.

2.8 Conclusion

To summarize, we have demonstrated a fiber-based source for CARS microscopy based on picosecond FWM in PCF. Seeding of the FWM process overcomes the limitations of noise and group-velocity mismatch. More than 160 mW of 2 ps pulses can be generated at suitable frequency shifts covering more than 500 cm^{-1}. The optical intensity noise of -55 dB on the 800 nm signal is too high for SRS imaging. Low-noise designs and new detection schemes could make SRS imaging possible. The system could also be further integrated using specialty splices and fiber couplers. This is a significant step toward a turn-key fiber-based source that will allow CARS microscopy to extend into biological and clinical applications.

Contemporary with the work presented in this chapter, an unseeded FWM CARS source was reported [26]. It used longer pulses and CARS imaging of biological samples was not reported. This confirms the importance of seeding to overcome both spontaneous noise and group-velocity mismatch.

Bibliography

[1] S. Lefrancois, D. Fu, G. R. Holtom, L. Kong, W. J. Wadsworth, P. Schneider, R. Herda, A. Zach, X. S. Xie, and F. W. Wise, Opt. Lett. **37**, 1652 (2012).

[2] S. Lefrancois, D. Fu, G. Holtom, L. Kong, W. Wadsworth, P. Schneider, R. Herda, A. Zach, X. S. Xie, and F. W. Wise, in *Multiphoton Microscopy in the Biomedical Sciences XII*, edited by A. Periasamy, K. Konig, and P. T. C. So (SPIE, Bellingham, WA, 2012), No. 1, p. 822620.

[3] S. Lefrancois, L. Kong, D. Ouzounov, F. Wise, and C. Yang, in *Multiphoton Microscopy in the Biomedical Sciences XI*, edited by A. Periasamy, K. Konig, and P. T. C. So (SPIE, Bellingham, WA, 2011), No. 1, p. 79030W.

[4] C. L. Evans and X. S. Xie, Annu. Rev. Anal. Chem. **1**, 883 (2008).

[5] C. W. Freudiger, W. Min, B. G. Saar, S. Lu, G. R. Holtom, C. He, J. C. Tsai, J. X. Kang, and X. S. Xie, Science **322**, 1857 (2008).

[6] F. Ganikhanov, S. Carrasco, X. S. Xie, M. Katz, W. Seitz, and D. Kopf, Opt. Lett. **31**, 1292 (2006).

[7] E. R. Andresen, H. N. Paulsen, V. Birkedal, J. Thogersen, and S. R. Keiding, J. Opt. Soc. Am. B **22**, 1934 (2005).

[8] A. F. Pegoraro, A. Ridsdale, D. J. Moffatt, J. P. Pezacki, B. K. Thomas, L. Fu, L. Dong, M. E. Fermann, and A. Stolow, Opt. Express **17**, 20700 (2009).

[9] Y.-H. Zhai, C. Goulart, J. E. Sharping, H. Wei, S. Chen, W. Tong, M. N. Slipchenko, D. Zhang, and J.-X. Cheng, Appl. Phys. Lett. **98**, 191106 (2011).

[10] K. Kieu, B. G. Saar, G. R. Holtom, X. S. Xie, and F. W. Wise, Opt. Lett. **34**, 2051 (2009).

[11] K. Wang, C. W. Freudiger, J. H. Lee, B. G. Saar, X. S. Xie, and C. Xu, Opt. Express **18**, 24019 (2010).

[12] G. Krauss, T. Hanke, A. Sell, D. Träutlein, A. Leitenstorfer, R. Selm, M. Winterhalder, and A. Zumbusch, Opt. Lett. **34**, 2847 (2009).

[13] K. Kieu and N. Peyghambarian, in *Multiphoton Microscopy in the Biomedical Sciences XI*, edited by A. Periasamy, K. Konig, and P. T. C. So (SPIE, Bellingham, WA, 2011), No. 1, pp. 790310–790310–7.

[14] S. Bégin, B. Burgoyne, V. Mercier, A. Villeneuve, R. Vallée, and D. Côté, Biomed. Opt. Express **2**, 1296 (2011).

[15] N. Akhmediev and M. Karlsson, Phys. Rev. A **51**, 2602 (1995).

[16] I. Cristiani, R. Tediosi, L. Tartara, and V. Degiorgio, Opt. Express **12**, 124 (2004).

[17] H. Tu and S. A. Boppart, Opt. Express **17**, 9858 (2009).

[18] D. Nodop, C. Jauregui, D. Schimpf, J. Limpert, and A. Tünnermann, Opt. Lett. **34**, 3499 (2009).

[19] L. Lavoute, J. C. Knight, P. Dupriez, and W. J. Wadsworth, Opt. Express **18**, 16193 (2010).

[20] P. J. Mosley, S. A. Bateman, L. Lavoute, and W. J. Wadsworth, Opt. Express **19**, 25337 (2011).

[21] M. D. Cocuzzi, K. L. Schepler, and P. E. Powers, IEEE J. Sel. Top. Quant. **15**, 372 (2009).

[22] S. Zhou, F. W. Wise, and D. G. Ouzounov, Opt. Lett. **32**, 871 (2007).

[23] L. J. Kong, L. M. Zhao, S. Lefrancois, D. G. Ouzounov, C. X. Yang, and F. W. Wise, Opt. Lett. **37**, 253 (2012).

[24] M. Balu, G. Liu, Z. Chen, B. J. Tromberg, and E. O. Potma, Opt. Express **18**, 2380 (2010).

[25] R. P. Scott, C. Langrock, and B. H. Kolner, IEEE J. Sel. Top. Quant. **7**, 641 (2001).

[26] M. Baumgartl, M. Chemnitz, C. Jauregui, T. Meyer, B. Dietzek, J. Popp, J. Limpert, and A. Tünnermann, Opt. Express **20**, 4484 (2012).

CHAPTER 3

PROPERTIES OF STIMULATED RAMAN SCATTERING STOKES PULSES IN CHIRPED-PULSE AMPLIFICATION[1]

In this chapter, we numerically study the generation of broadband Raman Stokes pulses generated by highly chirped pump pulses. We find that the compressibility of the Stokes pulse requires a chirped pump pulse duration not too large relative to the vibrational dephasing time of the medium. Remarkably, pulses remain compressible for dephasing times much smaller than the pulse duration, down to 1/30th of the pump duration. This indicates that operation of chirped pulse amplifiers beyond the SRS threshold is possible in a wide range of materials that can be used as Raman shifters, but that pulse coherence may be degraded in the case of glass systems.

3.1   Introduction

Chirped-pulse amplification (CPA) is currently the method of choice to maximize peak power from ultrafast laser systems. Using a highly-chirped pulse limits the nonlinear phase accumulation that degrades pulse quality, especially in fiber system with their tight light confinement and long interaction lengths. Pulse energies on the order of μJs at 100s of femtoseconds have been reached in fiber CPA systems [2, 3]. CPA was originally designed to prevent pulse distortion by self-phase modulation (SPM) by keeping the non-linear phase accumulation $\Phi_{NL} < 1$. Recent development in non-linear CPA allow $\Phi_{NL} \sim 10\pi$ to be tolerated in fiber systems, either through spectral shaping [4, 5, 6] or by third-order dispersion compensa-

tion of SPM [7, 8]. Going to higher energies and peak powers is then limited by stimulated Raman scattering (SRS), which depletes and distorts the pump pulse.

In fused silica fiber, the Raman response produces a Stokes shift of 440 cm^{-1} with a dephasing time of about 30 fs [9]. Initial studies suggest that the Stokes pulse may be recompressible when pulse walk-off is negligible [10]. Detailed numerical studies of pulse propagation under both stimulated and spontaneous Raman scattering have been performed [11], but the direct transfer of phase from a highly chirped pump remains to be investigated. Compressibility of the Raman Stokes pulses from a highly-chirped pump has been demonstrated experimentally in a barium nitrate crystal, with a Stokes shift of 1047 cm^{-1} and a dephasing time of 25 ps [12, 13]. Raman pulse shifting and compression was also demonstrated in methane gas [14]. Recent experiments suggest the Stokes pulse generated in silica fibers might also be exploited to overcome the Raman limit in CPA systems and extend their wavelength range [15]. However, we can expect that the fast dephasing time in glasses will impact how the phase across a long chirped pump pulse will map unto the Stokes field. A detailed investigation of the effects of Raman scattering on highly chirped pulses is thus necessary.

Here we numerically study the generation of Raman Stokes pulses in CPA systems. The spontaneous generation of Stokes pulses by highly-chirped pump pulses is modeled as a function of the vibrational dephasing time. The compressibility of the Stokes pulses is investigated, as well as the compressed pulse quality. Finally, the statistics of the stochastically generated pulses are characterized.

3.2 Numerical Model

The full GLNSE Eq. 1.15 is used to model SRS in chirped-pulse amplifiers. In the case of highly chirped pulses, the different frequency components of the pulse are temporally separated, preventing the blue and red parts of the spectrum to beat and interact through SRS. It is thus critical to include spontaneous Raman scattering to model the initial growth of the Stokes pulse.

The dominant dispersion coefficient used is $\beta_2 = 23$ ps^2/km. The third-order dispersion is $\beta_3 = 0.028$ ps^3/km, although its exact magnitude has little effect compared to stochastic fluctuations. The SPM coefficient is $\gamma = 0.0047$ (W m)$^{-1}$. This corresponds to a fiber with an effective area of 30 μm^2, although the results can be directly scaled to any core size. The Raman fraction f$_R$ is 0.18 and we use a room temperature of 300 K. The RK4IP method avoids Raman amplification of numerical noise due to longitudinal steps size and discrete Fourier transforms. Shot noise was not found to significantly affect the generated Stokes pulse.

3.3 Stokes Pulse Generation

We simulate conditions similar to a chirped-pulse amplifier system. A 3 nJ, 100 fs gaussian pulse is chirped to 120 ps using a linear second-order stretcher, then amplified to 1 μJ using a 50-cm long Yb-doped fiber. Gain narrowing reduces the bandwidth from 16 nm to 13 nm and the chirped pulse duration to 101 ps. The pulse then propagates through a few meters of passive single-mode fiber where it is subject to stimulated and spontaneous Raman scattering. This propagation can represent any fiber pigtail after amplifier stages or the long gain fibers used

in cladding-pumped systems. We show representative results each seeded by an instance of the stochastic Raman ASE.
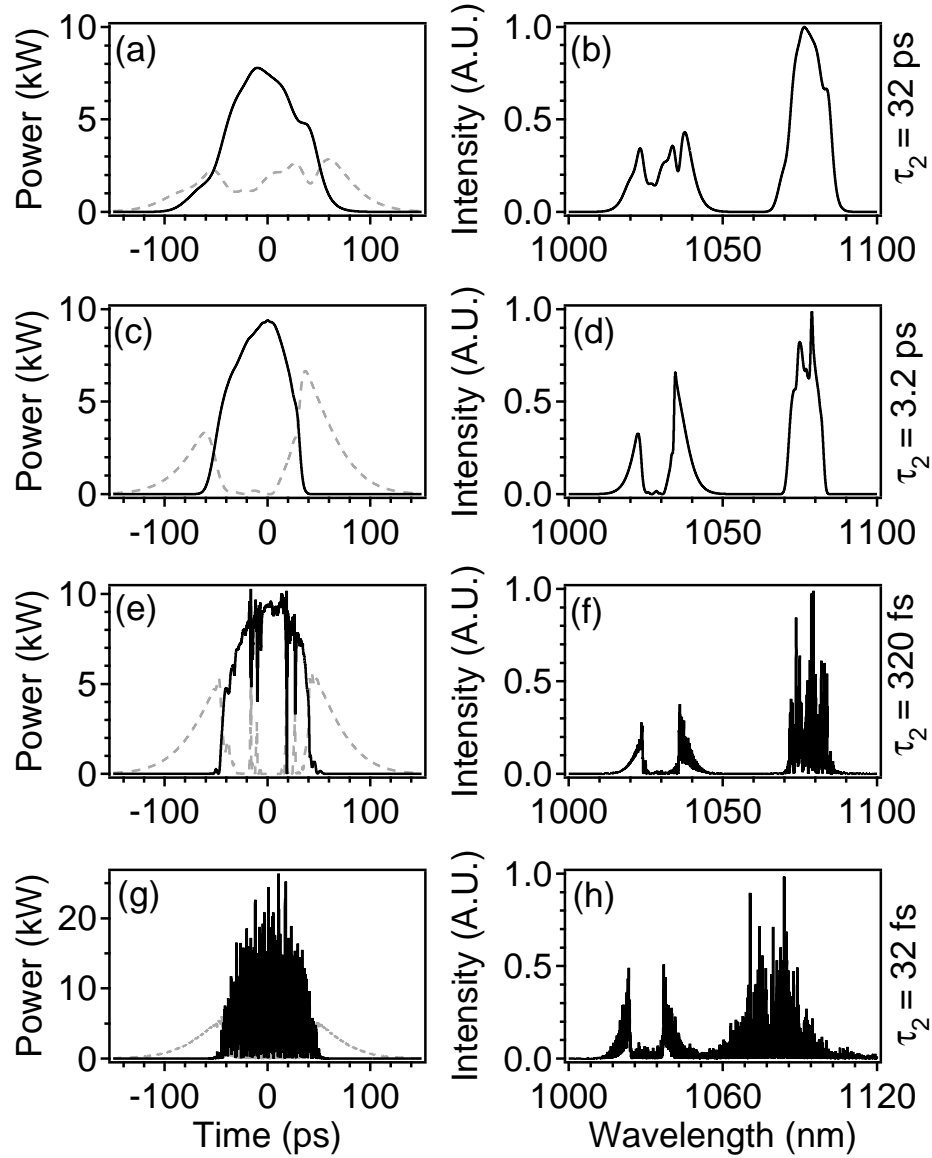
Figure 3.1: Left: Stokes pulses (solid) and depleted pump pulses (dashed) for varying dephasing time τ_2. Right: corresponding spectra.

To address the role of dephasing time in the transfer of phase from the pump to the Stokes pulse, we consider dephasing times τ_2 ranging from 32 ps down to 32 fs, the fastest corresponding to SRS in silica fibers. At $\tau_2 = 32$ fs, the

experimentally measured Raman gain is used [16]. For all other dephasing times, the Raman gain is renormalized to obtain significant Stokes generation over a few meters of fiber. The renormalization factors used to divide Eq. 1.11 are 175, 40 and 8 respectively for τ_2 32 ps, 3.2 ps and 320 fs. In all cases, propagation is stopped before a significant second-order Stokes pulse starts distorting the first order Stokes pulse. The resulting pulses and spectra are plotted in Figure 3.1. The conversion efficiencies from pump to Stokes for $\tau_2 = 32$ ps, 3.2 ps, 320 fs and 32 fs are respectively: 62% after 1.25 m, 58% after 1.25 m, 60% after 2.10 m, and 59% after 2.25 m. If shot noise and Raman ASE are removed, no Stokes pulse is generated, ruling out the possibility that the blue and red end of the spectrum could interact through SRS. As mentioned earlier, the large chirp temporally separates the frequency components and prevents intra-pulse Raman scattering.

For a dephasing time on the order of the chirped pump duration, a smooth Stokes pulse is generated. As the dephasing becomes faster, random structure starts deforming the pulse. For $\tau_2 < 1$ ps, the Stokes spectrum is highly and randomly structured. For the dephasing time of fused silica, the Stokes pulses is cut up into bursts of duration ∼100 fs, corresponding to the coherence time of spontaneous Raman scattering. Thus, for dephasing times longer than ∼ 1/100th of the pump duration, the delayed Raman convolution can smooth out the Raman ASE seed, but for faster responses it cannot prevent the Stokes from growing into independent bursts. In the next section, we will show that this correlates with a loss of internal coherence that prevents compressibility.

3.4 Coherence and Compressibility of Stokes pulses

An important test of the quality and coherence of the generated Stokes pulse is whether it can be recompressed close to its transform limit. Indeed, pulses from CPA systems must compress back to the high peak powers required by most applications. As a test, we propagate the Stokes field generated from different dephasing times through negative group-velocity dispersion (GVD), as shown in Figure 3.2. For τ_2 of 32 ps and 3.2 ps, the pulse clearly compresses to sub-ps duration, indicating coherent phase transfer between the chirped pump and the generated Stokes. Some internal structure is visible for a 3.2 ps dephasing time, suggesting the shorter dephasing time may distort the temporal phase. This effect is made more obvious for a 320 fs dephasing time. Although a tendency for the pulse to converge can be seen, the field is broken up into several sub-ps features that only converge down to ~ 20 ps. For the 32 fs dephasing time of fused silica, the ~ 100 fs bursts simply diverge due to dispersion, showing almost complete loss of coherence in the pulse.

The optimally compressed Stokes pulses are shown in Figure 3.3. Compression quality significantly improves with slower dephasing. For a τ_2 of 32 ps, the pulse compresses down to 300 fs, compared to a transform limit of 175 fs. A low-level pedestal can be seen, corresponding to residual non-linear chirp. Nevertheless, 65% of the energy is located in the main pulse. This pedestal is also observed in the compressed pump pulse before Raman shifting. It is due to self-phase modulation of a highly chirped pulse [17]. This indicates remarkably precise phase transfer between the pump and spontaneously generated Stokes fields. A faster dephasing of 3.2 fs yields a compressed duration of 310 fs compared to a transform limit of 280 fs. However, additional secondary structure is visible in amplitude and can be
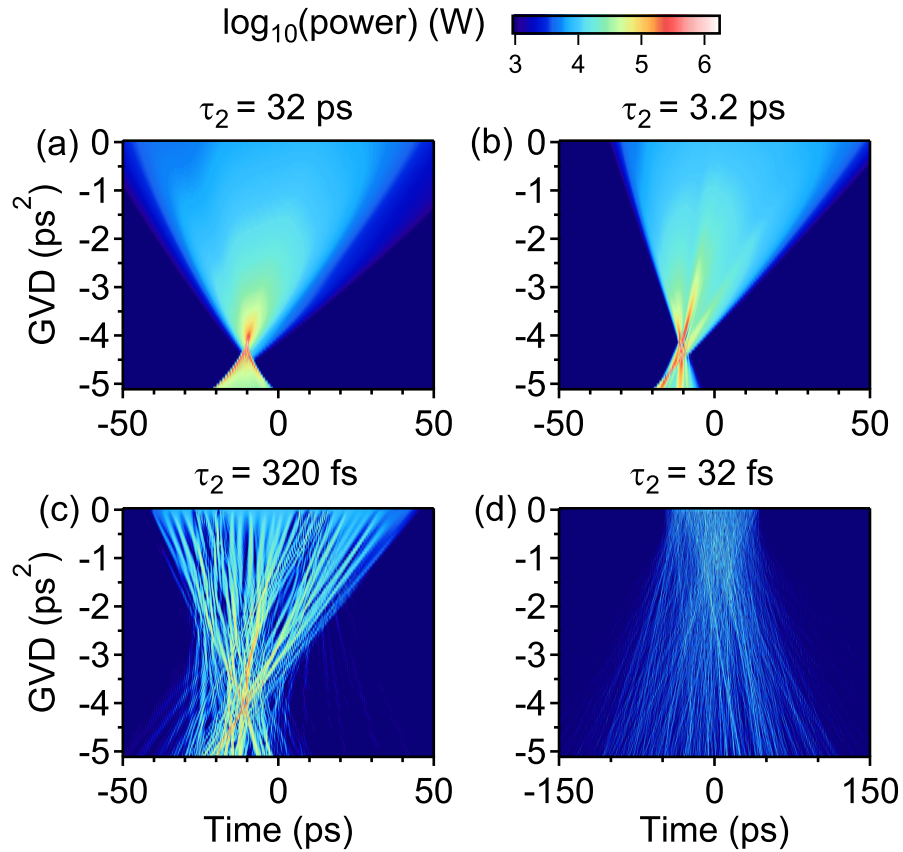
Figure 3.2: Propagation of Stokes pulses through GVD compressor.

seen to carry separate phase, indicating transient effects and degraded coherence. The main pulse contains about 45% of the energy. Stokes pulses generated with sub-ps dephasing times cannot compress below 10s of ps. The compressed pulse is randomly broken up into bursts whose durations are on the order of the coherence time. This confirms that phase transfer from pump to Stokes is limited by the dephasing time, and that a Raman response not too fast compared to the pump duration is necessary to generate coherent chirped Stokes pulses.
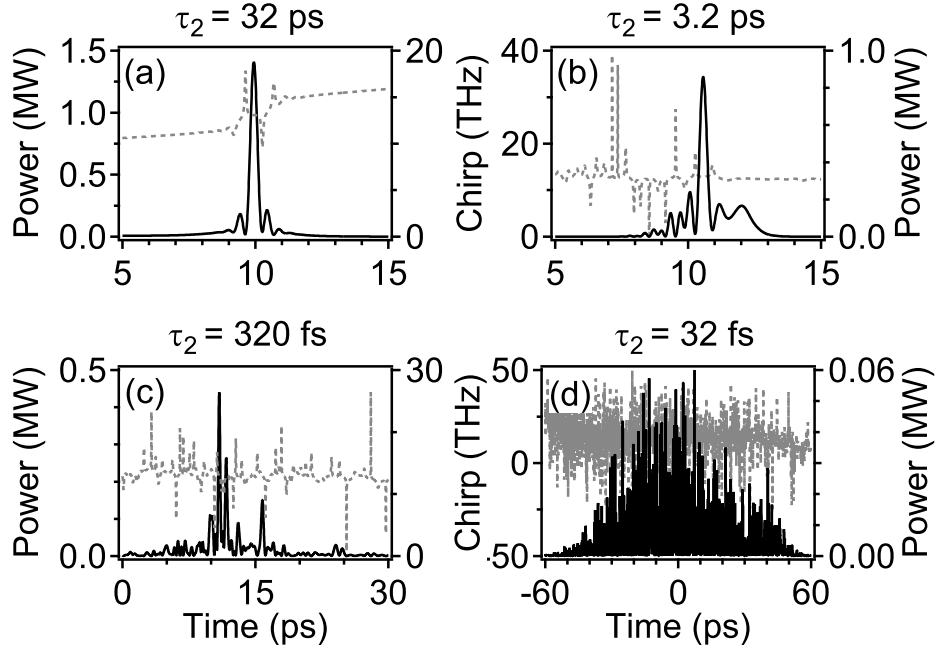
Figure 3.3: Compressed Stokes pulses (solid) and residual chirp (dashed).

3.5 Fluctuations in Stokes Pulses

Given that the generated Stokes pulses initially grows from spontaneous Raman scattering, we can expect pulse-to-pulse fluctuations in both amplitude and phase. Here we study the statistical properties of the pulses generated with long enough dephasing time to show coherence and compressibility. The distribution of the Stokes pulse energy and the peak power of the compressed pulses are shown for propagation lengths of 1.00 m, 1.25 m and 1.5 m in Figure 3.4. Each sample contains 300 shots. The amount of dispersion compensation is fixed for each length to the value maximizing the compressed peak power for a single run.

The pulse energy initially shows a wide, gaussian-like distribution. After further amplification along the fiber, the distribution narrows due to the stabilizing effects of pump depletion. This reduction in fluctuations is consistent with work done with unchirped picosecond pulses in optical fibers [18], as well as in gases [19].
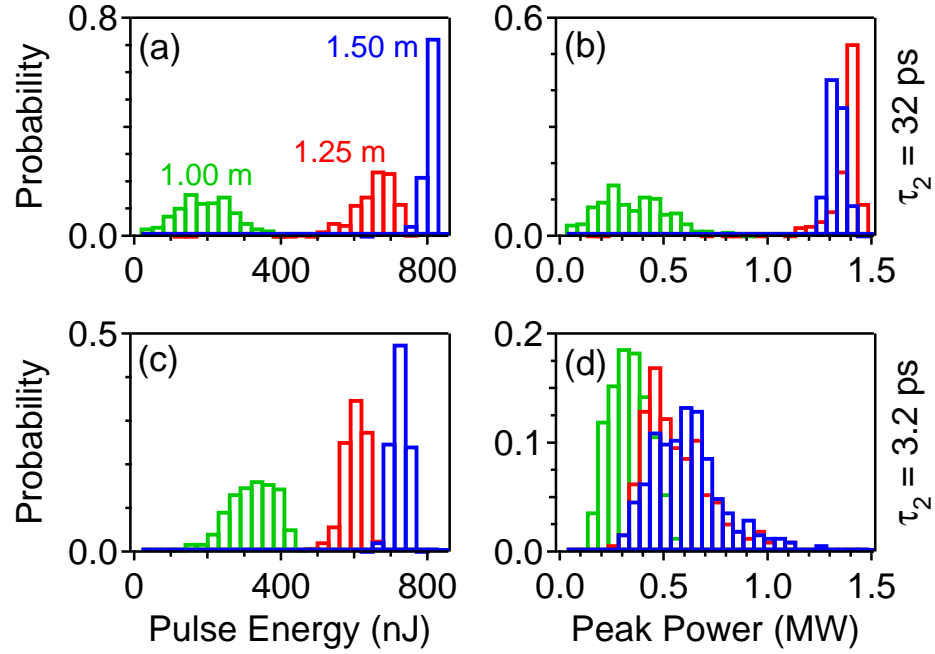
Figure 3.4: Probability distributions of Stokes pulse energy (left) and peak power (right). Propagation lengths are 1.00 m (green), 1.25 m (red) and 1.50 m (blue)

Saturation is also evident in the steepening of the distribution on the high energy side. Although the energy distributions behave similarly for dephasing times of 3.2 ps and 32 ps, the statistics of the compressed peak powers evolve differently. For a long dephasing time of 32 ps, the compressed peak power also narrows with increasing amplification. Although the energy distributions narrows further between 1.25 m and 1.50 m, the width of the peak power distribution does not significantly change. Moreover, the average peak power decreases slightly beyond 1.25 m. Inspection of the compressed temporal profile reveals that most of the additional energy is transferred to the pedestal visible in Figure 3.3(a), reducing pulse quality. For a slower dephasing time of 3.2 ps, the average peak power and the distribution width remain constant over the last two steps, despite an increase in average energy. The compressed temporal profiles reveal that most of the extra energy is channelled into secondary pulses as seen in Figure 3.3(b), preventing

further growth of the main pulse.

3.6 Discussion

The above results show that the relative magnitude of the Raman dephasing time compared to the pump pulse duration determines whether coherent phase transfer to the generated Stokes pulse is possible. For sub-ps dephasing times and ~ 100 ps chirped pump pulses, the fast dephasing fragments the Stokes pulse into incoherent bursts, preventing recompression. Thus, the peak power of recompressed pulses generated through SRS in glasses should be carefully checked, especially for pump pulse longer than a few picoseconds such as in [15]. Direct peak power checks are necessary since the short intrapulse features can appear on autocorrelations as a coherence spike whose duration is close to the bandwidth-limited duration. Exploiting SRS from long pulses in optical fibers would thus require coherent seeding at the Stokes wavelength to avoid pulse growth from low-coherence spontaneous Raman scattering.

For dephasing times greater than a ps, Stokes pulses have high internal coherence and can be recompressed to sub-ps durations, as demonstrated in barium nitrate [12]. This rapid increase in coherence, even for dephasing times only 1/30th of the pump duration, can be explained by a two-fold effect. First, the longer Raman response has a stronger smoothing effect, as represented by the convolution integral in the delayed response of Eq. 1.15. Second, the spontaneous Raman scattering that initially seeds the Stokes field has longer coherence time, thus requiring less smoothing. The secondary pulses generated with a dephasing time of 3.2 ps are probably due to transient effects from the Raman response. Indeed, these

67

features have durations close to the relevant dephasing time. Chirped pulses are particularly sensitive to transient Raman effects [20]. As indicated above, further buildup of the Stokes field channels energy into these secondary features. Thus, the single-pass efficiency of the Stokes generation process appears limited by transient effects for fast dephasing, and by self-phase modulation for slower dephasing.

Although a relatively fast dephasing of 3.2 ps generates compressible pulses, transient effects channel energy into secondary pulses, resulting in large peak power fluctuations. For a dephasing time of 32 ps, longer propagation results in higher conversion efficiency and a narrower energy distribution. However, most of the extra energy is channeled into a secondary pedestal, limiting peak power. Operating below saturation may be preferable. We expect that both higher pulse quality and lower fluctuations can be achieved using methods such as two pulse pumping [13] or multistage amplification [21].

The coherence time of the Raman response is mostly dependent on the host medium. Table 3.1 lists the Raman dephasing times of different materials. Amongst the glasses that can be drawn into fibers, the Tellurides have the longest coherence [22], about 5x that of fused silica. Bulk non-linear glasses like germanates can reach hundreds of femtoseconds of coherence [23]. However, in light of the simulations above, this is still insufficient for coherent generation of a highly chirped Stokes pulse. Coherence times on the order of picoseconds can be obtained from bulk laser materials, such as Ti:sapphire [24]. As mentioned earlier, certain crystals like barium nitrate can reach coherence times of tens of picoseconds. This suggests SRS could be exploited in several materials as a wavelength shifting tool in high-power CPA systems.

	Linewidth (cm^{-1})	Coherence τ_2
Fluoride glass [25]	320	25 fs
Fused Silica [26]	265	32 fs
As_2Se_3 glass [27]	90	93 fs
TeO_2 glass [22]	200	165 fs
Ge-Ga-S glass [23]	35	300 fs
$Ti:Al_2O_3$ [24]	0.5-1.4	2-6 ps
$Ba(NO_3)_2$ [12]	0.40	21 ps

Table 3.1: Raman linewidths and dephasing times of selected optical materials.

3.7 Conclusion

We have numerically studied the coherence properties of Stokes pulses generated by SRS in chirped-pulse amplifier systems. Raman dephasing time is a key parameter for the coherence and compressibility of Stokes pulses growing from spontaneous scattering. Remarkably, dephasing times as short as 1/30th of the pulse duration can produce Stokes pulses compressible to sub-ps durations. For faster sub-ps dephasing times, internal coherence is lost in the generated Stokes pulse, preventing compressibility of the resulting noise bursts. The results suggest that exploiting SRS in optical fibers requires careful attention to the coherence of the Stokes field. If compressibility is required, then SRS does indeed represent an upper limit to the pulse energy extractable from a fiber CPA system. On the other hand, crystalline materials used in solid-state laser systems have non-linear responses slow enough to produce coherent pulses in the present model. Exploitation of SRS in such materials is thus worth exploring, for instance as Raman shifters to extend the wavelength range of fiber CPA systems.

Bibliography

[1] S. Lefrancois and F. Wise, in *CLEO:2011 - Laser Applications to Photonic Applications* (Optical Society of America, Washington, DC, 2011), p. CThU2.

[2] H. Kalaycioglu, B. Oktem, C. Senel, P. P. Paltani, and F. O. Ilday, Opt. Lett. **35**, 959 (2010).

[3] T. Eidam, S. Hanf, E. Seise, T. V. Andersen, T. Gabler, C. Wirth, T. Schreiber, J. Limpert, and A. Tünnermann, Opt. Lett. **35**, 94 (2010).

[4] A. Braun, S. Kane, and T. Norris, Opt. Lett. **22**, 615 (1997).

[5] T. Schreiber, D. Schimpf, D. Müller, F. Röser, J. Limpert, and A. Tünnermann, J. Opt. Soc. Am. B **24**, 1809 (2007).

[6] D. N. Schimpf, J. Limpert, and A. Tünnermann, Opt. Express **15**, 16945 (2007).

[7] S. Zhou, L. Kuznetsova, A. Chong, and F. Wise, Opt. Express **13**, 4869 (2005).

[8] A. Chong, L. Kuznetsova, and F. W. Wise, J. Opt. Soc. Am. B **24**, 1815 (2007).

[9] R. H. Stolen, J. P. Gordon, W. J. Tomlinson, and H. A. Haus, J. Opt. Soc. Am. B **6**, 1159 (1989).

[10] D. Schadt and B. Jaskorzynska, J. Opt. Soc. Am. B **4**, 856 (1987).

[11] C. Headley III and G. P. Agrawal, J. Opt. Soc. Am. B **13**, 2170 (1996).

[12] N. Zhavoronkov, F. Noack, V. Petrov, V. P. Kalosha, and J. Herrmann, Opt. Lett. **26**, 47 (2001).

[13] A. V. Konyashchenko, L. L. Losev, and S. Y. Tenyakov, Quantum Electron. **40**, 700 (2010).

[14] C. Jordan, K. A. Stankov, G. Marowsky, and E. J. Canto-Said, Appl. Phys. B-Lasers O. **59**, 471 (1994).

[15] S. Zhou, T. Takamido, S. Imai, and F. Wise, Opt. Lett. **35**, 2397 (2010).

[16] R. H. Stolen and E. P. Ippen, Appl. Phys. Lett. **22**, 276 (1973).

[17] M. D. Perry, T. Ditmire, and B. C. Stuart, Opt. Lett. **19**, 2149 (1994).

[18] I. I. I. Headley C. and G. P. Agrawal, IEEE J. Quantum Electron. **31**, 2058 (1995).

[19] I. A. Walmsley, M. G. Raymer, T. S. II, I. N. D. III, and J. D. Kafka, Opt. Commun. **53**, 137 (1985).

[20] R. L. Carman, F. Shimizu, C. S. Wang, and N. Bloembergen, Phys. Rev. A **2**, 60 (1970).

[21] F. B. Grigsby, P. Dong, and M. C. Downer, J. Opt. Soc. Am. B **25**, 346 (2008).

[22] R. Stegeman, C. Rivero, G. Stegeman, P. Delfyett, K. Richardson, L. Jankovic, and H. Kim, J. Opt. Soc. Am. B **22**, 1861 (2005).

[23] I. Kang, S. Smolorz, T. Krauss, and F. Wise, Phys. Rev. B **54**, 641 (1996).

[24] S. Smolorz and F. Wise, Opt. Lett. **23**, 1381 (1998).

[25] Saïssy, A., Botineau, J., Macon, L., and Maze, G., J. Physique Lett. **46**, 289 (1985).

[26] D. Hollenbeck and C. D. Cantrell, J. Opt. Soc. Am. B **19**, 2886 (2002).

[27] J. Hu, C. R. Menyuk, L. B. Shaw, J. S. Sanghera, and I. D. Aggarwal, Opt. Express **18**, 6722 (2010).

CHAPTER 4

MULTIPULSING INSTABILITIES IN MULTIMODE FIBER LASERS[1]

In this chapter, we study the performance of mode-locked fiber lasers built using several designs of large mode area fibers. We find that the presence of unsuppressed higher order mode content in LMA fibers significantly reduces the maximum single pulse energy that can be stabilized in the cavity, indicating a destabilizing effect from multimode propagation. Careful control of higher-order mode content can restore full pulse energy scaling. This is shown in the case of step-index fiber, large core photonic crystal fiber, as well as chirally-coupled core fiber.

4.1 Introduction

As discussed in chapter 1.5, the pulse energy supported by fiber lasers can be scaled using pulse evolutions that minimize intra-cavity peak power and manage large non-linear phase shifts. A complimentary approach to scale up pulse energy is LMA fiber. A larger effective mode area scales up the peak power supported by a given pulse evolution at constant nonlinear phase shift [2]. For a given pulse evolution, the pulse energy of fiber lasers and amplifiers can be scaled up by using fibers with larger cores [2]. This reduces the intensity at a given energy and scales up the pulse energy required to achieve a given non-linear phase shift. However, large fiber cores guide multiple waveguide modes. The presence of higher-order modes (HOM) is well known to degrade beam quality in amplifiers and CW lasers, but their effects in mode-locked fiber oscillators has not been thoroughly studied.

---

[1]Much of the work in this chapter was published in the IEEE Journal of Quantum Electronics [1].

72

One can expect the coupling, interference and gain competition between different modes would negatively impact mode-locking stability.

Step index multi-mode fibers offer straightforward integration potential. Although they have found wide use in amplifiers, there has only been one isolated demonstration of their use in mode-locked oscillators [3]. It is suspected that even a small amount of residual higher-order mode (HOM) content may disrupt stable mode-locking in laser cavities. Several mechanisms have been demonstrated to filter out higher-order modes, including selective bend loss [4] and gain filtering [5]. Chirally-coupled core (CCC) fibers combine a large step-index core with a second helical core [6]. This provides an integrated mode filtering mechanism while preserving the integration potential of solid-glass step index fibers. Photonic crystal fiber (PCF) allows large effectively single-mode core, due to factors such as large propagation losses for higher-order modes and weak intermodal coupling [7, 8, 9]. The use of PCF has been popular in scientific studies, but has had less impact in practical devices due to high bend sensitivity and difficult integration with conventional fiber fusion technology.

Here we survey the performance of ANDi fiber lasers using several large core fiber designs. The optimal single-pulse performance is characterized for step-index multimode fiber, CCC fiber and large-core PCF. A link is established between the maximum single-pulse energy and the residual HOM content.

4.2   Multimode step-index fiber laser

The most straightforward way to scale to larger fiber cores is by using large mode-area step-index MMF while attempting to strip off higher-order modes. We built

the ANDi cavity presented in Figure 4.1. The gain medium is about 1.2 m of Yb-doped double-clad fiber with a core diameter of 20 μm (Liekki Yb1200-20/125). The 125 μm cladding diameter offers simple integration to telecommunication grade fiber components. The numerical aperture (NA) is 0.07, yielding a mode-field diameter (MFD) of 17 μm and a V-number of 4.3, supporting four waveguide modes. By solving the waveguide eigenvalue problem [10], the HOM closest to the fundamental LP_{01} mode is found to be LP_{11}, with a group-velocity mismatch (GVM) of 0.80 ps/m. Light from a 975 nm pump diode is injected into the cladding of the gain fiber using a homemade side-fused pump-signal combiner. To favor fundamental mode excitation, the combination of 0.35 m of fiber with an 8 μm core diameter and 0.14 NA and 0.45 m of 10 μm core diameter single-mode fiber (SMF) with a NA of 0.08 are spliced to the gain fiber through a tapered mode-field adapter inside the combiner. The total cavity length is brought to 2.6 m by splicing 0.6 m of matching passive 20 μm multimode fiber after the gain fiber. A cladding mode stripper after the gain fiber removes residual pump light. Nonlinear polarization rotation in the fibers is converted to self-amplitude modulation by three waveplates and a polarizing beamsplitter. This NPE port also serves as the output coupler. A polarizing isolator ensures unidirectional ring operation. A quartz plate placed before the isolator creates a birefringent spectral filter, enabling dissipative soliton pulse shaping. Two perpendicular coils in the gain fiber provide high loss to the higher order modes with little loss to the fundamental mode [4]. An external grating pair acts as a dispersive delay line to compensate the chirp of the output pulses.

We first operate the laser without coiling the gain fiber and thus without higher-order mode filtering. After tuning the NPE waveplates, the laser provides a stable, self-starting mode-locked pulse train at a repetition rate of 77 MHz. The mode-
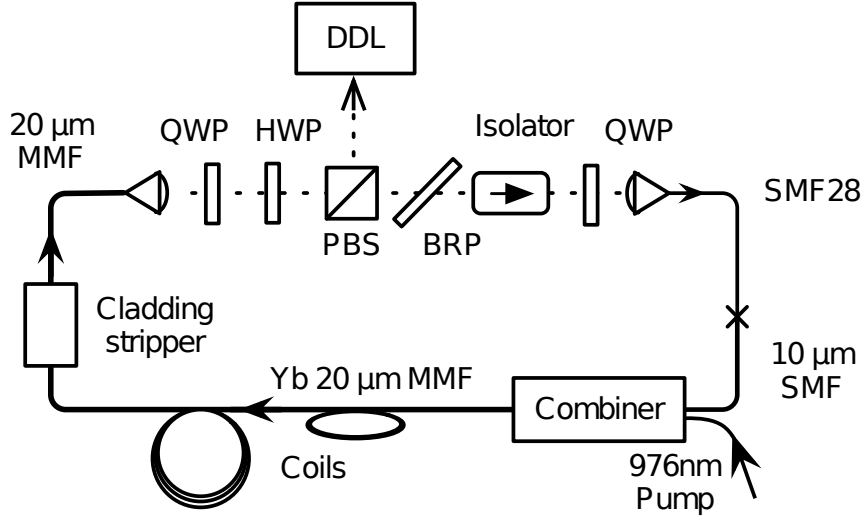
Figure 4.1: Step-index LMA ANDi setup. SMF/MMF: singlemode/multimode fiber, QWP/HWP: quarter/half waveplate, PBS: polarizing beam splitter, BRP: birefringent plate, DDL: dispersive delay line.

locked spectrum and dechirped interferometric autocorrelation (AC) using a 15-nm filter are presented in Figure 4.2(a) and (b). The single-pulse energy is 4.4 nJ, and the full-width at half-maximum (FWHM) of the AC is 250 fs, giving a pulse duration of 177 fs using a gaussian deconvolution factor. Two smaller pulses are visible $\sim$ 1.5 ps away from the main pulse. This agrees with a calculated intermodal delay of 1.4 ps between LP_{01} and LP_{11}. The spectrum shows strong modulations with a few nm period due to multi-path interference (MPI). The Fourier transform of the spectrum shown in Figure 4.2(c) qualitatively confirms the fringes correspond to the LP_{11} intermodal delay. A quantitative assessment of the HOM content would require a spatially resolved measurement such as the S^2 method [11]. The M^2 parameter was measured to be 1.33, confirming the multimode nature of the beam. If the pump power is raised further, the mode-locked state becomes unstable, then locks into similar double- and triple-pulsing states as shown in Figure 4.2(d). In the multi-pulsing states, the energy of each individual pulse is always nearly 4.2 nJ.
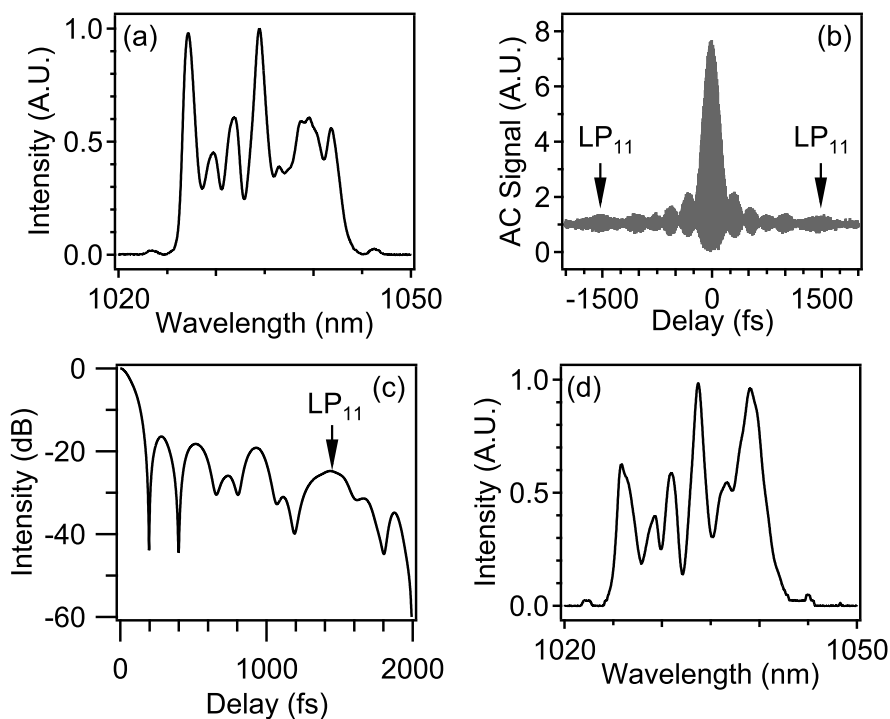
Figure 4.2: Mode-locked states of a step-index LMA ANDi without coiling: (a) spectrum and (b) dechirped interferometric AC of single pulsing state at 4.0 W of pump, (c) Fourier Transform of (a) showing secondary pulse and (d) double pulsing at 4.9 W pump.

The linear coupling between fiber modes is determined by random refractive index variations and microbends in the fiber core, and can only be addressed during fiber fabrication. We instead control the higher order mode loss by coiling the fiber on two perpendicular axes [4]. We found mode-locked states with coiling diameters from 8 cm to 4 cm, with prohibitive bending losses at smaller diameters. Figure 4.3(a)-(b) shows a single-pulsing mode-locked state at a coiling diameter of 4 cm with a 15 nm filter. The pulse energy is 21 nJ, and from the dechirped AC we infer a dechirped pulse duration of 115 fs. Filtering of the higher-order modes clearly allows higher pulse energies. This wide-bandwidth mode is similar to the highly structured mode in Figure 12 (h) of [12]. Up to its sensitivity limit, the autocorrelation trace shows no secondary pulse at the LP_{11} delay, confirming
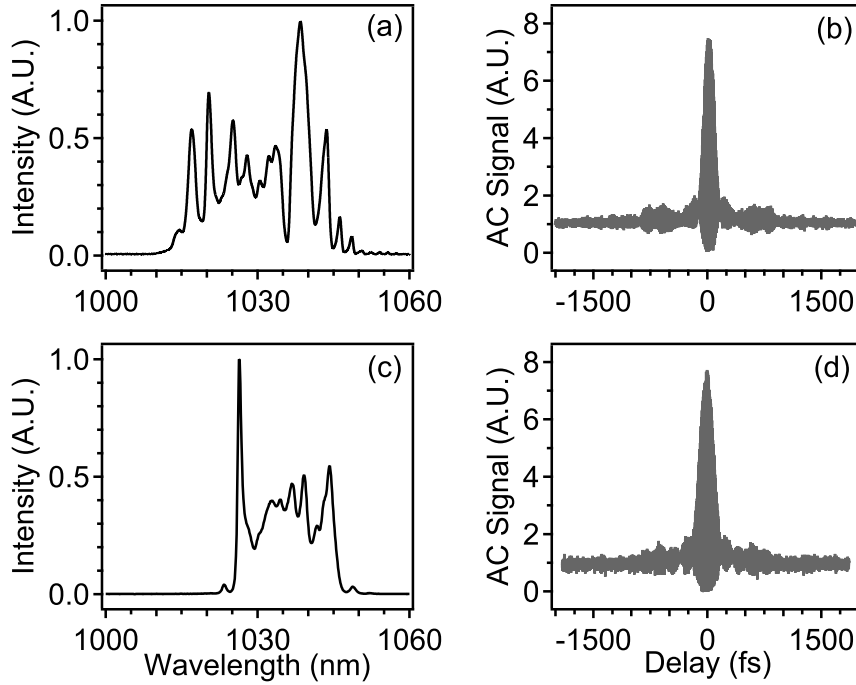
Figure 4.3: Mode-locked states of a step-index LMA ANDi with the gain fiber coiled to a diameter of 4 cm. Spectrum and dechirped interferometric AC using: (a)-(b) 15 nm filter, (c)-(d) 20 nm filter.

lower HOM content. Figure 4.3(c)-(d) present a similarly stabilized mode-locked state with a coiling diameter of 4 cm and a 20 nm filter. The pulse energy and inferred dechirped duration are 12 nJ and 150 fs. Secondary LP_{11} pulses are again not detected above the noise floor of the autocorrelation.

Although energies of up to 21 nJ are achieved in this multimode fiber laser, this is well below that of a previously-built laser with 10 μm core diameter single-mode fiber [13]. This laser provided pulse energies up to 31 nJ with a similar 2 m cavity. By scaling the MFD from 11 μm to 17 μm, we would expect pulse energies up to 75 nJ from the 20 μm core ANDi. This indicates that despite coiling, higher-order modes are not sufficiently controlled in the step-index LMA cavity, and their presence limits the maximum single pulsing energy that can be stabilized.

4.3 CCC fiber laser

An optimal mode control mechanism should be built into the fiber design rather than depend on external manipulations. This is the case of chirally-coupled core (CCC) fibers [6]. In such a fiber, a secondary core is wrapped in a helix around the main core. The pitch and chirality of the helix are chosen to selectively couple out modes other than the fundamental through quasi-phasematched resonances. We show results from an ANDi laser based on 3.9 m of Yb-doped CCC fiber. The fiber core diameter is 33.5 μm with a NA of 0.06. This yields a MFD of 21 μm and V = 6.03, supporting six modes. The LP_{11} mode has a calculated GVM of 0.5 ps/m with LP_{01}. A detailed characterization of the performance of the laser is presented in chapter 5. Here we put the results in the context of multimode propagation. Figure 4.4 presents a self-starting single-pulsing state obtained with an 8 nm filter. The pulse energy is 47 nJ and we infer a dechirped pulse duration of 225 fs from the AC. The small spectral modulation at the center indicate low HOM content, confirmed by the absence of any secondary pulse up to the 30 dB noise floor of the autocorrelation trace. The M^2 is measured to be 1.1 to 1.15 in CW and mode-locked states, confirming HOM filtering. When normalized to the mode-area of the fiber, these results are comparable to those a single-mode ANDi laser with similar dispersion and output spectral bandwidth. Pulse energies of about 4-5 nJ and 200 fs dechirped durations are shown in Figure 12(f) and Figure 13 of [12], using a fiber with a mode area 12 times smaller. This confirms that the robust and continuous mode filtering in the CCC fiber helps stabilize a multimode core to singlemode mode-locked performance.
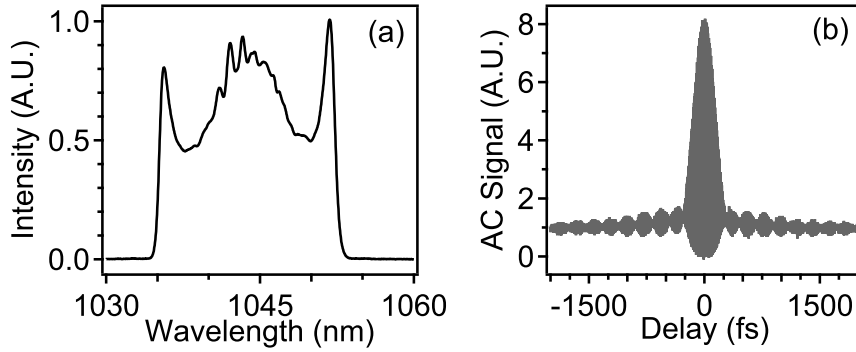
Figure 4.4: Mode-locked state of a LMA CCC fiber ANDi laser: (a) spectrum and (b) dechirped interferometric AC.

4.4 LMA PCF laser

Another monolithic mode-filtering mechanism is the large mode-area photonic crystal fiber. We present results from a laser built around such a LMA PCF. The details of the setup as well as representative mode-locked states are discussed in chapter 7. The central element is 1.25 m of Yb-doped LMA PCF with a core diameter of 40 μm, an effective NA of 0.03 and a MFD of $\sim$33 μm. The photonic lattice is hexagonal with a pitch of 12.3 μm and a hole diameter of 1.1 μm [9]. Although this seven missing hole design is not endlessly single mode, the modal propagation constants are far enough to suppress intermodal coupling over the length of the fiber. This results in effectively single-mode behavior if the fundamental mode is properly seeded.

Two lasers were built using the same cavity design and distinct PCFs with essentially identical specifications (Crystal Fibre DC-170-40-Yb and DC-170-40-Yb-2). Figure 4.5 shows self-starting mode-locked states obtained using each fiber. The first fiber is presented in Figure 4.5(a)-(b) and yields a single pulsing state with energy 124 nJ, and the state from the second fiber in Figure 4.5(c)-(d) is double

pulsing with an average energy of 47 nJ per pulse. The first PCF laser shows very weak spectral modulations and no visible secondary pulse on its autocorrelation, indicating essentially singlemode propagation. Although the fibers are essentially singlemode by specification, the second fiber clearly displays significant higher-order mode content as evidenced by the strong modulations on the mode-locked spectrum. This could be due to inconsistencies in the fabrication process allowing higher-order modes to be guided. Excitation of multiple modes at the fiber input could also seed secondary modes, although identical setups and alignment procedures were used for both lasers. The singlemode PCF yields single pulse energies of up to 154 nJ, limited by available pump power, while the effectively multimode PCF only provides up to 60 nJ before the onset of multipulsing instabilities. This corroborates the conclusions from the step-index ANDi laser that the presence of unfiltered higher-order mode content limits the maximum single pulse energy accessible in the cavity.

It should be noted that regular PCFs with cores diameters larger than 40 μm require the addition of extra mode filtering in the cavity. Indeed, photonic crystal rod lasers, such as in [14, 15], use a piece of single mode fiber as an intracavity spatial mode filter. This has recently been overcome by large-pitch PCF designs which provide strong HOM filtering [16, 17]

4.5   Multipulsing threshold and multimode propagation

A rough estimate of the HOM content delivered by a laser can obtained through spectral interference. With femtosecond bandwidth pulses, secondary pulses with delays on the order of picoseconds can be observed as spectral interference fringes.
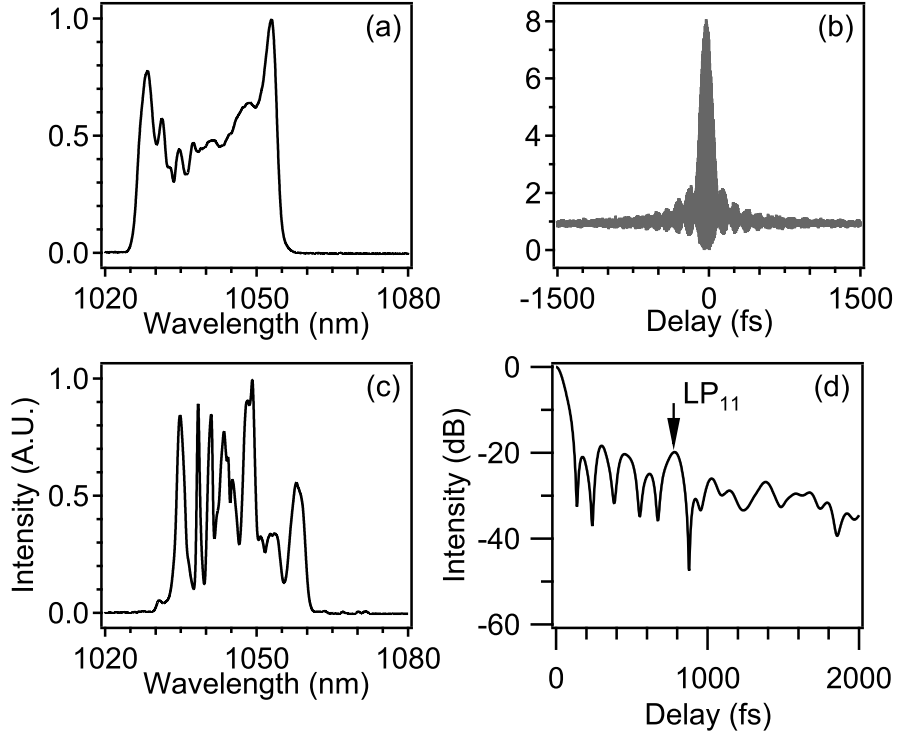
Figure 4.5: Mode-locked states of a LMA PCF based ANDi laser. (a)-(b) Spectrum and dechirped interferometric AC of the effectively single mode PCF, (c)-(d) spectrum and its Fourier transform for the effectively multimode PCF.

Taking the Fourier Transform of a pulse with intensity $I_1(x, y, t)$ and a second one $I_2 = \alpha^2(x, y)I_1(x, y, t - \tau_d)$ delayed by τ_d, the resulting power spectrum is:

$$S(x, y, \omega) = I_1(x, y, t)[1 + \alpha^2(x, y) + 2\alpha(x, y)\cos(\tau_d\omega)]. \qquad (4.1)$$

Thus, the field amplitude of the dominant higher-order mode (HOM), usually LP_{11}, can be inferred from the amplitude of the spectral fringes. Using a wide aperture spectrometer (about 1 mm in this study), we can estimate the average multi-path interference $MPI = 10\log(P_i/P_0)$ by taking the Fourier transform of the spectrum and evaluating the amplitude of the secondary pulse corresponding to the HOM, as seen in Figure 4.1. When a secondary pulse is directly visible in the pulse autocorrelation, this estimate agrees with the measured amplitude to within a few percent. Due to the symmetric nature of the intensity spectrum, the MPI is

81

twice the measured amplitude to account for the power at $\pm\tau_d$. Although a more quantitative and mode discriminating characterization would require a spatially resolved technique such as the S^2 method [11], this average spectral interference method provides a crude estimate of HOM influence on mode-locking.

To summarize this experimental survey of LMA ANDi fiber lasers, Figure 4.6 plots the maximum single pulse energies obtained with the different fibers and mode filtering mechanisms as a function of dominant MPI content inferred from spectral modulations. For each cavity, we selected modes with similar bandwidths (BW) and thus comparable peak powers. The pulse energies are normalized to the fundamental mode area ($\sim$30 μm^2) of a standard SMF at a 1 μm wavelength.
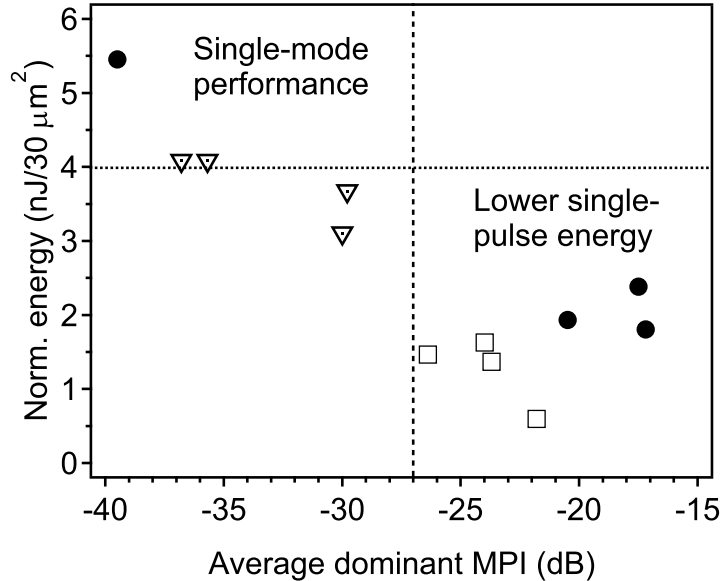
Figure 4.6: Normalized maximum single pulse energies vs. dominant MPI content inferred from spectral modulations for step-index MMF with 17 nm output BW (squares), PCF with 26 nm output BW (filled circles) and CCC with 17 nm output BW (dotted triangles) ANDi fiber lasers. Dotted line: typical energy from a $\sim$200 fs SMF ANDi laser; dashed line: observed MPI limit for single-mode performance.

The complex and diverse pulse shapes obtained with ANDi cavities complicates

the identification of spectral features corresponding to secondary pulses, so we will not attempt to extract a rigorous trend. However, there is a clear indication that filtering out HOM content enables higher pulse energies to be reached. Indeed, the singlemode PCF as well as the CCC cavities both lie in the high-energy/low-MPI part of the graph. Above an averaged MPI of ∼ -27 dB, fiber laser cavities fail to attain the single pulse energies expected from scaling SMF results. This is consistent with the level of HOM content observed in an effectively single-mode step-index soliton laser [3], and gives a quantitative assessment of the effectively single-mode regime. Mode-locked fiber laser performance thus seems critically affected by multimode content. Whereas HOM content in an amplifier or CW laser mainly results in a degradation of beam quality, our results show that it limits the maximum single-pulsing energy attainable in a mode-locked oscillator.

4.6   Conclusion

The experimental findings in this chapter indicate that unsuppressed higher-order spatial modes severely affect the performance of mode-locked fiber lasers. Whereas HOM content in amplifiers and CW lasers mainly affects beam quality, the experiments presented here show that the maximum stable single pulse energy achievable in mode-locked oscillators is greatly reduced from the limit expected by scaling the core size. This indicates that mode-locking is fundamentally destabilized when secondary mode content becomes significant enough. Experimentally, large core step-index fiber shows the largest performance degradation, yielding about 4 nJ of pulse energy compared to an expected energy of 75 nJ. Mode-filtering using selective bend loss raises the maximum pulse energy to 20 nJ, but still underperforms singlemode sources. In practice, full pulse energy scaling is achievable only with

careful mode management mechanisms. This is demonstrated for large mode-area PCF as well as chirally-coupled core fibers whose mode-locked performance scales as expected with core size.

Bibliography

[1] E. Ding, S. Lefrancois, J. N. Kutz, and F. W. Wise, IEEE J. Quantum Electron. **47**, 597 (2011).

[2] N. G. R. Broderick, H. L. Offerhaus, D. J. Richardson, and R. A. Sammut, IEEE Photonic Tech. L. **10**, 1718 (1998).

[3] M. E. Fermann, A. Galvanauskas, and M. Hofer, Appl. Phys. B-Lasers O. **70**, S13 (2000).

[4] J. P. Koplow, L. Goldberg, and D. A. V. Kliner, Opt. Lett. **25**, 442 (2000).

[5] J. R. Marciante, IEEE J. Sel. Top. Quant. **15**, 30 (2009).

[6] C.-H. Liu, G. Chang, N. Litchinitser, A. Galvanauskas, D. Guertin, N. Jabobson, and K. Tankala, in *Advanced Solid-State Photonics* (Optical Society of America, Washington, 2007), p. ME2.

[7] B. T. Kuhlmey, R. C. McPhedran, and C. M. de Sterke, Opt. Lett. **27**, 1684 (2002).

[8] N. A. Mortensen, M. D. Nielsen, J. R. Folkenberg, A. Petersson, and H. R. Simonsen, Opt. Lett. **28**, 393 (2003).

[9] J. Limpert, A. Liem, M. Reich, T. Schreiber, S. Nolte, H. Zellmer, A. Tunnermann, J. Broeng, A. Petersson, and C. Jakobsen, Opt. Express **12**, 1313 (2004).

[10] D. Marcuse, *Theory of Dielectric Waveguides* (Academic Press, New York, 1974).

[11] J. W. Nicholson, A. D. Yablon, S. Ramachandran, and S. Ghalmi, Opt. Express **16**, 7233 (2008).

[12] A. Chong, W. H. Renninger, and F. W. Wise, J. Opt. Soc. Am. B **25**, 140 (2008).

[13] K. Kieu, B. G. Saar, G. R. Holtom, X. S. Xie, and F. W. Wise, Opt. Lett. **34**, 2051 (2009).

[14] B. Ortaç, M. Baumgartl, J. Limpert, and A. Tünnermann, Opt. Lett. **34**, 1585 (2009).

[15] C. Lecaplain, B. Ortaç, G. Machinet, J. Boullet, M. Baumgartl, T. Schreiber, E. Cormier, and A. Hideur, Opt. Lett. **35**, 3156 (2010).

[16] F. Stutzki, F. Jansen, T. Eidam, A. Steinmetz, C. Jauregui, J. Limpert, and A. Tünnermann, Opt. Lett. **36**, 689 (2011).

[17] M. Baumgartl, C. Lecaplain, A. Hideur, J. Limpert, and A. Tünnermann, Opt. Lett. **37**, 1640 (2012).

CHAPTER 5

ENERGY SCALING OF DISSIPATIVE SOLITON LASERS BASED ON CCC FIBER[1]

In this chapter, we present a dissipative soliton laser based on Yb-doped large mode-area CCC fiber. This is the first mode-locked laser to use CCC fiber, and demonstrates its ability to scale the pulse energy of ultrafast fiber lasers in a solid glass package with low bend sensitivity and compatibility with fiber fusion technology. The performance matches simulations of dissipative soliton pulse evolution, as well as pulse energies expected from scaling of single-mode ANDi fiber lasers. Beam quality, spectral interference and a high single-pulsing limit demonstrate effectively single-mode operation. The oscillator provides chirped pulses of energies greater than 40 nJ, which dechirp to below 200 fs . With a shorter fiber, pulse durations close to 100 fs are achieved at chirped pulse energies of 22 nJ, limited by the available pump power.

5.1   Introduction

A larger effective fiber mode area scales the peak power supported by a given pulse evolution at constant nonlinear phase shift [2]. So far, the most successful technology for scaling to large singlemode fiber cores has been photonic crystal fibers (PCF) and rods [3]. Oscillators that reach the megawatt peak powers have been reported based on this approach [4, 5]. Despite their impressive performance, lasers based on PCF have found little practical application; integration into fiber devices is hindered by incompatibility with fusion splicing and sensitivity to bend loss. Large mode-area step-index fibers offer superior integration potential. There

---

[1]The work presented in this chapter is reported in Optics Express [1].

is a brief and isolated report of a modelocked soliton laser based on multimode fiber [6]. However, as outlined in chapter 4, conventional step-index fibers cannot suppress HOMs sufficiently to allow stable modelocking at high single-pulse energies. Small amounts of energy in HOMs cause multi-pulsing at energies well below those expected from mode-area scaling. There is thus a need for a distributed transverse mode filtering mechanism that is robust enough for an application as sensitive as ultrafast modelocking, yet retains the integration potential of all-glass fibers. Leaky waveguides that selectively couple out HOMs while maintaining low losses on the fundamental mode provide such a mechanism. Examples include leakage channel fibers [7], as well as Bragg fiber for which a mode-locked oscillator was recently demonstrated [8]. Another implementation of selective leakage is chirally-coupled core (CCC) fiber, which use a secondary core wound around a large central core to create a distributed and integrated HOM filtering mechanism [9]. Using no external mode-filtering or mode-matching methods, CCC fiber systems have shown effectively single-mode performance. Although a continuous-wave (CW) laser based on Yb-doped CCC fiber has been demonstrated [10], an application as sensitive as ultrafast modelocked lasers requires its own investigation.

Here we present a mode-locked high energy ANDi fiber laser based on Yb-doped CCC fiber. The dissipative soliton pulse evolution is modeled. Beam quality and higher-order mode suppression are characterized. Finally, output pulse performance is characterized for two total fiber lengths and compared to equivalent single-mode fiber lasers.

5.2 Design and modeling

The central component of the oscillator is an Yb-doped CCC fiber provided by the University of Michigan and Arbor Photonics. It has a core diameter of 33.5 μm and a numerical aperture (NA) of 0.06, which yields an effective area of $\sim 350~\mu\text{m}^2$ and a $V = 6.1$. This core nominally supports six modes. To suppress these HOMs, a secondary leaky side core is wrapped in a helix in optical proximity around the main core, as can be seen in Figure 5.1(a). Central modes can be coupled into the secondary core selectively through quasi-phase-matched interactions that involve the optical angular momentum of each mode in this helically symmetric structure. By properly choosing the diameter and the NA of the secondary core as well as the helix properties, the HOMs with azimuthal numbers $l \geq 1$ can be coupled out while keeping the $l = 0$ fundamental mode off-resonance [9].
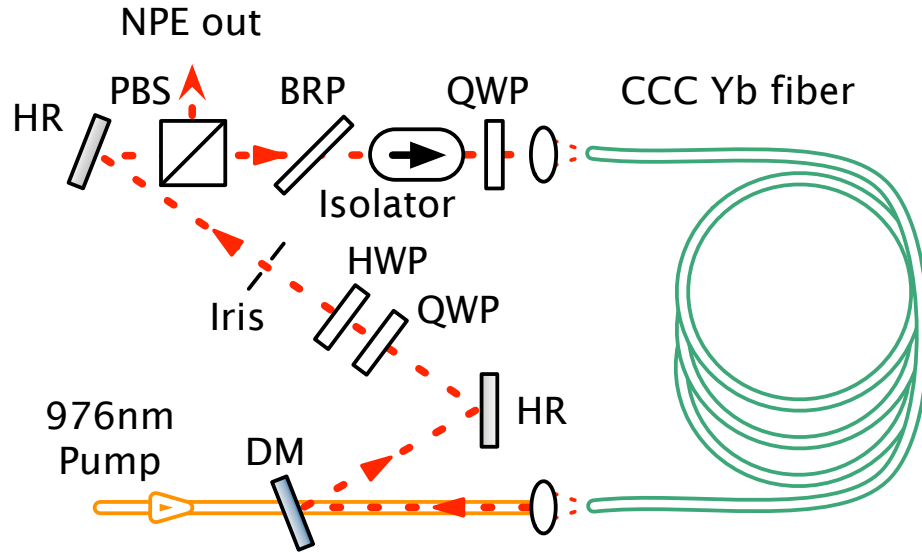
Figure 5.1: (a) Side view of angle-cleaved CCC fiber. (b) CCC fiber oscillator design: DM, dichroic mirror; PBS, polarizing beamsplitter; DDL, dispersive delay line; BRP, birefringent plate; QWP and HWP, quarter- and half-waveplate; HR, dielectric mirror.

We built a ring laser based on the ANDi design, as shown in Figure 5.1(b). The cladding of the fiber has a diameter of 250 μm, and a low-index coating provides a cladding NA of 0.46. The absorption at wavelengths around 975 nm is 5 dB/m. We used 3.9 m of Yb CCC fiber to obtain efficient pump absorption. The fiber was loosely coiled with a 30 cm diameter to avoid bend loss and external HOM filtering. The light from a fiber-coupled diode bar that provides up to 35 W at 976 nm is coupled through a dichroic mirror into the cladding of the fiber. An isolator ensures unidirectional operation. The nonlinear polarization evolution (NPE) in the fiber is converted into amplitude modulation by three wave plates and a polarizing beamsplitter. This NPE port also functions as a variable output coupler. A quartz plate placed in front of the input polarizer of the isolator creates a birefringent spectral filter. An iris placed before the output filters out residual cladding light. An external grating compressor compensates the chirp of the output pulses. The present cavity uses free-space coupling of pump and signal given the novel nature of CCC fiber. However, the solid glass nature of such fibers is compatible with the development of fused components such as pump/signal combiners.

To verify that the cavity supports dissipative solitons, we performed split-step Fourier simulations of the non-linear Schrödinger equation, as in [11]. The group-velocity dispersion is $\beta_2 = 23$ ps^2/km and the Kerr non-linearity is $\gamma = 0.40$ (W km)$^{-1}$. The small signal gain is $\sim$ 30 dB and we use a saturation energy $E_{sat} = 38$ nJ. An output coupling of 0.92 is followed by an instantaneous saturable absorber and an 80% effective linear loss. The gain filter has a 40 nm bandwidth. A stable solution starting from white noise and using a filter bandwidth of 8 nm is shown in Figure 5.2. The chirped pulse duration and spectral bandwidth increase in the CCC fiber. The saturable absorber has a small effect on the final state, and the spectral filter shapes the chirped pulse to self-consistency

with large temporal and spectral breathing. The solution taken after the saturable absorber has a pulse energy of 40 nJ and a transform-limited duration of 170 fs.
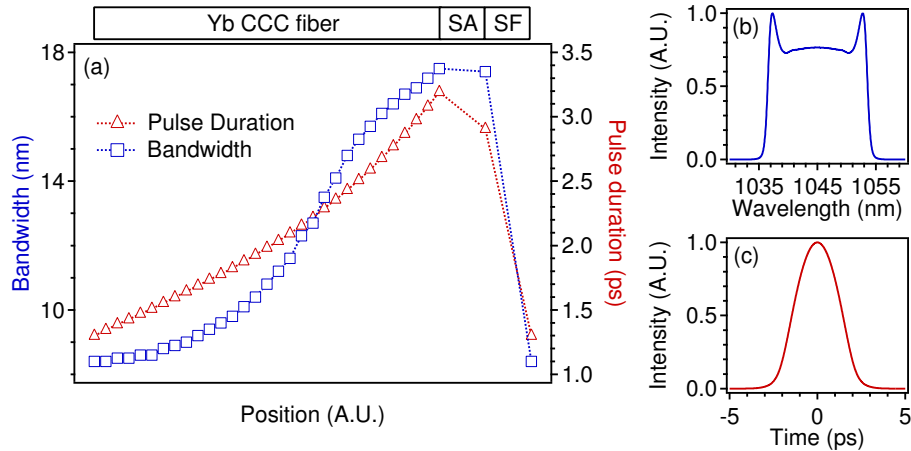
Figure 5.2: (a) Simulated pulse evolution: SA, saturable absorber; SF, spectral filter. Output pulse (b) spectrum and (c) chirped time profile.

5.3 Experiments

Experimentally, a variety of self-starting mode-locked states are obtained by adjusting the wave plates. The laser outputs a stable pulse train at 53 MHz, which was monitored using a sampling oscilloscope with 30 ps resolution, and single-pulsing was checked with an autocorrelator with up to 60 ps delay. Beam quality measurements are shown in Figure 5.3. The beam profile is gaussian. In both CW and mode-locked operation at 2.5 W and 1.9 W output power respectively, we measured $M^2 \sim 1.10 - 1.15$, consistent with $M^2 \leq 1.1$ we measured from singlemode sources. A similar oscillator using fibers with 20 μm core diameter and 0.07 NA yielded $M^2 \sim 1.3 - 1.7$ [12]. Combined with the absence of any secondary pulse on the long-range autocorrelation (AC) in Figure 5.3(c), this confirms robust

filtering of the higher-order modes by the CCC fiber.
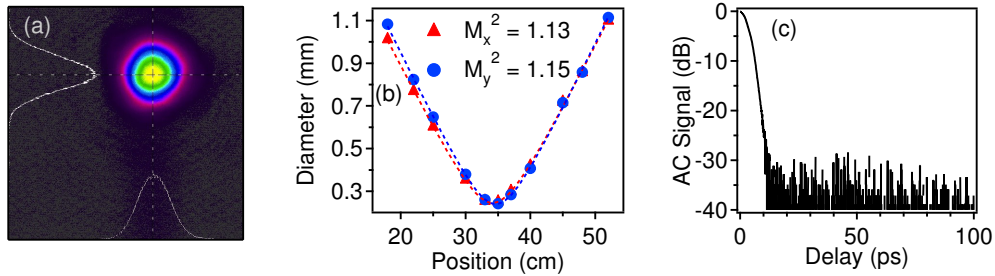
Figure 5.3: Mode-locked beam characteristics around 2 W output power: (a) beam profile, (b) M^2 measurement and (c) long-range AC.

Data from a representative mode-locked state using an 8-nm filter are presented in Figure 5.4. This state is sustained over hours, and equivalent states have been reproduced over several weeks. With about 15 W of coupled pump power, the average output power is 2.3 W, which corresponds to a chirped pulse energy of 43 nJ, in agreement with simulations. The dechirped pulse duration is 195 fs. This is within 10% of the transform-limited pulse duration inferred from the zero-phase Fourier transform of the power spectrum. Our compressor yields 28 nJ of dechirped energy, corresponding to more than 125 kW of peak power. Stable pulse energies of up to 47 nJ were obtained, but the pulses had larger wings, extending out to $\sim$ 1 ps from the peak. Increasing the pump power further results in a multipulsing instability. The spectrum displays modulations that we attribute to spectral interference with a small amount of HOM content. From the amplitude of the spectral modulation, we infer that the HOMs carry on the order of 0.1% of the energy, consistent with the absence of any secondary pulse on the long-range AC as previously shown. No measurable increase in secondary mode content is thus observed over the operating range of the laser.
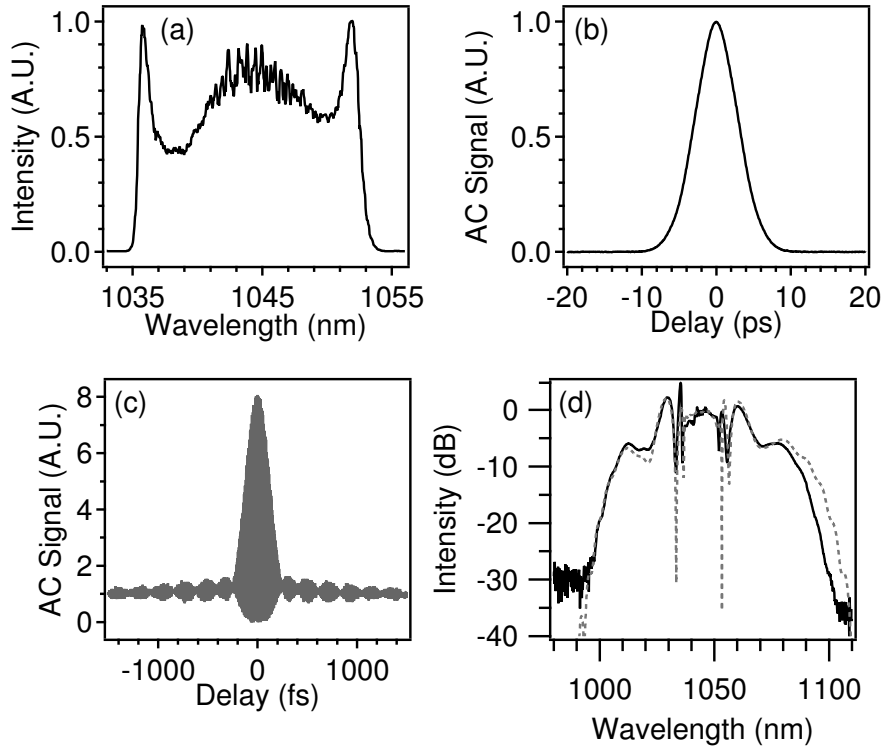
Figure 5.4: Experimental mode-locked pulse from 3.9 m cavity at 2.3 W output power: (a) spectrum (0.1 nm res.), (b) chirped AC, (c) dechirped interferometric AC. (d) Spectrum after propagation trough 1 m of SMF (solid) compared to simulation (dashed).

To verify the peak power, we launched 2 nJ dechirped pulses into 1 m of single-mode fiber (SMF) with a 5 μm core diameter and NA of 0.14. The self-phase modulation (SPM)-induced spectral broadening is shown in Figure 5.4(d). We compare the spectrum with a split-step simulation starting from a simulated pulse as in Figure 5.2. The calculation accounts for dispersion up to the third order, SPM, intrapulse Raman scattering and small under-compensation of chirp from the grating compressor. The simulation reproduces the complex spectrum of the measured pulse quite accurately, which confirms that the energy is indeed located in the main pulse.

Although the current results do not set new performance records for fiber lasers, we can verify that the performance of CCC fiber scales correctly with mode area. We make a controlled comparison between this laser and an SMF-based ANDi laser with similar cavity dispersion, spectral filtering and output bandwidth. With an effective area of $\sim 30~\mu\mathrm{m}^2$, such a cavity reaches pulse energies of 4-5 nJ as shown in Figure12-13 of [11]. This scales by a factor of ~ 10 from the CCC results as expected, demonstrating sufficient higher-order mode suppression for high energy mode-locking [12]. With the correct pulse energy scaling demonstrated, the general trends of ANDi lasers should apply. There are indications that such lasers can be optimized for short pulses or high energy using lower or higher net dispersion respectively [13, 14]. As a preliminary example, results from a cavity using 1.8 m of CCC gain fiber and a 15 nm spectral filter are shown in Figure 5.5. The pulse dechirps to 105 fs duration, very close to the transform limit. The chirped pulse energy is pump-limited to 22 nJ at 88 MHz repetition rate.
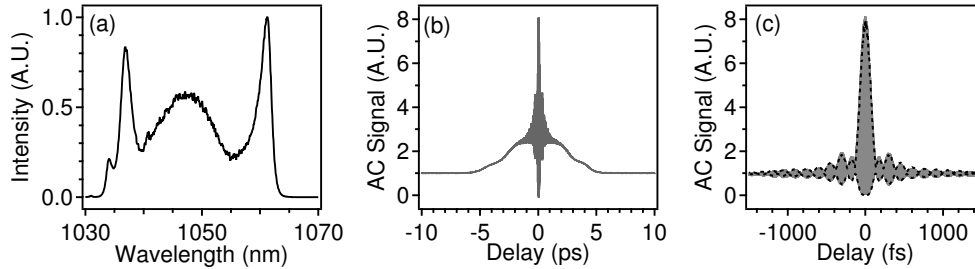
Figure 5.5: Experimental pulse from 1.8 m cavity: (a) spectrum, (b) chirped and (c) dechirped interferometric AC (solid grey) compared to calculated transform limited AC (dashed).

5.4 Conclusion

To summarize, we have demonstrated the energy scaling of modelocked fiber lasers by use of a chirally-coupled core fiber. The performance of a dissipative-soliton laser agree well with simulations that assume single-mode propagation, and scales correctly with mode area from equivalent SMF lasers. Self-starting pulse trains are obtained, with chirped pulse energies above 40 nJ and dechirped durations below 200 fs. A lower-dispersion cavity yields pulses as short as 100 fs, as expected from previous results. Although the current design uses free-space optics for pump and signal coupling, the solid glass design of CCC fiber is compatible with integration into monolithic fused fiber components, as will be shown in chapter 6. Having demonstrated sufficient higher-order mode suppression and effective core size scaling for an application as exacting as femtosecond mode-locked oscillators, we anticipate that CCC fiber can enable robust, integrated and high power ultrafast sources.

Contemporary to this work, an independent demonstration of a CCC fiber oscillator in a stretched-pulse cavity design was reported [15].

Bibliography

[1] S. Lefrancois, T. S. Sosnowski, C.-H. Liu, A. Galvanauskas, and F. W. Wise, Opt. Express **19**, 3464 (2011).

[2] N. G. R. Broderick, H. L. Offerhaus, D. J. Richardson, and R. A. Sammut, IEEE Photonic Tech. L. **10**, 1718 (1998).

[3] A. Tünnermann, T. Schreiber, and J. Limpert, Appl. Opt. **49**, F71 (2010).

[4] S. Lefrançois, K. Kieu, Y. Deng, J. D. Kafka, and F. W. Wise, Opt. Lett. **35**, 1569 (2010).

[5] C. Lecaplain, B. Ortaç, G. Machinet, J. Boullet, M. Baumgartl, T. Schreiber, E. Cormier, and A. Hideur, Opt. Lett. **35**, 3156 (2010).

[6] M. E. Fermann, A. Galvanauskas, and M. Hofer, Appl. Phys. B-Lasers O. **70**, S13 (2000).

[7] L. Dong, H. A. McKay, L. Fu, M. Ohta, A. Marcinkevicius, S. Suzuki, and M. E. Fermann, Opt. Express **17**, 8962 (2009).

[8] C. Lecaplain, A. Hideur, S. Février, and P. Roy, Opt. Lett. **34**, 2879 (2009).

[9] C.-H. Liu, G. Chang, N. Litchinitser, A. Galvanauskas, D. Guertin, N. Jabobson, and K. Tankala, in *Advanced Solid-State Photonics* (Optical Society of America, Washington, 2007), p. ME2.

[10] S. Huang, C. Zhu, C.-H. Liu, X. Ma, C. Swan, and A. Galvanauskas, in *Conference on Lasers and Electro-Optics/International Quantum Electronics Conference* (Optical Society of America, Washington, DC, 2009), p. CThGG1.

[11] A. Chong, W. H. Renninger, and F. W. Wise, J. Opt. Soc. Am. B **25**, 140 (2008).

[12] E. Ding, S. Lefrancois, J. N. Kutz, and F. W. Wise, IEEE J. Quantum Electron. **47**, 597 (2011).

[13] N. B. Chichkov, K. Hausmann, D. Wandt, U. Morgner, J. Neumann, and D. Kracht, Opt. Lett. **35**, 3081 (2010).

[14] A. Chong, W. H. Renninger, and F. W. Wise, Opt. Lett. **32**, 2408 (2007).

[15] H.-W. Chen, T. Sosnowski, C.-H. Liu, L.-J. Chen, J. R. Birge, A. Galvanauskas, F. X. Kärtner, and G. Chang, Opt. Express **18**, 24699 (2010).

CHAPTER 6

HIGH ENERGY AMPLIFIER SIMILARITON LASER BASED ON

INTEGRATED CCC FIBER[1]

In this chapter, we report a fiber laser combining the amplifier similariton evolution with chirally-coupled core fiber. We demonstrate for the first time a fused pump-signal combiner for double-clad pumping of CCC fiber, enabling integrated high-energy short pulse oscillators. Chirped pulse energies above 60 nJ are obtained with dechirped pulse durations below 90 fs. Numerical simulations confirm that a high-quality parabolic pulse evolves self-similarly inside the cavity. Peak powers approaching half a megawatt can be obtained, which to our knowledge is the highest delivered from a fiber laser with integrated pump coupling.

6.1 Introduction

As discussed in chapter 5, CCC fiber offers robust distributed mode-filtering and can enable high energy mode-locked fiber lasers. A dissipative soliton fiber laser was demonstrated with the energy scaling factors expected given the larger core. However, the lowest pulse dechirped duration achievable was around 105 fs. Scaling dissipative solitons lasers to shorter durations is possible but requires careful optimization [2]. In contrast, the amplifier similariton pulse evolution supports large spectral breathing. Pulses from such lasers can be dechirped below 60 fs with a standard grating compressor [3].

Applying LMA fiber designs to amplifier similariton lasers would enable ultrafast sources competing firmly with solid state lasers in both energy and pulse

---

[1]Parts of the work presented in this chapter was presented at CLEO 2012 [1]. A manuscript is under preparation for submission to Optics Letters.

duration. A first demonstration used 10 μm core diameter singlemode fiber yielded up to 20 nJ of chirped pulse energy. Pulse durations as low as 40 fs were obtained using adaptive pulse shaping [4]. Combining CCC fiber with the similariton design is a natural next step.

Another major advantage of CCC fiber is its solid-glass design. This makes it fully compatible with fusion splicing and other fused-fiber techniques. However, all reported uses of CCC fiber so far used isolated fiber and free space coupling. One of the most critical parts of a fiber laser is pump coupling, which involves separately aligning two beams into a single fiber. Demonstrating a fused pump-signal coupler for CCC fiber will be a key step in realizing the fibers full integration potential.

Here we present a high energy amplifier similariton fiber laser based on Yb-doped CCC fiber. A cavity design with integrated pump coupling is described and the similariton evolution is modeled. Experimental mode-locking trends and optimal pulse performance are then characterized.

6.2   Design and modeling

The amplifier similariton cavity design is shown in Figure 6.1. The gain fiber is 3 m of Yb-doped CCC fiber as in chapter 5, with a core diameter of 33 μm and a numerical aperture (NA) of 0.06, corresponding to an effective area $A_{eff} \approx$ 350 μm^2. The side-fused pump-signal combiner was fabricated by ITF Labs in Canada for the University of Michigan. The fibers are spliced together using a standard fusion splicer. The combiner contains about 50 cm of matching passive CCC fiber. A multimode diode pump at 976 nm is coupled into the fiber cladding through one of two pump fibers with 100 μm core diameter and NA of 0.22. A
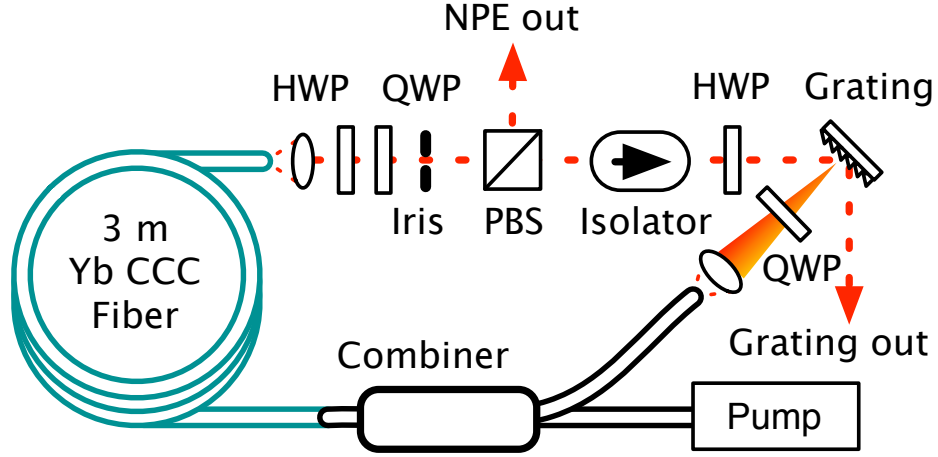
Figure 6.1: Setup for CCC fiber amplifier similariton laser. PBS: polarizing beam-splitter, SA: saturable absorber, fil: spectral filter.

spectral filter with 2.2 nm bandwidth is created by placing a 600 lines/mm grating about 10 cm from the coupling lens of the signal port of the combiner. A half-wave plate in front of the grating maximizes efficiency. A polarization sensitive isolator ensures unidirectional ring propagation. An iris blocks residual cladding light. Non-linear polarization evolution (NPE) is turned into saturable absorption with 3 waveplates and a polarizer. The NPE port is used as a variable output coupler. The zero-order grating reflection is used to monitor the intra-cavity pulse. A dichroic mirror is placed after the output port to separate the signal from the residual pump, and a grating pair compressor is used to dechirp the pulses.

To verify the that similariton pulses are formed in the cavity, we performed split-step Fourier simulations of the non-linear Schrodinger equation [5]. The group velocity dispersion $\beta_2 = 20$ ps^2/km and the non-linear coefficient $\gamma = 0.40$ (W km)$^{-1}$. The small signal gain $g_0 = 30$ dB and the saturation energy $E_{sat} = 60$ nJ. The saturable absorber has a modulation depth $l_0 = 1.0$ and saturation power $P_{sat} = 5$ kW. The gaussian spectral filter has a 2.2 nm full-width at half-maximum (FWHM) bandwidth, the output coupling is 0.70 and a lumped

linear loss of 0.70 accounts for fiber coupling and grating efficiency among others. The gain filter has a 40 nm bandwidth. The results are shown in Figure 6.2. The pulse duration and bandwidth grow continuously in the gain fiber, as expected in self-similar evolution. The saturable absorber has limited effect on the steady-state pulse. The spectral filter shapes the pulse back to a narrowband, nearly transform-limited pulse that seeds the next cycle of self-similar evolution. As is typical of amplifier similariton lasers, spectral breathing by more than a factor of 15 is observed. The output pulse taken after the saturable absorber is a linearly chirped parabola with 60 nJ energy, 33 nm of bandwidth and dechirped duration of 80 fs.
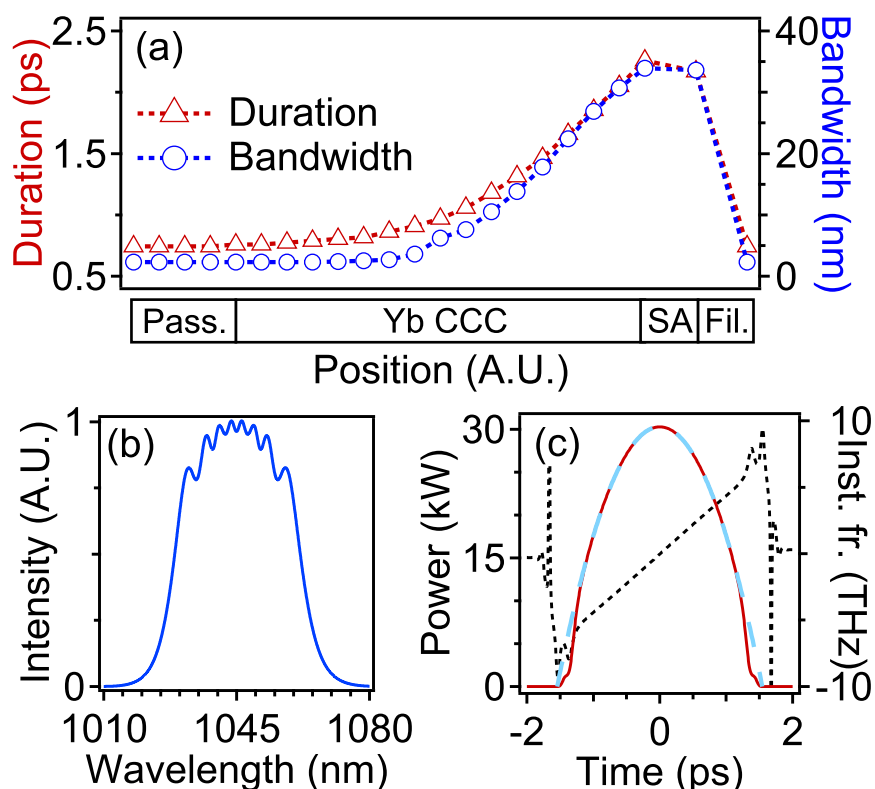

Figure 6.2: Simulated (a) pulse evolution, output pulse (b) spectrum, (c) intensity (solid), parabolic fit (light dashed) and instant frequency (dashed).

6.3 Experiments

Experimentally, the NPE wave-plates are adjusted until mode-locking is observed. A stable self-starting pulse train is obtained at 55 MHz repetition rate. Single-pulsing is checked with a 20 GHz sampling oscilloscope and an autocorrelator with up to 60 ps delay. Figure 6.3 shows mode-locked spectra obtained for absorbed pump powers ranging from 10 W to 20 W. This corresponds to average output powers of 0.44 W up to 3.3 W. The intra-cavity bandwidth increases monotonically with pulse energy from 11 nm to 37 nm, as expected for amplifier similaritons. Some rapid oscillation is visible on top of the NPE output spectrum in Figure 6.3, probably corresponding to spectral interference with a small amount of secondary mode. We suspect this is generated in the combiner, where residual stress may induce mode-mixing and scatter some light in the cladding. The fringe amplitude corresponds to about 0.1% of amplitude in secondary modes, indicating strong mode filtering in the CCC fiber. The RF spectrum shows an instrument limited 80 dB contrast from the noise floor, with a few narrowband 50-70 dB from the main harmonics at the highest powers. This probably indicates the onset of thermal instabilities. Indeed, although transient mode-locking was observed up to 5.5 W, beyond 3.3 W slow thermal instabilities prevent long-term modelocking and cause damage to the combiner and fiber endface.

A self-starting mode-locked state at the maximum stable power is shown in Figure 6.4. The chirped pulse energy is 61 nJ, yielding an average power of 3.3 W. The NPE output spectrum is steep-sided, while the intra-cavity spectrum has a typical similariton laser shape. The output pulse is chirped to 2.2 ps and can be dechirped to 86 fs using a standard grating pair compressor. This is close to the transform-limited duration of 70 fs, confirming the mostly linear chirp typical
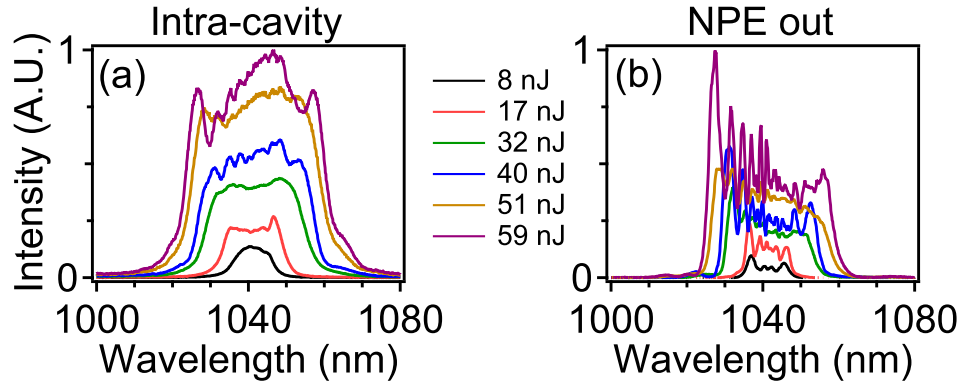
Figure 6.3: Experimental pulse spectrum trends (a) intra-cavity and (b) at the NPE output.

of similariton pulses. The deviation can be due to the limited gain bandwidth, as well the 40-50 nm bandwidth over which the fundamental mode propagates with low-loss in the current CCC design. The dispersion required to dechirp the pulse is -0.05 ps^2, smaller than the total cavity dispersion of -0.07 ps^2. This is typical of amplifier similaritons where the dispersion is accumulated over a single roundtrip [3]. In contrast, dissipative solitons have output dispersions equal or greater than the cavity since the chirp is accumulated over many roundtrips [6]. Effectively single-mode propagation is verified at 3.3 W of output power by the gaussian output beam, M^2 of 1.21 and the absence of secondary pulses above the 30 dB sensitivity of a background-free autocorrelator. The operation is stable for several hours and mode-locked states with similar performance were reproduced over several months.

The current results represent a ten-fold improvement over a single-mode amplifier similariton laser with similar parameters [3]. This is consistent with the scaling of the fiber core size. With a $\geq 70\%$ efficient grating compressor, up to 0.5 MW of peak power could be obtained, twice as much as an amplifier similariton laser with 10 μm diameter single-mode fiber and adaptive pulse shaping. As indicated
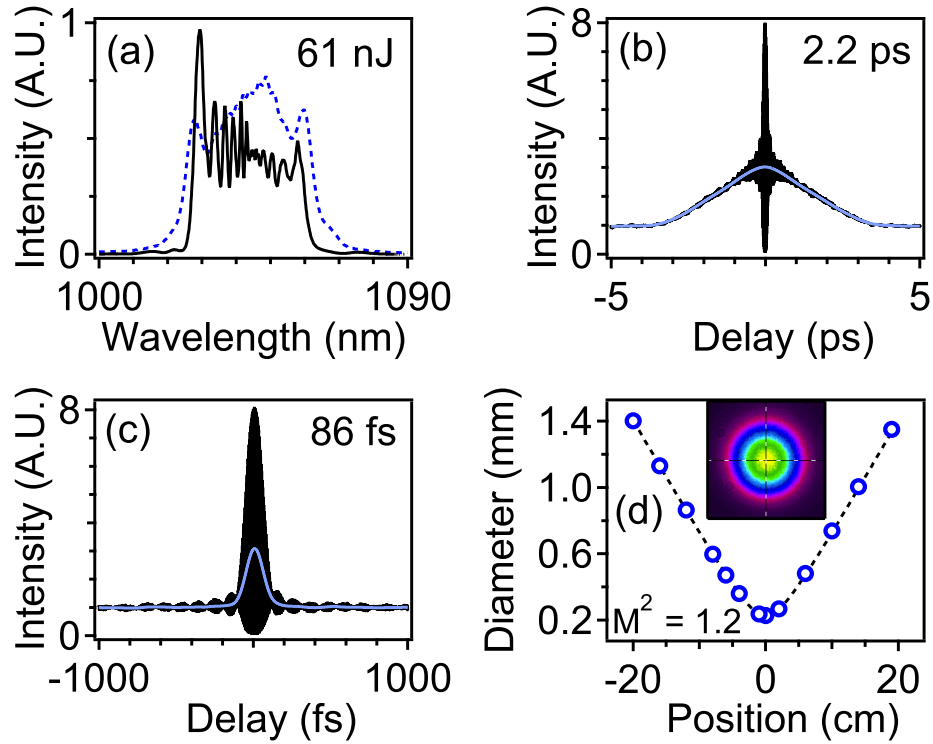
Figure 6.4: Experimental output of CCC similariton laser: (a) NPE output (solid) and intracavity (dashed) spectra, inset beam profile; (b) chirped autocorrelation and (c) dechirped autocorrelation. (d) M^2 measurement and output beam profile (inset $(0.72 \text{ mm})^2$ field).

above, mode-locked states with pulse energies up to 100 nJ and bandwiths supporting dechirped durations approaching 50 fs. Further engineering of the combiner to minimize fiber stress and increase thermal handling capabilities should enable such high energy states to be stabilized, allowing megawatt peak powers to be approached by an integrated and spliceable fiber laser. CCC fiber designs with more broadly-spaced fundamental mode resonances will also be necessary to generate shorter pulses.

6.4 Conclusion

In conclusion, we have demonstrated a high energy amplifier similariton laser based on chirally-coupled core fiber. A fused pump-signal combiner demonstrates the integration potential of CCC fiber. Chirped pulses with energies up to 60 nJ can be dechirped to durations below 90 fs. Numerical simulations confirm self-similar pulse evolution in the cavity. Further energy scaling should be possible with proper engineering of fused components. To our knowledge, this is the highest peak power delivered from a fiber laser with fiber-integrated pump coupling, demonstrating the potential for CCC fiber to enable robust and high performance fiber lasers.

Bibliography

[1] S. Lefrancois, T. S. Sosnowski, C.-H. Liu, A. Galvanauskas, and F. W. Wise, in *CLEO:2012 - Laser Applications to Photonic Applications* (Optical Society of America, Washington, DC, 2012), p. CF1N.6.

[2] A. Chong, W. H. Renninger, and F. W. Wise, Opt. Lett. **33**, 2638 (2008).

[3] W. H. Renninger, A. Chong, and F. W. Wise, Phys. Rev. A **82**, 21805 (2010).

[4] B. Nie, D. Pestov, F. W. Wise, and M. Dantus, Opt. Express **19**, 12074 (2011).

[5] F. O. Ilday, J. R. Buckley, W. G. Clark, and F. W. Wise, Phys. Rev. Lett. **92**, 213902 (2004).

[6] A. Chong, W. H. Renninger, and F. W. Wise, J. Opt. Soc. Am. B **25**, 140 (2008).

CHAPTER 7

SCALING DISSIPATIVE SOLITON FIBER LASERS TO

MEGAWATT PEAK POWERS[1]

In this chapter, we report a dissipative soliton laser based on large-mode-area Yb-doped photonic crystal fiber. Numerical simulations show that such a cavity can support dissipative solitons with energies up to 300 nJ, with dechirped pulse duration less than 100 fs. The measured performances matches theoretical predictions and reaches 12 W of average power at 84 MHz repetition rate, corresponding to 142 nJ pulses, which dechirp to a transform limited duration of 115 fs. Performance is currently limited by the available pump power.

7.1   Introduction

Recently, photonic crystal fibers (PCF) have enabled the production of very large single-mode cores. When this work was initiated, PCF had already been successfully been used to scale up the energy from mode-locked fiber lasers. For example, pulse energies up to 63 nJ with 150 fs dechirped pulses were reached in an ANDi laser [2]. Microstructured rigid rods offer the largest areas and have enabled microjoule energies directly from a single oscillator [3]. However, dechirped pulse duration was limited to hundreds of femtosecond and mode-filtering elements are required due to the lightly multi-mode nature of the rods.

A straightforward scaling of the performance of ANDi lasers reveals that PCF lasers at the time fell short of expected performance. Scaling the performance of a 100 μm^2 effective area ANDi laser [4], we could expect more than 300 nJ in

---

[1]The work presented in this chapter is reported in Optics Letters [1].

sub-100 fs pulses from the $\sim$1000 μm^2 effective area of the PCF. Incidentally, the PCF lasers cited above use an ANDi design, but without a discrete spectral filter. The gain and SESAM bandwidth act as effective 20-40 nm filters in these lasers [2], rather broad for ANDi lasers. The filter is an important pulse shaping element in ANDi lasers, and too broad of a filter restricts the mode-locking range [5]. SESAM are also less flexible saturable absorbers compared to NPE due to their fixed saturation curve, slow responses and susceptibility to thermal damage. Finding a PCF fiber laser design realizing the full scaling potential of dissipative soliton fibers laser was thus an outstanding issue when this project was initiated.

Here we present an ANDi fiber laser based on large-core PCF and delivering up to a megawatt of compressed peak power. The dissipative soliton pulse evolution is modeled and the experimental pulse performance is characterized.

7.2   Design and modeling

The high pump absorption and the difficulty of efficiently splicing or coupling from PCF into other fibers dictate that the cavity be made of only a short length of active fiber. This reduces the total cavity dispersion, implying weaker pulse-shaping by chirped pulse spectral filtering. To determine if such a cavity can support dissipative soliton pulses, numerical simulations were performed with the cavity elements of Figure 7.1. The fiber is 1.25 m long with a net group-velocity dispersion of 0.026 ps^2. The Kerr non-linearity is $\gamma = 0.14$ (W km)$^{-1}$. The small signal gain is 30 dB and the gain saturation energy is $E_{sat} = 67$ nJ. An output coupling of 0.96 is followed by an instantaneous saturable absorber with a modulation depth $l_0 = 0.9$ and saturation power $P_{sat} = 8$ kW. The spectral filter

bandwidth is 12 nm and a gain filter with 40 nm bandwidth is applied.

A stable solution is shown in Figure 7.1, with the output taken after the saturable absorber having 145 nJ energy and a dechirped duration of 90 fs. The simulated pulse evolution is qualitatively similar to that in [5]. This demonstrates that spectrally filtered dissipative solitons are possible in such a cavity despite low non-linearity and dispersion. This is in contrast to [2, 3], where spectral breathing is weak and pulse-shaping is dominated by self-amplitude modulation in a SESAM along with gain filtering. Here, despite the low non-linearity in the PCF, the introduction of a narrow enough spectral filter combined with high pump power provides sufficient pulse shaping to produce self-consistent dissipative solitons. Stable solutions were found for energies up to 160 nJ with a 12 nm spectral filter, and above 300 nJ for a 20 nm filter, both with sub-100 fs dechirped durations.

Following these numerical results, the laser in Figure 7.2 was built. The gain medium is 1.25 m of nominally single-mode Yb-doped large mode-area PCF (Crystal-Fibre DC-170-40-Yb), with a mode-field diameter of 33 μm and effective numerical aperture (NA) $\sim$0.03. An air cladding with a diameter of 170 μm and a NA of $\sim$0.62 at 950 nm guides the pump. The fiber length is chosen to optimize pump absorption. The dispersion of the fiber was estimated to be 0.019 ps^2/m around 1 μm [6]. The output of a fiber-coupled laser diode that provides up to 35 W with a 0.5 nm bandwidth around 976 nm is injected in the cavity using a short-pass dichroic mirror. A polarization sensitive isolator ensures unidirectional ring operation. Spectral filtering is provided by placing a quartz plate in front of the input polarizer of the isolator to create a birefringent filter with 12 nm bandwidth. Non-linear polarization evolution (NPE) in the fiber is converted to amplitude modulation by the waveplates and a polarizing beam splitter. The out-
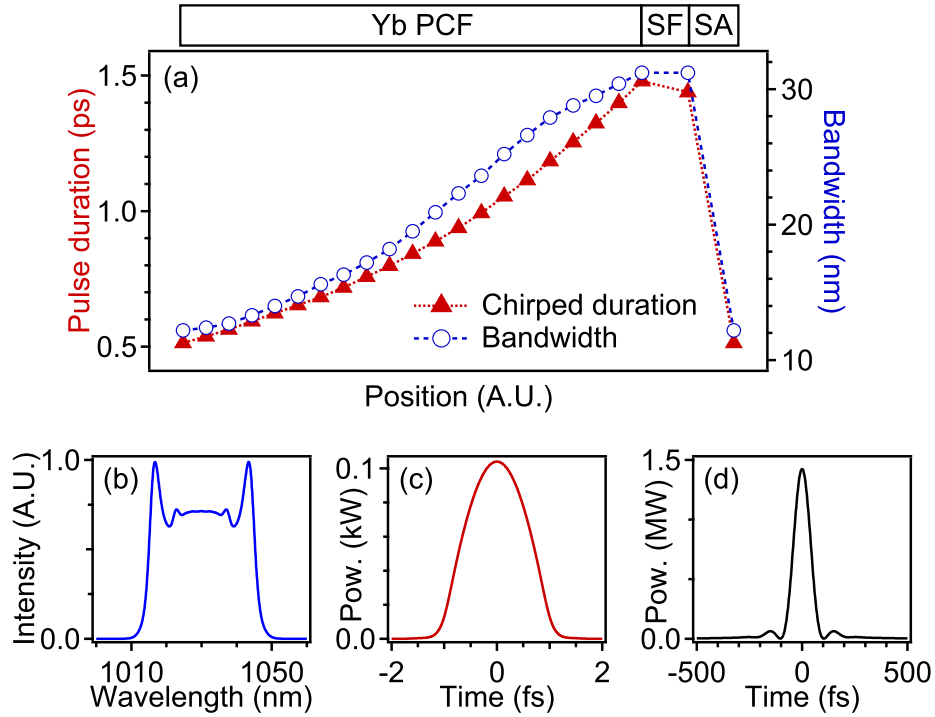
Figure 7.1: (a) Simulated pulse evolution: SF, spectral filter; SA, saturable absorber. Output pulse (b) spectrum, (c) chirped and (d) dechirped time profiles.

put is taken from the NPE port. A grating pair compressor compensates the chirp of the output pulse.

7.3 Experiments

The laser produces stable, self-starting pulse trains, which were monitored using a sampling oscilloscope with 30 ps resolution. Single-pulsing was checked with an autocorrelator with up to 50 ps delay. The spectra in Figure 7.3 correspond to stable experimental modelocked states with neighboring NPE waveplate settings. As output coupling from the NPE port is reduced and intra-cavity energy increased (lower output energy), SPM generates broader bandwidth and deeper modulation
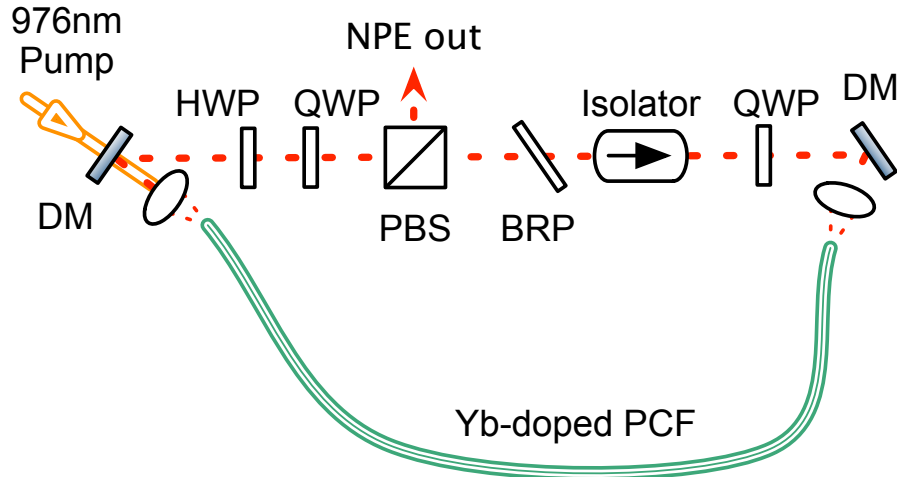
Figure 7.2: Experimental PCF ring laser design: DM, dichroic mirror; HWP and QWP, half and quarter waveplates; PBS, polarizing beamsplitter; BRP, birefringent plate; DDL, dispersive delay line.

at the center of the spectrum. This is the same trend as in [5], consistent with a spectrally filtered dissipative soliton pulse evolution in the cavity. We note small spectral fringes with a period of 2-3 nm, which we suspect are due to spectral interference with a weakly guided second mode. From the modulation depth, we estimate this mode carries less than 1% of the total energy.
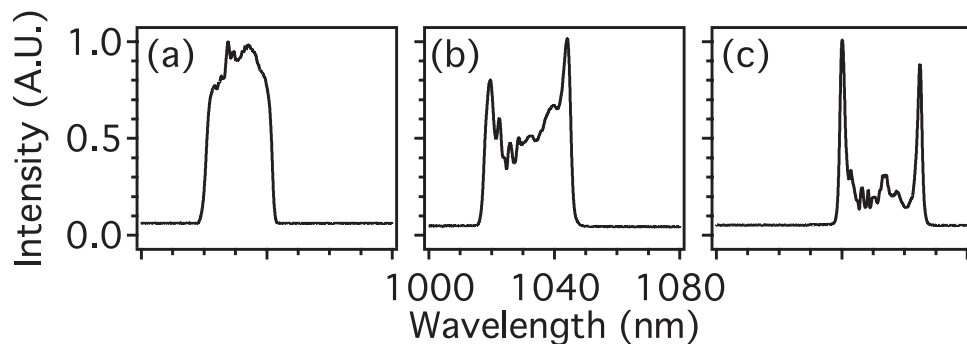
Figure 7.3: Modelocked spectra with output energies (a) 154 nJ, (b) 124 nJ, (c) 52 nJ.

Figure 7.4 shows a high-energy state with a short, clean pulse. With about

24 W of pump light coupled into the cladding, the average output power is 12 W, corresponding to a chirped pulse energy of 142 nJ. After dechirping with a grating pair providing -0.035 ps^2 of dispersion, the interferometric auto-correlation shows a clean pulse nearly identical to the calculated transform limit of the spectrum. From this, we infer a pulse FWHM duration of 115 fs. Assuming a 25% loss from a well-designed grating compressor, this corresponds to a peak power of about 1 MW. The RF spectrum shows good amplitude stability with only small sidebands more than 70 dB down from the first harmonic, at frequencies in the range of gain relaxation oscillations. The dynamic range is limited by the detector/spectrum analyzer combination. Despite minor environmental drifts, modelocking was sustained over many hours.
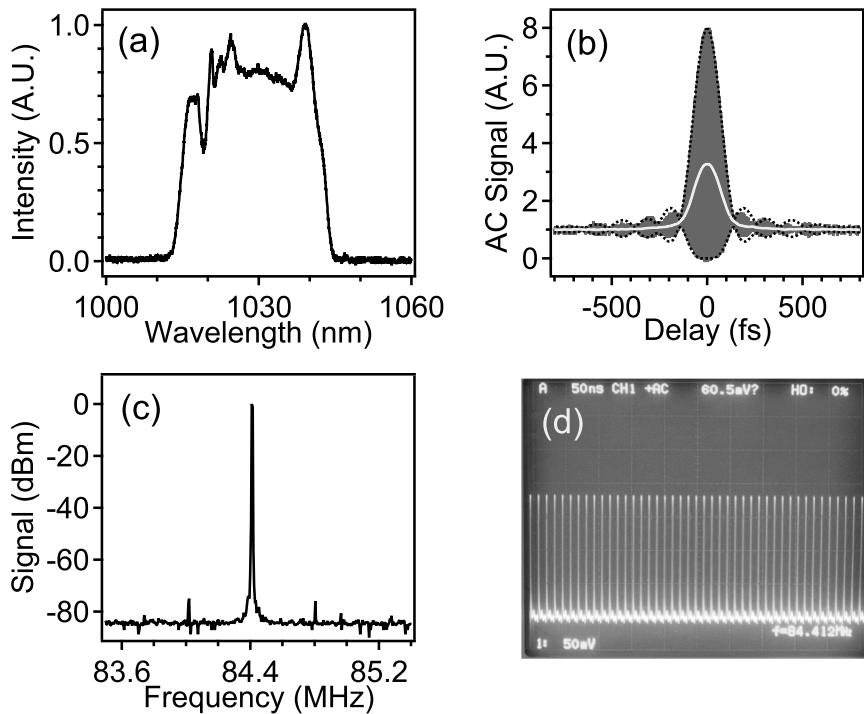

Figure 7.4: Modelocked output: (a) spectrum, (b) dechirped interferometric autocorrelation (gray) and spectrum transform limited envelope (dotted black), (c) RF noise spectrum, 2 MHz span, 1 kHz resolution and (d) pulse train, 50 ns/div and 400 kHz bandwidth.

Pulse energy is expected to scale with mode area at constant nonlinear phase shift. By scaling from [4], 100-fs pulses with energy up to 300 nJ should be possible, in agreement with the numerical simulations. The current laser achieves similar pulse duration to [4] and nearly 5 times higher pulse energy. The energy is currently limited by available pump power. Peak power is comparable to that obtained from the photonic crystal rod laser in [3]; the shorter pulses free from residual phase provided by the present laser compensate for the lower pulse energy. The average and peak powers exceed that of Ti:Sapphire lasers [7] and approach that of state-of-the-art chirped pulse oscillators [8]. At first, fiber endface damage was sometimes observed, presumably due to self-Q-switching in non-modelocked waveplate settings. This can be prevented by careful surface preparation where the microstructure is collapsed at the fiber ends before cleaving. Existing endcap technology [9] can also be used should damage occur again at higher powers.

One of the advantages of fiber gain media is the possibility of integration into compact, robust sources. The laser presented here uses free-space pumping and signal coupling, as well as a PCF gain medium with high bending loss below a radius of 0.5 m. However, recent technological advances have produced similar fibers with bending radii down to 30 cm. Fused pump-signal combiners for airclad PCF have been demonstrated [10], as well as interfacing PCF to single-mode fiber [11]. Integration of the laser design presented here is thus within the reach of current technology.

7.4 Conclusion

In conclusion, we have presented an all-normal dispersion Yb fiber laser based on large-mode area PCF. The laser delivers 12 W at an 84 MHz repetition rate. The 140 nJ pulses can be dechirped extra-cavity to 115 fs. The megawatt peak power that can be reached with this laser matches that of fiber lasers and approaches that of the highest performance solid-state lasers. Numerical simulations confirm dissipative soliton evolution and indicate that pulse energies around 300 nJ are possible given sufficient pump power and endface damage protection, which demonstrates scalability of the ANDi laser concept to the frontier of ultrafast laser performance.

Following this demonstration of a megawatt peak power ANDi laser, several reports have improved on this design and demonstrated record fiber laser performance. By overcoming pump power limitations, more than 300 nJ pulses dechirping down to 75 fs were obtained as expected [12]. Pushing the effective mode area further using newly-developped large-pitch PCF, up to 0.9 μJ pulses dechirping to 90 fs were obtained, corresponding to peak powers are high as 7 MW [13].

Bibliography

[1] S. Lefrançois, K. Kieu, Y. Deng, J. D. Kafka, and F. W. Wise, Opt. Lett. **35**, 1569 (2010).

[2] C. Lecaplain, B. Ortaç, and A. Hideur, Opt. Lett. **34**, 3731 (2009).

[3] B. Ortac, M. Baumgartl, J. Limpert, and A. Tuennermann, Opt. Lett. **34**, 1585 (2009).

[4] K. Kieu, W. H. Renninger, A. Chong, and F. W. Wise, Opt. Lett. **34**, 593 (2009).

[5] A. Chong, W. H. Renninger, and F. W. Wise, J. Opt. Soc. Am. B **25**, 140 (2008).

[6] C. Lecaplain, C. Chedot, A. Hideur, B. Ortac, J. Limpert, C. Chédot, and B. Ortaç, Opt. Lett. **32**, 2738 (2007).

[7] J. D. Kafka, M. L. Watts, and J. Pieterse, IEEE J. Quantum Electron. **28**, 2151 (1992).

[8] A. Fernandez, T. Fuji, A. Poppe, A. Furbach, F. Krausz, and A. Apolonski, Opt. Lett. **29**, 1366 (2004).

[9] C. D. Brooks and F. D. Teodoro, Opt. Express **13**, 8999 (2005).

[10] K. P. Hansen, C. B. Olausson, J. Broeng, D. Noordegraaf, M. D. Maack, T. T. Alkeskjold, M. Laurila, T. Nikolajsen, P. M. W. Skovgaard, M. H. Sorensen, M. Denninger, C. Jakobsen, and H. R. Simonsen, Opt. Eng. **50**, 111609 (2011).

[11] S. G. Leon-Saval, T. A. Birks, N. Y. Joly, A. K. George, W. J. Wadsworth, G. Kakarantzas, and P. S. J. Russell, Opt. Lett. **30**, 1629 (2005).

[12] C. Xie, M.-L. Hu, D.-P. Zhang, C.-L. Gu, Y.-J. Song, L. Chai, and C.-Y. Wang, IEEE Photonic Tech. L. **24**, 551 (2012).

[13] M. Baumgartl, C. Lecaplain, A. Hideur, J. Limpert, and A. Tünnermann, Opt. Lett. **37**, 1640 (2012).

CHAPTER 8

FUTURE DIRECTIONS

8.1   A four-wave mixing fiber-OPO for CARS microscopy

In chapter 2, we showed that four-wave mixing in PCF is an efficient fiber-based frequency conversion mechanism for picosecond pulses. A two-color fiber laser was built to perform CARS microscopy of biological samples. While this optical parametric amplifier (OPA) represents a significant simplification over conventional solid-state sources, it would be useful to simplify the design further. A natural next step would be to place the PCF in a cavity to form an optical parametric oscillator (OPO). A separately tuned seed laser would no longer be necessary. We can also expect noise to be lower due to the self-consistent nature of oscillators.

OPOs based on FWM in fiber have been demonstrated. Much work has been done on PCF OPOs [1], and multimodal CARS and multiphoton microscopy is possible with such devices [2]. However, most of the work so far has focused on either femtosecond and tens of picosecond or longer pulses. For femtosecond pulses, seeding in or near the anomalous dispersion region allows self-seeding by SPM spectral broadening and minimizes pulse walk-off. However, this is unsuitable for picosecond CARS due to the large FWM gain bandwidth and small frequency shift. Introducing a spectral filter can reduce the output bandwidth, but the frequency shift is still no greater than 1100 cm^{-1} [3].

Based on the FWM design described in chapter 2, we will study the possibility of combining normal dispersion FWM with high peak power few-picosecond pulses to produce a fiber-OPO for CARS microscopy.

Modeling and design

The GNLSE model used in chapter 2.3 can be applied to an OPO system. The pump pulses and shot noise are injected into the PCF segment. The FWM signal and idler pulses initially grow from noise. At each roundtrip, the idler field is fedback with a given feedback ratio accounting for roundtrip losses, and a delay is applied to ensure synchronization between the pump and fed back pulses. The simulation loops until the idler energy is stabilized.

Figure 8.1 shows the evolution of the output signal of a fiber-OPO over 50 roundtrips. The OPO is composed of 21 cm of Bath 050803B PCF. The input pump pulses have 2.15 kW peak power (17 nJ) and 7.5 ps duration (0.23 nm bandwidth) with a center wavelength of 1035 nm. At this wavelength, the dispersion coefficients used are $\beta_2 = 21.1\,\text{fs}^2/\text{mm}$, $\beta_3 = 40.9\,\text{fs}^3/\text{mm}$, $\beta_4 = -43.0\,\text{fs}^4/\text{mm}$, $\beta_5 = 168\,\text{fs}^5/\text{mm}$ and $\beta_6 = -799\,\text{fs}^6/\text{mm}$. After each roundtrip, a 1300 nm long-pass filter is applied to feedback the idler with a 5% transmission. A delay of -1.8 ps is applied to compensate GVM and synchronize with the next pump pulse.
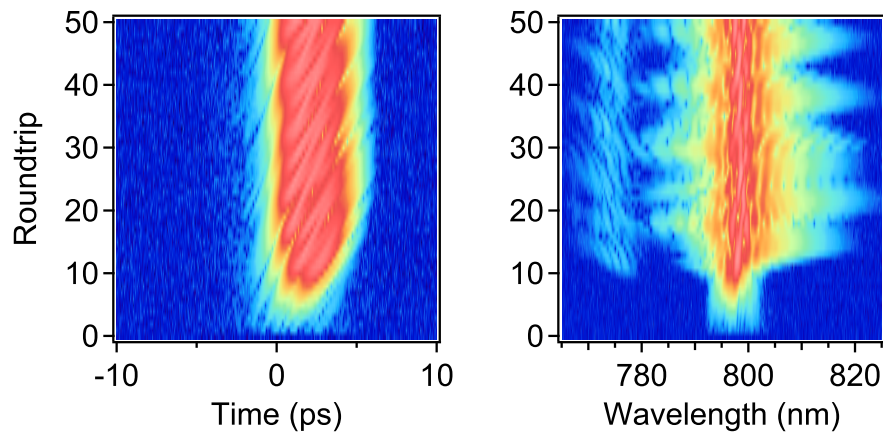

Figure 8.1: Evolution of the output signal from a free-running FWM fiber-OPO. Color scale is logarithmic.

Although signal and idler pulses are efficiently generated, the free-running OPO does not converge to a stable state and the output bandwidth is several nanometers. However, an oscillatory pattern is clearly visible within the complex shape of the signal. This is probably due to cascaded interactions between the pump and generated sidebands. This could be due to complex non-linear dynamics such as limit cycle behavior. Although this is interesting from a fundamental science perspective, it is not suitable as a stable laser source.

The complex evolution of the free-running OPO leads to energy flowing between the phase-matched central spectral peak and secondary peaks. A narrow spectral filter could stabilize the OPO by suppressing the growth of the secondary peaks. Figure 8.2 shows the evolution of an OPO with a 2 nm gaussian filter centered at 1468 nm introduced before the idler feedback. The OPO output converges to within $1:10^2$ in less than 50 roundtrips.
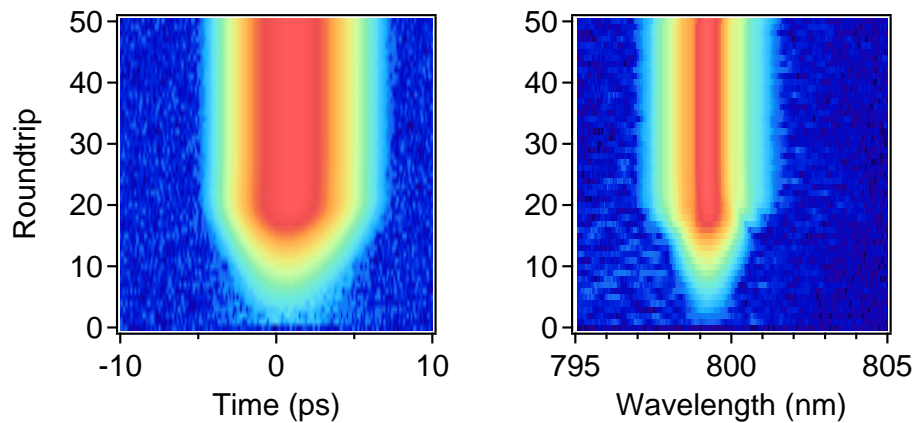

Figure 8.2: Evolution of the output signal from a FWM fiber-OPO with a stabilizing spectral filter. Color scale is logarithmic.

OPO signal output trends are shown in Figure 8.3. The OPO delivers high performance for a delay range of 0.8 ps. The signal does not grow significantly outside this range. The signal peak power grows roughly linearly with the pump

peak power, with saturation setting in around 3 kW. A saturation of the output peak power occurs for feedback efficiencies beyond 5%. The oscillator converges to a stable solution for filter bandwidths between 1 nm to 8 nm. For bandwidth lower than 1 nm the signal is suppressed, while for bandwidths higher than 3 nm the output spectrum becomes broader and structured until the OPO is no longer stable past 8 nm. Finally, if the input pulses are chirped, the output peak power declines for chirped bandwidths larger than 1 nm.
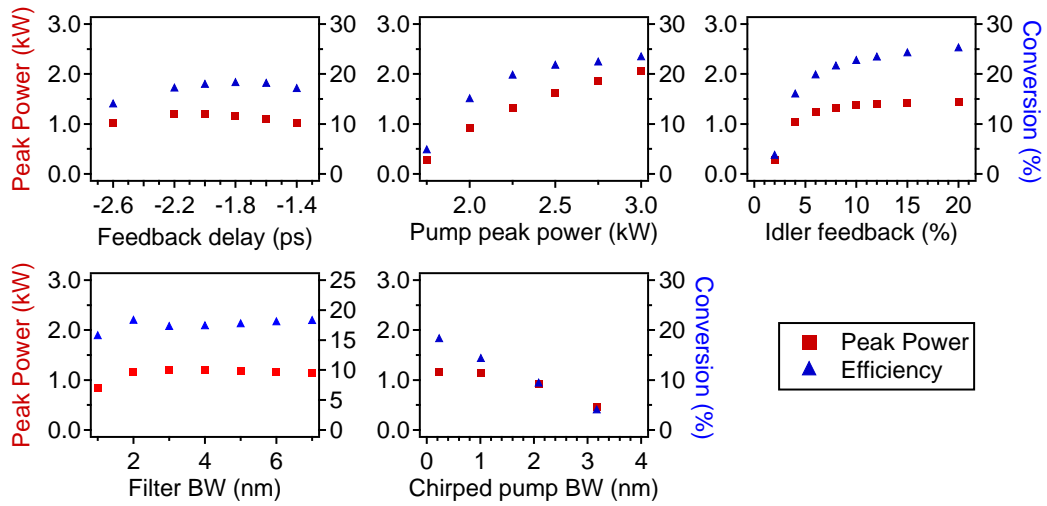

Figure 8.3: Fiber-OPO output signal trends.

Based on the results above, a complete FWM fiber-OPO design is presented in Figure 8.4. In order to synchronize to the 54 MHz repetition rate of the pump fiber laser, 3.5 m of fiber with 8.2 μm core diameter and 0.14 NA is added. The spectral filter has again 2 nm bandwidth around 1468 nm, and the feedback delay is 10.2 ps. For the pump parameters above, the output signal pulses have 3.0 nJ of pulse energy corresponding to 18% conversion, 0.46 nm bandwidth and 2.5 ps duration. The pulse energy is stable within $1:10^4$ over more than 1000 roundtrips. The idler pulses are practically unaffected in the fiber feedback segment given the dispersion and non-linear lengths $L_D \approx 150$ m and $L_{NL} \approx 21$ m.
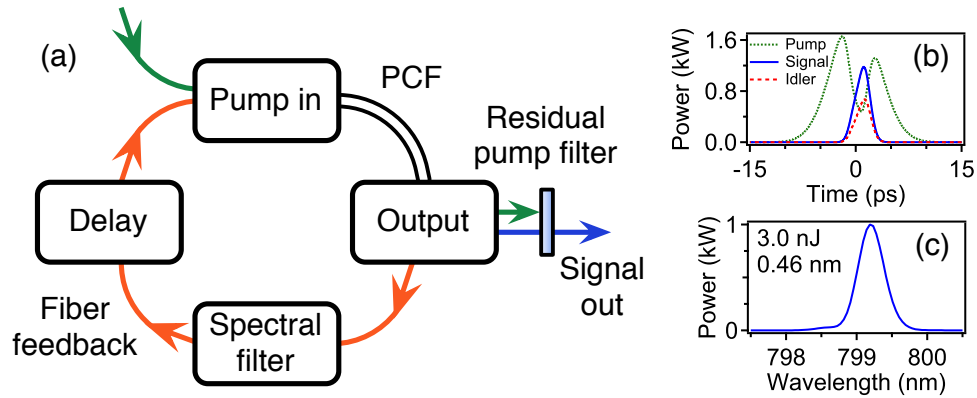
Figure 8.4: (a) Proposed design for a picosecond FWM fiber-OPO. Converged output (b) pulses and (c) signal spectrum.

Preliminary experiments

The fiber-OPO design is implemented experimentally with the setup in Figure 8.5. The pump pulses are provided by the fiber laser and divided pulse amplifier used previously. The pump is coupled in and the signal is extracted using dichroic mirrors. A filter with about 2 nm bandwidth is created by placing a 600 ln/mm grating 10 cm before the idler feedback collimator. A fiber delay line with up to 80 ps delay ensures synchronization. A fiber polarization controller matches the idler polarization to the pump. The PCF length is 30 cm, the feedback fiber is about 330 cm long and the free-space sections comprise about 36 cm of total length. Using a CW laser, the idler feedback is estimated to be 2-4%.

Preliminary experiments were performed with the grating replaced by a mirror. This helps align the cavity and synchronize the delay without having to simultaneously tune the filter to the still uncertain idler wavelength. Figure 8.6 shows the unfiltered OPO output after delay synchronization. With 29 nJ of pump pulse energy in the PCF, more than 5 nJ of signal can be generated. The signal bandwidth
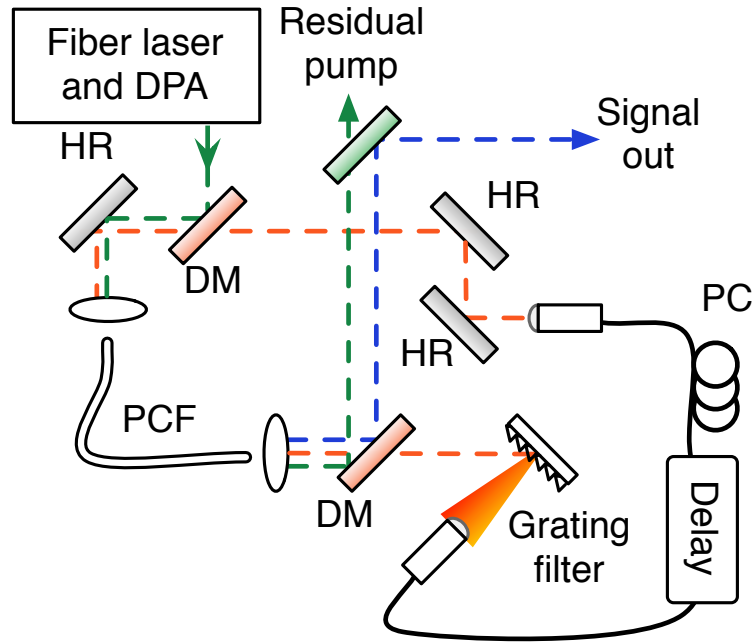
Figure 8.5: Experimental setup for FWM fiber-OPO. HR: mirror, DM: dichroic mirror, PC: polarization controller.

is about 13 nm, consistent with the typical bandwidth from the oscillating output simulated in Figure 8.1. If the feedback is blocked, spontaneous FWM produces a signal with about 1 nJ pulse energy and bandwidth of about 4 nm. The corresponding spontaneous idler also exhibits a broad spectrum and is centered around 1470-1480 nm, in good agreement with simulations.
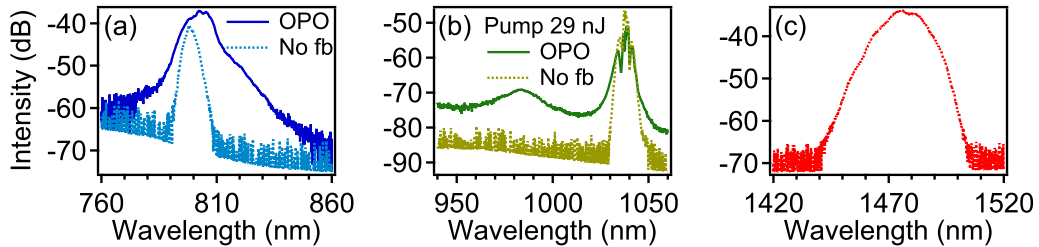

Figure 8.6: Experimental results for FWM fiber-OPO without spectral filtering. Output spectra for OPO (solid) and single-pass (dotted) for (a) signal, (b) residual pump and (c) spontaneous idler.

Preliminary noise measurements of the filter-less OPO shown in Figure 8.7 indicate a signal RIN of about -90 dBm/Hz, 20 dBm higher than the FWM OPA. This is expected given the oscillatory behavior seen in simulations.
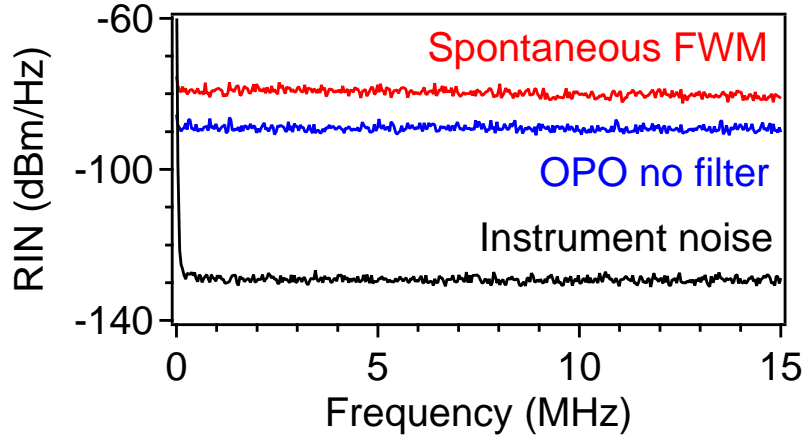

Figure 8.7: Relative intensity noise of the unfiltered fiber-OPO signal pulse train.

The next step will be to introduce the spectral filter inside the cavity and obtain the stable narrow-band operation predicted in simulations. Given the good agreement between filter-less OPO experiments and simulations, the stabilized fiber-OPO has good chances of success. Further integration of the OPO cavity will also be pursued. A 1035/1470 nm high power WDM has already been obtained (Gooch and Housego, United Kingdom). The non-linear length of the pump pulses is on the order of 10 cm in 1030 nm singlemode fiber. Figure 8.3 indicates spectral broadening of up to a factor of 4 is tolerable, so SPM in the pump pigtails should be manageable.

8.2 Femtosecond four-wave mixing frequency conversion

This report focuses on simulations of four-wave mixing in PCF for tunable femtosecond pulse conversion. Four-wave mixing presents two different regimes depending on the sign of the dispersion. At normal dispersion, higher-order dispersion generates widely spaced and narrow sidebands. This is most suitable for picosecond frequency conversion. In the anomalous dispersion regime, modulation instability gives rise to broad solitonic sidebands. This is suitable for femtosecond pulses. Also, the anomalous dispersion regime is more sensitive to input peak power, since it is dominated by the balance of SPM and GVD. Figure 1 shows the phase-matching diagram for a commercial NL1040 PCF from NKT Photonics. Its zero-dispersion wavelength is around 1040 nm.
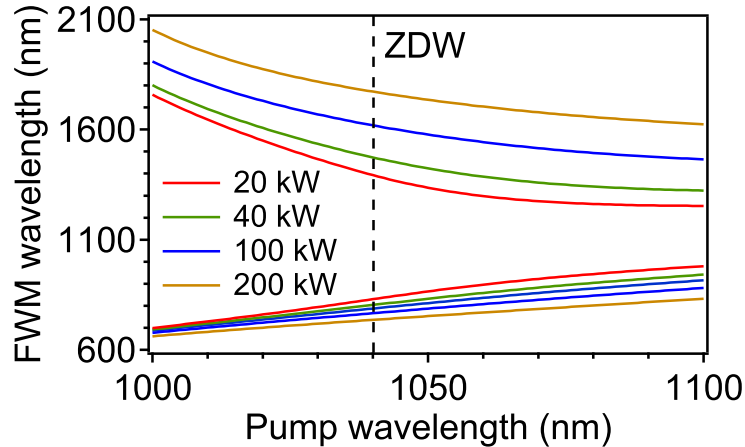
Figure 8.8: FWM phase-matching for NL1040 PCF.

We first investigate seeded femtosecond pulse conversion in a PCF optimized for normal-dispersion FWM. Figure 8.9 shows the evolution of a 100 fs pulse with 40 kW input peak power, centered at 1036 nm. The expected FWM sideband is around 775 nm. Although this sideband initially grows, it never contains significant energy, despite a strong 1 W seed at the idler wavelength. Eventually,

SPM broadens the pump pulse down to 800 nm and a peak is generated around 945 nm. This is probably due to FWM on the anomalous dispersion side from the broadened pump pulse.
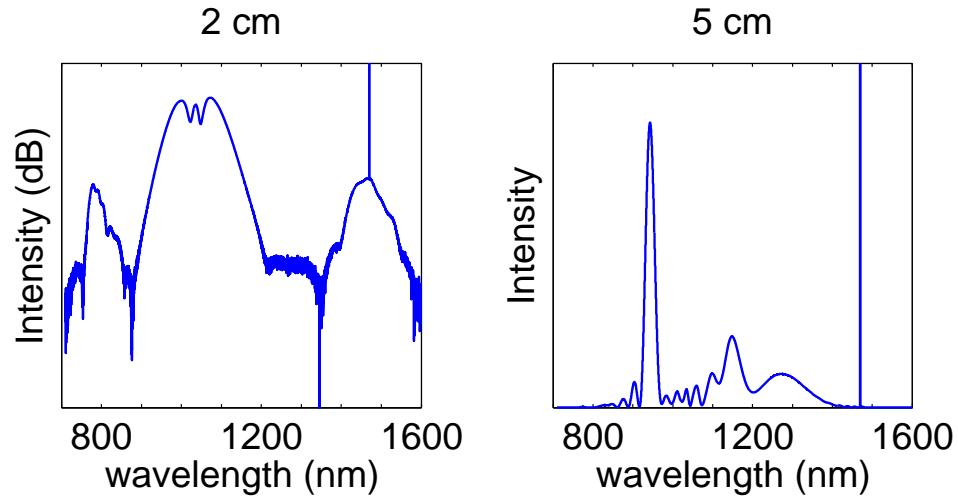

Figure 8.9: Simulated FWM in a normal-dispersion Bath PCF with ZDW 1051 nm.

Thus, pumping in the anomalous dispersion regime or close to the zero-dispersion wavelength seems most appropriate for femtosecond pulses. This is due to rapid pulse walk-off in the femtosecond regime, prohibiting the widely spaced frequency conversion possible with picosecond pulses. Also, self-seeding occurs due to large SPM broadening of the spectrum extending all the way to the FWM wavelengths. This regime has been exploited in fiber-FWM OPAs and OPOs [4, 5, 6].

A highly non-linear PCF should be most optimal for self-seeded femtosecond FWM. Figure 8.10 details the frequency conversion of 1030 nm pulses in NKT NL1040 PCF. Since the SPM seeds the process, the blue-shifted signal is on the trailing side while the idler is on the leading edge. A broad red-shifted feature is also visible, probably a Raman soliton that breaks off from the part of the spectrum on the anomalous dispersion side.

Figure 8.11 details FWM trends for NL1040 PCF at different peak powers. This
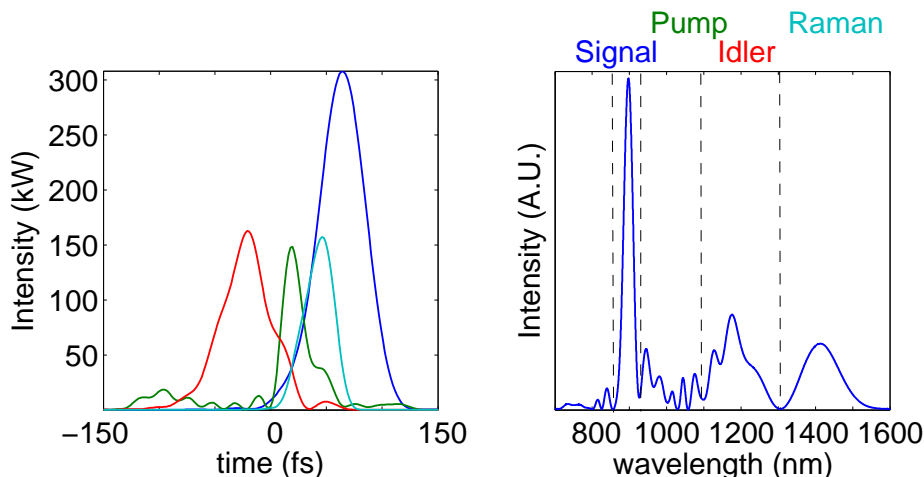
Figure 8.10: Simulations of self-seeded FWM in NL1040 PCF after 3.3 cm propagation of a 40 kW peak power pulse.

is the main mechanism to tune the generated wavelengths in self-seeded FWM. With increasing peak powers, signals from 940 nm to 840 nm can be generated with greater than 40% conversion efficiency. The signal pulses are shorter than 70 fs without external compression.

A preliminary experimental test of femtosecond FWM is shown in Figure 8.12. The input pulses are centered around 1047 nm and are dechirped to 90 fs. The energy in the fiber is 6 nJ, corresponding to about 60 kW peak power. 5 cm of NL1040 PCF from NKT Photonics is used. The signal wavelength is around 920 nm, roughly fitting the 40 kW simulation result. This could be due to secondary pulse features reducing the actual peak power, as well as uncertainties in the experimental fiber and pulse parameters. Signal conversion is about 28%. The idler pulse spectrum around 1150 nm is highly structured, but the Raman soliton around 1300 nm is rather smooth. This first result indicates the experimental process could approach simulated performance given some optimization.

Although this report simulates FWM with peak powers up to 200 kW, it should
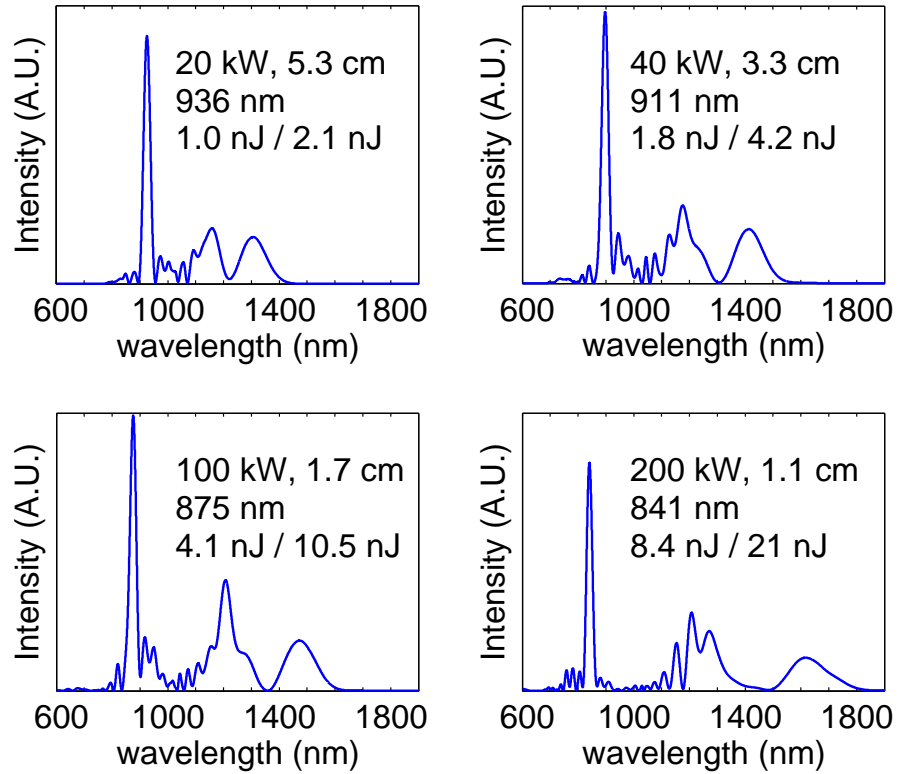
Figure 8.11: Simulated FWM trends in NL1040 PCF. Centers signal wavelength and pulse energy over total pulse energy is shown.
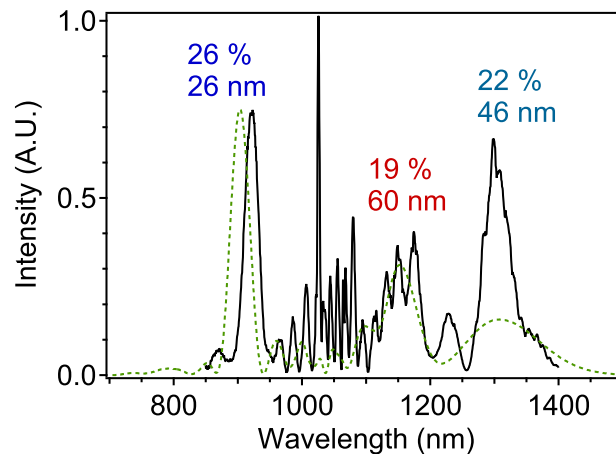

Figure 8.12: Experimental (solid line) FWM in 5 cm of NL1040 PCF with 90 fs, 60 kW pulse, compared to simulation for 40 kW peak power after 2.5 cm (dashed line). Data courtesy of Peng Li.

be possible to obtain wavelength shorter than 875 nm with higher input powers. However, it is difficult to simulate this reliably with the current split-step Fourier integration of the slowly-varying envelope approximation. Indeed, the envelope model creates a spectrum symmetric around the carrier. Thus, any frequency higher than twice the carrier corresponds to negative frequencies on the low side. This limits the current 1030 nm carrier simulations to wavelengths no smaller than 515 nm. When simulating femtosecond FWM, this generates artifacts at the spectral edge which interfere with the physical pulse. This can be seen in Figure 8.13 as resolution limited modulation in the time domain and peaks at the edge of the spectral window. To simulate larger frequency shifts, numerical methods accounting for the full electric field will have to be used to account for carrier-level effects.
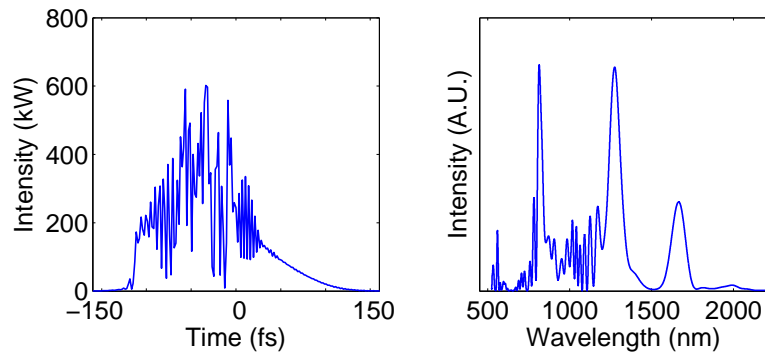
Figure 8.13: Simulated FWM with 400 kW pulses, showing numerical limits of the SSF method.

In conclusion, femtosecond FWM in PCF is possible when pumping near the zero-dispersion wavelength. Self-seeding is achieved due to large SPM spectral broadening. Limited tunability is possible by changing the input peak powers. The maximum tuning range should go down to around 800 nm with typical sources and fibers. Preliminary experiments show conversion down to 920 nm and up to 1300 nm with 20-30% conversion are possible. Simulating larger frequency shifts

127

will require numerical methods beyond the slowly-varying envelope approximation.

8.3 Gain scaling of similariton fiber lasers

Here I summarize results from simulations scaling amplifier similariton lasers to large energies. A first step was to use chirally-coupled core fiber. Besides energy scaling with larger fiber cores, we can optimize the pulses evolution to maximize energy. The parabolic similariton of the NLSE with gain is an asymptotic solution that is fully defined by three parameters: pulse width T_p, spectral bandwidth ω_p and peak power P_0 [7]. These in turn depend on the fiber parameters: GVD β_2, non-linearity γ and gain per unit length g. We can obtain an expression for the output pulse energy E_g at a given ω_p:

$$E_g = \frac{3\omega_p^3 \beta_2^2}{\gamma g}. \tag{8.1}$$

Thus, using longer fibers with lower unit gain should yield higher pulse energies before the gain bandwidth distorts the similariton evolution. Figure 8.14 shows the simulated output spectrum for a CCC oscillator with a constant 30 dB net small-signal gain and a 2 nm gaussian filter. The seed pulse is gaussian to emphasize the general trend. The RMS bandwidth is kept constant at 24 nm.

After about 10 m of gain fiber, the spectrum stabilizes into a mostly parabolic shape. Pulse energy then increases linearly with gain fiber length. The time domain pulses are parabolic and their chirped duration also increases linearly. The peak power of the pulses remains constant, so that the extra energy is stored in the longer durations resulting from the larger net dispersion of the gain fiber.

Simulations no longer converge after 45 m of gain fiber. This is probably due to the uncompensated dispersion of the pulse fed back into the gain fiber. This puts the input pulse further from the asymptotic solution and weakens the similariton attractor.
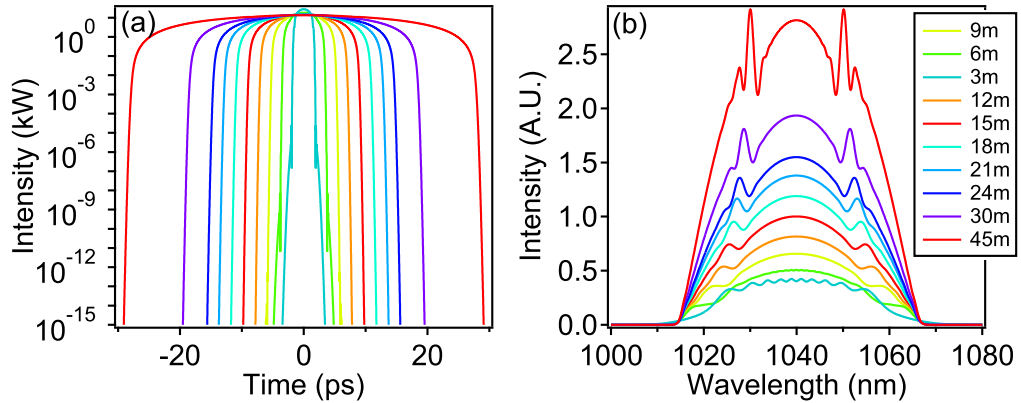

Figure 8.14: Simulations of an all-normal similariton oscillator with decreasing gain per length.

To further study energy scaling, dispersion compensation is added after the output coupler. Three quarters of the total cavity dispersion is compensated. As expected, the output spectra show a cleaner parabolic spectra and simulations converge for longer gain fibers. This is shown in 8.15. Simulations are stopped at 150 m for practical considerations.

We now look at trends in energy and pulse durations in Figure. 8.16(a). As pointed out above, after 10 m of gain fiber, the similariton energy and duration grow linearly with gain fiber length. This is in agreement with Equation 8.1. For an all-normal cavity, up to 300 nJ can be obtained for a gain fiber length of 45 m. For the DM cavity energies above one uJ are obtained.

However, the compressed pulse quality degrades for longer fibers. Figure 8.16(b) shows that the dechirped pulse duration increases beyond 150 fs, and
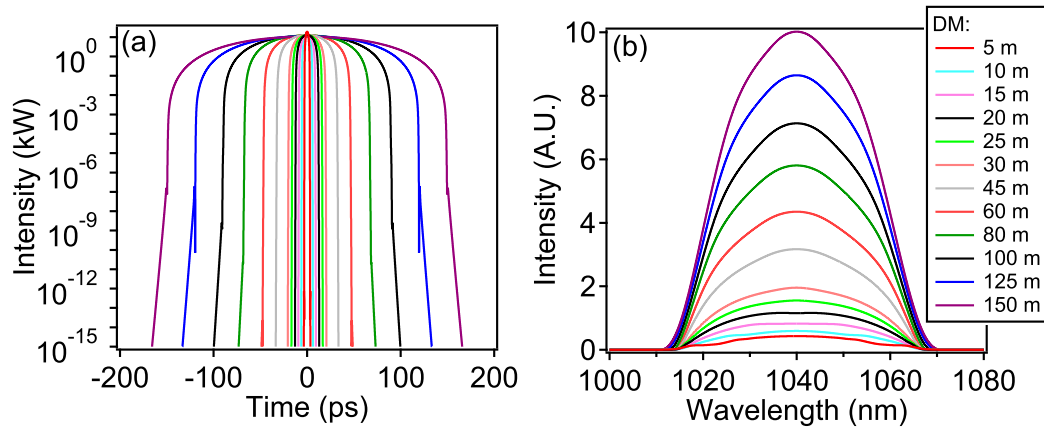
Figure 8.15: Simulations of a dispersion-managed similariton oscillator with decreasing gain per length.
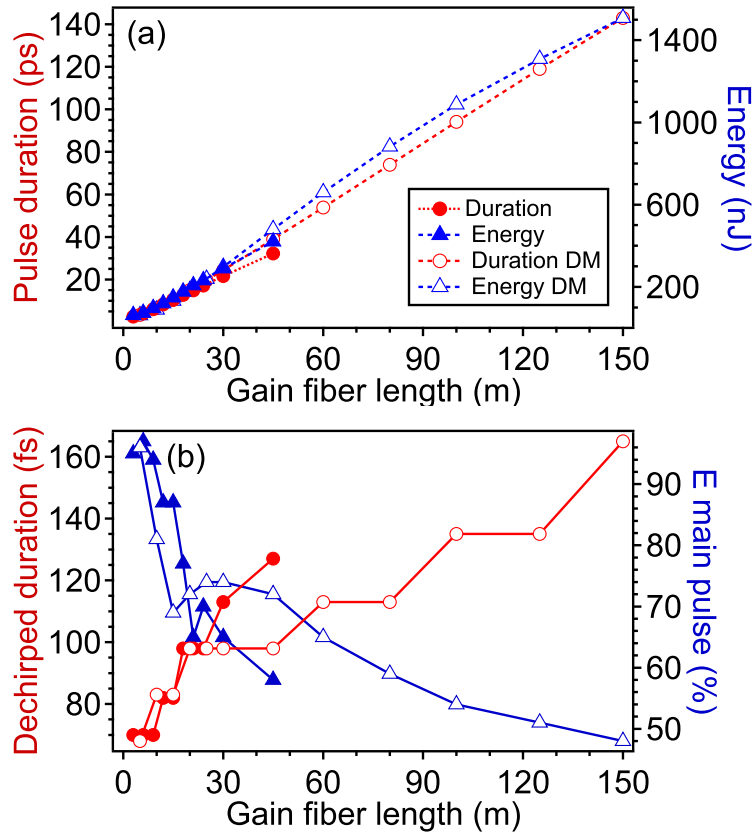
Figure 8.16: Modeled trends for gain scaling similariton oscillators: (a) chirped pulse properties and (b) dechirped pulse quality.

the percentage of energy in the main pulse drops below 70 % for fiber lengths larger than 25 m. A few picosecond pedestal develops on the dechirped pulses. Figure 8.17 demonstrates this for the all-normal case. This is similar to what happens in CPA systems with uncompensated SPM. Indeed, this pedestal is typical of SPM accumulation on highly chirped pulses [8].
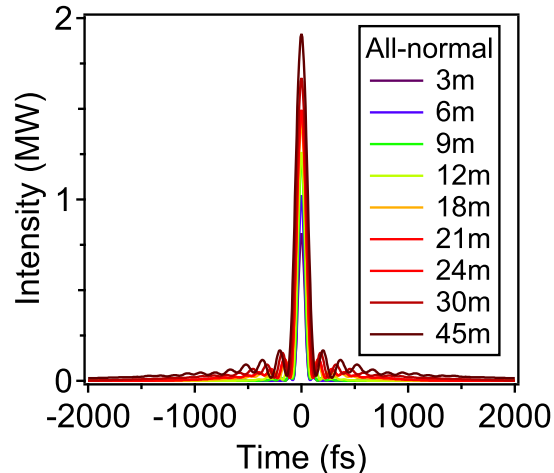

Figure 8.17: Dechirped pulse trends modeled for a gain-scaled all-normal similariton.

This places an upper limit on the ideal gain fiber length for optimal similariton performance. Figure 8.18 shows the scaling of the compressed peak power. There is an inflection point around 40 m of gain fiber. After this, the pedestal takes away a significant amount of pulse energy, and the peak power saturates past 4 MW of peak power. Depending on whether an application requires clean short pulses or merely peak power, the optimal fiber length should lie between 10 m to 40 m of gain fiber.

These simulations are preliminary and represent the best-case systems. Self-starting and stability must be assessed. Some insight could be gleaned from simulations starting from noise, but the real test will be experimental. Current CCC fibers have pump absorptions of about 5 dB/m at 976 nm and could be extended
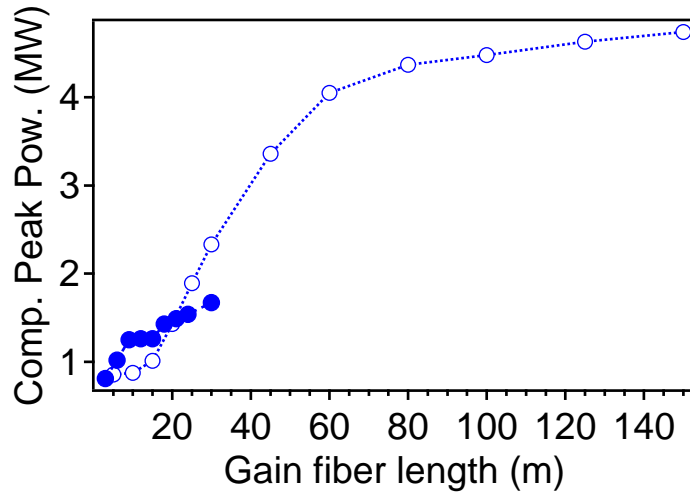
Figure 8.18: Compressed peak power modeled for gain-scaled similaritons.

to about 10 m. Pumping at 915 nm would lower absorption and could allow longer lengths. This also lowers inversion and increases the gain bandwidth of Yb to around 60 nm. Bismuth fiber currently has very low absorption and typically requires around 30 m of gain fiber. This is detrimental to most pulse evolutions but could prove advantageous for similaritons.

In conclusion, simulations indicate that scaling to high energies and peak powers should be possible by lowering the gain per length of CCC similariton lasers. Pulse energies close to 300 nJ and peak powers above 1 MW should be obtained with around 10-15 m of realistic gain fiber. Scaling up to 1 uJ seems possible for very long fibers, but pulse quality degrades and it is unsure if a suitable gain fiber can be found.

8.4 Pulse compression of normal-dispersion fiber lasers

We numerically study the temporal compression of ultrashort pulses generated from normal dispersion fiber lasers. Spectral broadening is provided by self-phase modulation (SPM) in a normal-dispersion photonic crystal fiber (PCF). We consider the case of a dissipative soliton all-normal dispersion (ANDi) laser and an amplifier similariton laser. The influence of the input chirp on the compressed pulses is systematically studied.

Input pulses are generated by simulating mode-locked oscillators with parameters typical for double-clad single-mode systems at 1 μm. The ANDi fiber set contains 50 cm of passive fiber, 1.5 m of gain fiber and another 30 cm of passive fiber. A 15 nm FWHM gaussian filter provides pulse shaping. The amplifier similariton laser contains 20 cm of passive fiber, 2 m of gain fiber and another 30 cm of passive fiber. In both cases, the gain saturation energy is ramped up until the output pulse supports a 100 fs FWHM transform-limited pulse. The input pulses are shown in Figure 8.19. To study the influence of chirp, the input pulses are passed through variable amounts of negative group velocity dispersion (GVD) to obtain shorter pulses.

Pulse compression is carried out in an all-normal dispersion PCF. The fiber is engineered to have a low and constant GVD from 900 nm to 1200 nm [9]. We use a GVD $\beta_2 = 3.4$ fs^2/mm and an effective area of 8 μm^2. Given the flat GVD profile, we neglect third-order dispersion.

The model uses the extended non-linear Schrödinger equation Eqn.1.15. This accounts for shock-formation and Raman scattering to accurately model short pulses. Spontaneous Raman noise and shot noise were included, but they had no
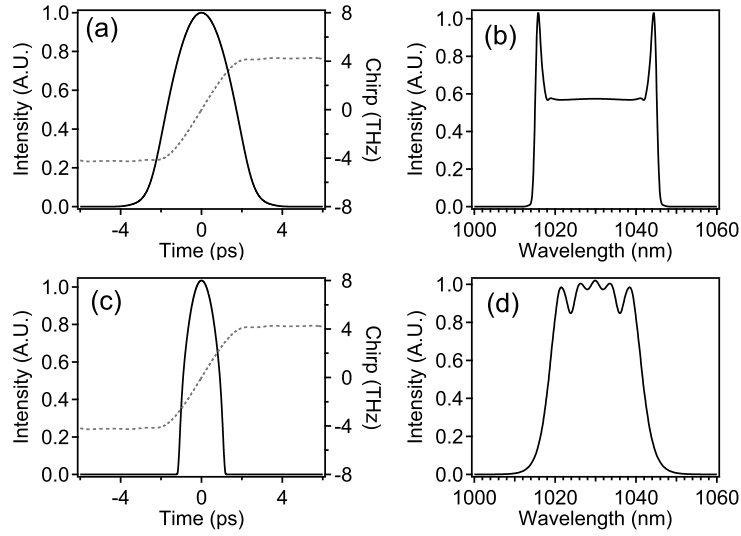
Figure 8.19: Simulated pulse (solid), chirp (dashed) and spectrum from double-clad ANDi laser (a)-(b) and amplifier similariton laser (c)-(d).

significant effect in this regime.

The input pulses with different chirps are propagated through 60 cm of PCF. The input pulse energy is chosen so that the RMS spectral bandwidth grows to 100 nm, supporting a 14-18 fs transform-limited pulse. For the fully compressed input pulses, we also study compression in 10 cm of PCF. This is done to avoid the wave-breaking which occurs for longer fibers due to the increasing effect of dispersion on these compressed pulses.

The compressed spectra from the ANDi laser are shown in Figure 8.20. For chirped pulses with duration of 1 ps or more, the spectra show signature of SPM broadening. However, the effect of chirp is visible in the decrease spectral fringe period with increasing chirp. This is likely due to rapidly varying phase across the pulse due to chirp. A flat central section is also visible, with a width comparable to the original spectrum. For ANDi pulses compressed to 300 fs, strong features develop around the original ANDi sidepeaks. This effect is stronger in the 100 fs

134

pulse, indicating This is similar to the experimental trend seen in the compression of a Ti:sapphire chirped-pulse oscillator [10]. When propagating through a shorter 10 cm of fiber, the 100 fs still shows amplified sidepeaks, but the overall spectral shape appears simpler under the lower dispersion.
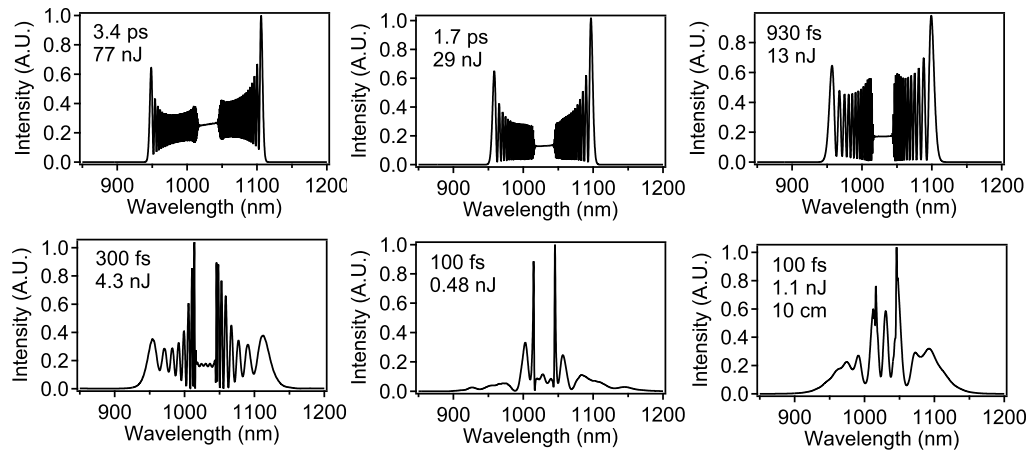

Figure 8.20: Compressed pulse spectra from an ANDi laser.

The results for the amplifier similariton pulses are shown in Figure 8.21. For the fully chirped pulse with 1.8 ps duration, parabolic compression occurs and the spectrum is quite smooth. At 900 fs, a complex spectrum is formed, probably through a mechanism intermediate between parabolic and pure SPM compression. Shorter pulses appear to compress mostly through SPM.

As a control, we first simulate the compression of a transform-limited gaussian pulse with 100 fs duration, as shown in Figure 8.22. For the 60 cm propagation, the pulse evolves towards a parabolic shape due to the balance of dispersion and SPM. For 10 cm of fiber, dispersion is very small and the compressed pulse spectrum has the typical SPM shape.

The pulses output from the PCF are compressed to their optimal peak power using pure negative GVD. The results for both the ANDi laser and the amplifier
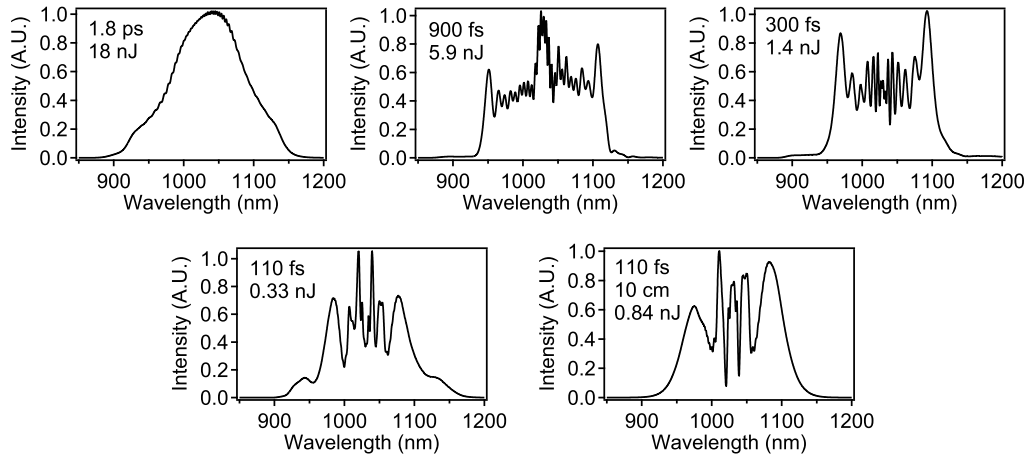
Figure 8.21: Compressed pulse spectra from an amplifier similariton laser.
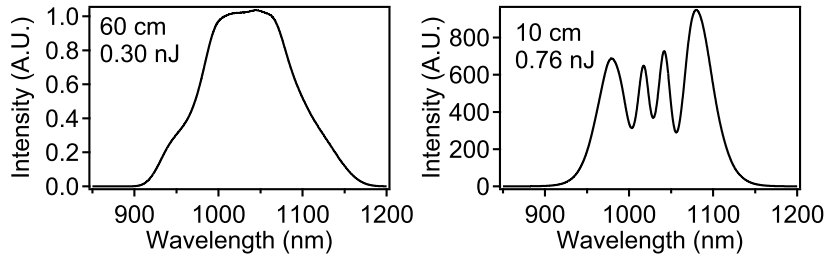
Figure 8.22: Compressed pulse spectra from transform-limited gaussian input.

similariton are shown in Figure 8.23. In both cases, the pulses generated by chirped inputs are longer and then to show a low but wide pedestal. This is typical of the residual phase imparted by SPM on chirped pulses [8]. Although lower initial chirp generates more structured spectra, the compressed pulses are shorter and have shorter pedestals. For the ANDi pulses, the optimal pulse in terms of duration and structure occurs for a input stretching of 3x, with additional structure forming for shorter inputs. For the parabolic pulses, the intermediate chirp regime shows more structure. However, for the 100 fs pulses, the parabolic spectrum generates a cleaner pulses with less secondary structure than the ANDi pulse.

As a control, the compressed pulses from a gaussian input are shown in Figure 8.24. For both 10 cm and 60 cm propagation, good quality pulses close to the
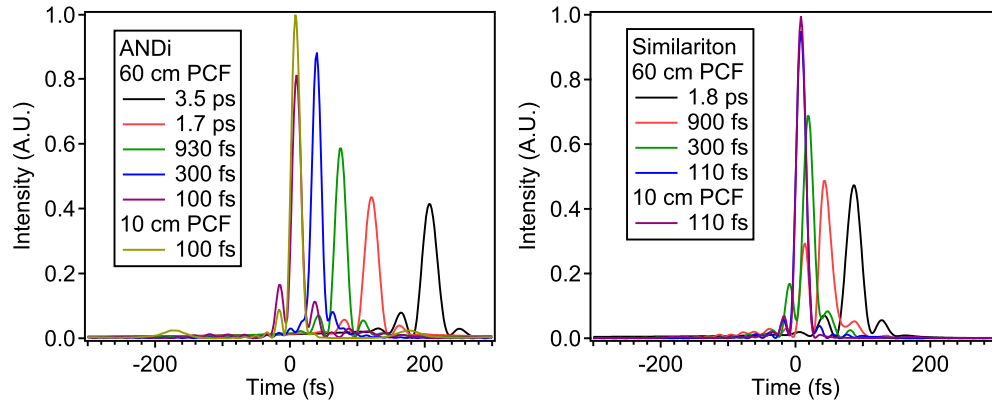
Figure 8.23: Compressed temporal profiles for ANDi and amplifier similariton pulses.

transform limit are obtained. The corresponding compressed parabolic pulses are essentially identical, whereas the ANDi pulses show additional secondary structure for fully dechirped inputs.
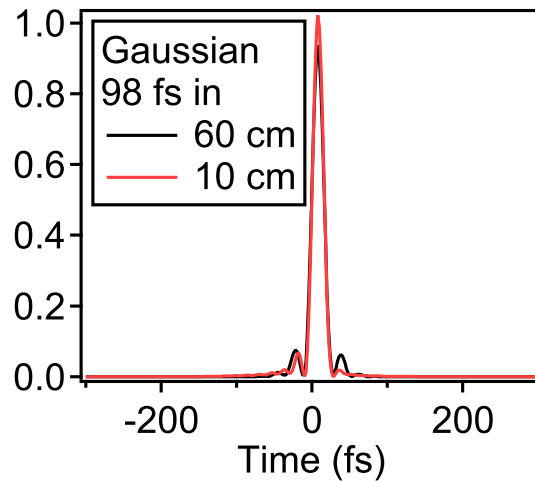

Figure 8.24: Compressed temporal profiles for gaussian pulses.

We have numerically studied the SPM pulse compression down to 15 fs durations of ANDi laser and amplifier similariton pulses . In the ANDi laser case, the side-peaks are amplified when using a nearly dechirped pulse, whereas the spectrum is more SPM-like at large chirp. For the amplifier similariton pulses,

parabolic pulse compression occurs at large chirp, and SPM compression takes over at small chirps.

For the ANDi pulse, it is preferable to use a stretching ratio of about 3x to minimize spectral structure and obtain cleaner compressed pulses. For the amplifier similariton pulses, dechirped input pulses produce the best compression, with performance similar to gaussian inputs. The optimal compression at low chirps is due to the typical pedestals formed by SPM on chirped pulses.

Although the spectra generated by chirped inputs are smoother, better pulse compression is obtained from the more complex spectra generated at low chirps. The parabolic spectra of the amplifier similariton pulse develops less pronounced structure and is thus better suited for short pulse compression.

Bibliography

[1] J. E. Sharping, J. Lightwave Technol. **26**, 2184 (2008).

[2] Y.-H. Zhai, C. Goulart, J. E. Sharping, H. Wei, S. Chen, W. Tong, M. N. Slipchenko, D. Zhang, and J.-X. Cheng, Appl. Phys. Lett. **98**, 191106 (2011).

[3] C. Gu, C. Goulart, and J. E. Sharping, Opt. Lett. **36**, 1488 (2011).

[4] V. P. Yanovsky and F. W. Wise, Opt. Lett. **19**, 1547 (1994).

[5] Y. Deng, Q. Lin, F. Lu, G. P. Agrawal, and W. H. Knox, Opt. Lett. **30**, 1234 (2005).

[6] J. E. Sharping, M. A. Foster, A. L. Gaeta, J. Lasri, O. Lyngnes, and K. Vogel, Opt. Express **15**, 1474 (2007).

[7] Y. Deng, C.-Y. Chien, B. G. Fidric, and J. D. Kafka, Opt. Lett. **34**, 3469 (2009).

[8] M. D. Perry, T. Ditmire, and B. C. Stuart, Opt. Lett. **19**, 2149 (1994).

[9] L. E. Hooper, P. J. Mosley, A. C. Muir, W. J. Wadsworth, and J. C. Knight, Opt. Express **19**, 4902 (2011).

[10] T. Ganz, V. Pervak, A. Apolonski, and P. Baum, Opt. Lett. **36**, 1107 (2011).

APPENDIX A

NUMERICAL METHODS

A.1   The Runge-Kutta interaction picture method

Numerically simulating phenomena involving large non-linear phase accumulation is susceptible to discretization errors. The usual method for non-linear optical pulse propagation is the split step-Fourier method ([1], section 2.1.4). It involves separating the linear part $\widehat{D}$ and the non-linear part $\widehat{N}$ and computing them separately over a longitudinal step h. The linear operator is evaluated in the Fourier domain, and the non-linear part is usually handled with a 4th order Runge-Kutta integrator.

$$\frac{\partial A}{\partial z} = (\widehat{D} + \widehat{N})A \tag{A.1}$$

$$A_{n+1} = e^{h(\widehat{D}+\widehat{N})}A_n \approx e^{h\widehat{D}}e^{h\widehat{N}}A_n \tag{A.2}$$

The accuracy of the split-step method is limited to first order in h by the operator commutator $[h\widehat{D}, h\widehat{N}] \sim h^2$. It is possible to split each propagation step further to achieve better accuracy. The most commonly used scheme is the symmetric split-step Fourier method. The dispersion operator is split into two half-steps, and the non-linear part is evaluated in the middle of the segment.

$$A_{n+1} = e^{\frac{h}{2}\widehat{D}}e^{h\widehat{N}}e^{\frac{h}{2}\widehat{D}}A_n \tag{A.3}$$

Combined with a 4th order Runge-Kutta integrator, this yields an accuracy $\sim h^2$.

$$A_D = e^{\frac{h}{2}\widehat{D}} A_n \tag{A.4}$$

$$k_1 = h\widehat{N} A_D$$

$$k_2 = h\widehat{N}(A_D + k_1/2)$$

$$k_3 = h\widehat{N}(A_D + k_2/2)$$

$$k_4 = h\widehat{N}(A_D + k_3)$$

$$A_{RK} = A_D + k_1/6 + k_2/3 + k_3/3 + k_4/6$$

$$A_{n+1} = e^{\frac{h}{2}\widehat{D}} A_{RK}$$

More elaborate arrangements of $\widehat{D}$ and $\widehat{N}$ can cancel higher-order errors. The Runge-Kutta in the Interaction Picture (RK4IP) method includes the linear operator into the Runge-Kutta integrator [2]. This yields an algorithm with an accuracy $\sim h^4$, the limit of the RK integrator.

$$A_D = e^{\frac{h}{2}\widehat{D}} A_n \tag{A.5}$$

$$k_1 = e^{\frac{h}{2}\widehat{D}} [h\widehat{N} A_n]$$

$$k_2 = h\widehat{N}(A_D + k_1/2)$$

$$k_3 = h\widehat{N}(A_D + k_2/2)$$

$$k_4 = h\widehat{N}(e^{\frac{h}{2}\widehat{D}} [A_D + k_3])$$

$$A_{n+1} = e^{\frac{h}{2}\widehat{D}} \left[A_D + k_1/6 + k_2/3 + k_3/3\right] + k_4/6$$

To test the RK4IP method, we reproduced a picosecond Raman generation simulation from [1], section 8.3.3. Convergence was tested for both the symmetric split-step and RK4IP method by comparing results to a 200 000 longitudinal step simulation and computing the relative error as in [2]. For less than 2000 steps, the accuracy scales like h^4 for both methods, indicating the coefficient of the h^5 error

is the same. For more than 2000 steps, the h^3 error of the split-step method limits its accuracy to h^2. As expected, the RK4IP method remains accurate up to h^4, until a accuracy floor is reached, probably due to the double precision limit of the machine. The numerical noise growth in Raman generation discussed earlier was found to appear for a larger step number than with the split-step method.
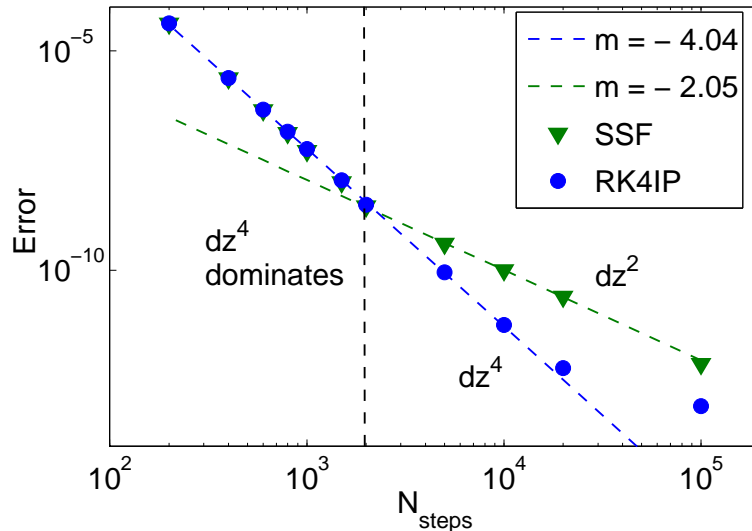

Figure A.1: Numerical accuracy of symmetric split-step Fourier and RK4IP algorithms.

A.2 Discrete noise distributions

This section describes how to numerically model random field such as spontaneous Raman scattering and shot noise.

The Raman ASE $\Gamma_R(t, z)$ is modeled by the correlation spectrum of Eq. 1.13:

$$\langle \Gamma_R(\Omega, z)\Gamma_R^*(\Omega', z') \rangle = \frac{2f_R \hbar \omega_0}{\gamma} |\mathrm{Im}[h_r(\Omega)]| \left[n_{th}(|\Omega|) + U(-\Omega) \right] \delta(\Omega - \Omega')\delta(z - z').$$
$$(A.6)$$

The delta functions indicate the field is uncorrelated between different frequency bins or propagation steps, but the average magnitude follows a thermalized Raman gain spectrum. Numerically, we generate it by creating a random complex gaussian number distribution u_i^{rand} with zero mean and unit variance, then multiplying by the thermalized Raman spectrum of Eq. A.6 [3]. The delta-functions are discretized according to $\delta(x_i - x_j) = \delta_{i,j}/\Delta x$, where $\delta_{i,h}$ is the Kronecker delta and Δx is the discretization step:

$$\Gamma_R(\Omega_i, z_i) = \sqrt{\frac{2f_R\hbar\omega_0}{\gamma}|\mathrm{Im}[h_r(\Omega_i)]|\left[n_{th}(|\Omega_i|) + U(-\Omega_i)\right]}\frac{u_i^{rand}}{\sqrt{\Delta\Omega\Delta z}}. \tag{A.7}$$

Similarly, the shot noise correlation spectrum is given in Eq. 1.14 [4]:

$$\langle\delta A^*(f)\delta A(f')\rangle = \frac{hf}{2}\delta(f - f'). \tag{A.8}$$

The delta function can be discretized as above. Thus, shot noise can be modeled by adding a complex gaussian random distribution $\delta A(f_i)$ to the input pulse in the frequency domain:

$$\delta A(f_i) = \sqrt{\frac{hf_i}{2\Delta f}}u_i^{rand}. \tag{A.9}$$

Bibliography

[1] G. P. Agrawal, *Nonlinear Fiber Optics*, 3rd ed. (Academic Press, New York, 2001).

[2] J. Hult, J. Lightwave Technol. **25**, 3770 (2007).

[3] S. J. Carter, Phys. Rev. A **51**, 3274 (1995).

[4] R. Paschotta, Appl. Phys. B-Lasers O. **79**, 153 (2004).